Quantitative analyses of single mitochondrial components reveal an early role of small-mitochondrial-networks in priming neoplasticity

Mayank Saini[1#], Swati Agarwala[1#], Biratal Wagle[1], Brian Spurlock[2,3], Bharti Golchha[1], Danitra Parker[2,4] and Kasturi Mitra[1,2*]

[1] Department of Biology, Ashoka University, New Delhi (NCR), India

[2] Department of Genetics, University of Alabama at Birmingham, Birmingham, Alabama, USA

[3] McAllister Heart Institute, Department of Pathology, University of North Carolina, Chapel Hill, USA

[4] Dept of Integrative Biology and Pharmacology, Institute of Aging, University of Texas Health Science Center at Houston, USA

* corresponding author: Kasturi Mitra

[#] Equal Contribution

Email: kasturi.mitra@ashoka.edu.in (primary)

Author Contributions: M.S. performed all mito-SinComp analyses, S.A. performed all transcriptomics analyses, B.W. developed mito-SinComp analyses with help from M.S., B.S. and D.P. collected data, B.G. performed immunoblot analyses, K.M. supervised all aspects and wrote the manuscript with help from M.S., S.A. and B.W.

Competing Interest Statement: None

Classification: Biological sciences, Cell Biology

Keywords: Mitochondrial network heterogeneity, Stemness driven neoplasticity, Microscopy, scRNA-seq, Carcinogen

This PDF file includes:

Main Text
Figures 1 – 7 and their legends

Abstract

Quantitative understanding of mitochondrial heterogeneity is necessary for elucidating the precise role of these multifaceted organelles in tumor cell development. We demonstrate an early mechanistic role of mitochondria in initiating neoplasticity by performing quantitative analyses of structure-function of single mitochondrial components coupled with single cell transcriptomics. We demonstrate that the large Hyperfused-Mitochondrial-Networks (HMNs) of keratinocytes promptly get converted to the heterogenous Small-Mitochondrial-Networks (SMNs) as the stem cell enriching dose of the model carcinogen, TCDD, depolarizes mitochondria. This happens by physical reorganization of the HMN nodes and edges, which enriches redox tuned SMNs with distinct network complexity. This leads to establishment of transcriptomic interaction between the upregulated redox relevant mtDNA genes and the lineage specific stemness gene, KRT15, prior to cell cycle exit. The SMN enrichment and related transcriptomic connections are sustained in the neoplastic cell population. Consistently, carcinogenic dose incapable of causing pronounced neoplastic stem cell enrichment fails to establish specific enrichment of SMNs and its linked mtDNA-KRT15(stemness) transcriptomic interaction prior to cell cycle exit. The mtDNA-KRT15 modulation is confirmed in cSCC tumors, while highlighting patient heterogeneity. Therefore, we propose that early enrichment of redox-tuned SMNs primes neoplastic transformation by establishing mtDNA-stemness transcriptomic interaction prior to cell cycle exit towards specifying quiescent neoplastic stem cells. Our data implies that redox-tuned SMNs, created by mitochondrial fission, would be sustained by tuning the balance of mitochondrial fission-fusion during neoplastic transformation. The proposed early role of mitochondria in cancer etiology is potentially relevant for designing precision strategies for cancer prevention and therapy.

Significance Statement

The challenges of understanding the complex role of the multifaceted and heterogenous cellular organelles, mitochondria, can be potentially overcome with their quantitative analyses. We use a combinatorial approach of quantitative analyses of single-mitochondrial-components and scRNA-seq to elucidate a mechanism of mitochondrial priming of cancer initiation by a model carcinogen. We propose that conversion of large Hyperfused-Mitochondrial-Networks (HMNs) to Small-Mitochondrial-Networks (SMNs) primes non-transformed keratinocytes towards their neoplastic transformation. Mechanistically, the SMNs, enriched by modulation of the physical nodes and edges of mitochondrial networks, tunes mitochondrial redox balance to establish transcriptomic interactions towards specifying a state of stemness. Further probing of our fundamental findings in the light of cancer heterogeneity may facilitate refinement of the various proposed mitochondria based targeted cancer therapies.

Main Text

Introduction

Regulation of cellular homeostatic processes requires nuanced spatiotemporal control, which when disturbed may lead to pathological conditions. The mitochondria, as dynamic organelles, act as gatekeepers of multiple cellular homeostatic processes and, also form signalling hubs (1, 2). Mitochondria are heterogeneous between tissues, cell types and even within cells, while their dysfunctionality has been causatively linked to various disease pathology (3–5). The involvement of mitochondria in cancer pathology has been studied at various functional levels, including regulation of energy metabolism, signalling and gene expression (6, 7). Initiation of tumor formation can happen when the lineage specific adult stem cells undergo neoplastic transformation into tumor initiating cells (8, 9). Importantly, certain tumor initiating cells are particularly vulnerable to mitochondrial inhibition (10, 11). However, mitochondrial heterogeneity, at the level of tumor cells as well as cancer patients, poses challenges in developing a generalized understanding of the exact role of mitochondria in cancer initiation or progression, thus making translation of findings difficult.

Mitochondria are heterogenous in their shapes and structures, including their elaborate physical networks, modulation of which affects cell proliferation and various other cellular processes critically (12–16). Mitochondrial structure-function is primarily modulated by the counteracting processes of mitochondrial fission and fusion. The core molecular machinery for mitochondrial fission involves Drp1 and its mitochondrial recruiters MFF or FIS1, while that of mitochondrial fusion are the Mitofusins and OPA1 (15, 17). Fission and fusion of mitochondria can act in concert in regulating the same or different aspect of a given cellular process (18–22). However, how mitochondrial fission and fusion processes coordinate to maintain the physical mitochondrial networks remains an open question, largely due to lack of quantitative understanding of the mitochondrial networks per se. Additionally, mitochondria can exist anywhere in the shape spectrum in normal or pathophysiological states, which is not reflected accurately by genetic alteration of the molecular players. Therefore, straightforward genetic approaches have led to confusing findings preventing building a consensus of the exact role of mitochondrial fission and fusion in cancer development. This highlights the necessity of developing quantitative understanding of the structure-function of mitochondria across their shape spectrum to elucidate the intricate interplay of mitochondria with other cellular process.

Various laboratories, including our own, have attempted to define and quantitate mitochondrial shape using high resolution confocal microscopy (23–30). Using quantitative approach of mitochondrial structure and function analyses, we have previously reported that a distinct structure and function state of mitochondria prime neoplastic stemness in ovarian and keratinocyte lineages (20, 30). In this priming process, low mitochondrial fission and high mitochondrial membrane potential are achieved to poise the cells for self-renewal and proliferation. Similar mitochondria-driven priming of stem cells has also been reported in neural, hematopoietic and mammary lineages (31–33). Using a model carcinogen that influences stemness properties in multiple cell lineages (34–39), we reported that repression of mitochondrial fission as well as its regulated activation are required to prime a stem cell state to

initiate as well as sustain neoplasticity in keratinocytes (20). Activation of mitochondrial fission is also essential for oncogene induced neoplastic transformation in other lineages (40, 41).

Here, we investigate the mechanism of mitochondrial priming of stemness towards initiating neoplastic transformation. We find that particularly low dose the model carcinogen, TCDD, which enriches neoplastic stem cells (20), can itself initiate mitochondria-based priming of stemness in non-transformed cells within one hour of exposure. To probe into the role of intracellular mitochondrial heterogeneity, we developed quantitative structure-function analysis of **sin**gle **mito**chondrial **comp**onents (mito-SinComp) and employed it along with quantitative single cell RNA Seq (scRNA-seq). We and others previously described the role of hyperfusion of mitochondria in cell cycle transition, stress, starvation and inhibition of stemness driven neoplasticity (20) (22, 42, 43). Here we demonstrate that TCDD driven priming of neoplasticity involves precise conversion of the **H**yperfused-**M**itochondrial-**N**etworks **(HMNs)** to **S**mall-**M**itochondrial-**N**etworks **(SMNs)**. Based on mito-SinComp and transcriptomic network analyses (hdWGCNA), we propose that early enrichment of redox tuned SMNs primes neoplastic transformation by establishing mtDNA-stemness interaction prior to cell cycle exit towards specifying quiescent neoplastic stem cells. Data obtained with our novel and combinatorial approaches reveal a mechanistic underpinning of cancer initiation involving early mitochondrial priming of stemness, while highlighting heterogeneity of such a process in patient tumors. Further probing of our fundamental findings in in vivo cancer models and in patient tumors may facilitate informed design of personalized strategies for cancer prevention and therapy.

Results

Single mitochondrial analyses identify and characterize the physical Small- Mitochondrial-Networks that are linked to stemness transcriptomic network

We previously employed single cell modalities of mito-SinCe (for mitochondrial shape analyses) and scRNA-seq (for transcriptomics analyses) to elucidate mitochondrial priming of stem cell driven neoplasticity in HaCaT keratinocytes (20, 44). Such mitochondrial priming of self-renewal and proliferation is characterized by enrichment of cells with intermediately-fused mitochondria, while hyperfusion of mitochondria prevents such stem cell priming. Here we designed analyses of single mitochondrial components, '**mito-SinComp'**, to quantitively define, identify and characterize the physical mitochondrial networks, and identify any linked stemness transcriptomic network by employing scRNA-seq analyses. We took advantage of our previously published mito-SinCe data set where 'intermediately-fused' (**INT**) or 'hyperfused' (**HF**) mitochondria are enriched, respectively, in cells with weak or strong knockdown of the mitochondrial fission protein Drp1 (20). Here, we combined this data set and studied individual mitochondrial networks and non-networks from the INT and HF cell groups as defined by the [Fission] vs [Fusion5] bivariate plots (**Fig. 1A**); these mito-SinCe metrics were designed from MitoGraph output (30, 45). The total mitochondrial length per cell in the INT group is lower than that of the HF group where, by definition, cells tend to have fewer mitochondrial components due to fusion of majority of components (**Fig. S1A-B**).

Using the newly developed mito-SinComp pipeline on the MitoGraph output we identified individual networks and non-networks of mitochondria (see Main and Supplementary Methods for

details), as represented by Cell1-INT and Cell2-HF having comparable total mitochondrial length **(Fig. 1B, Fig. S1C, Suppl. Data 1** showing comparison of the metrics for each cell**)**. The mito-SinComp pipeline revealed various structural properties of mitochondrial components in the INT-Cells and HF-Cells groups: **a)** comparable abundance of networked and non-networked mitochondria per cell (**Fig. S1D-E**) and length of non-networked mitochondria between the groups (**Fig. S1F,** right); **b)** higher abundance of longer networked mitochondria (i.e. hyperfused) in the HF-Cells group (**Fig. S1F,** left); **c)** the average length of the networked mitochondria per cell is substantially shorter in the INT-Cells group in comparison to the HF-Cells group, while the networked mitochondria are ~10-100 times longer than the non-networked mitochondria (**Fig. 1C, Fig. S1G**). These data raised the possibility that the INT-cells may be enriched with Small Mitochondrial Networks (**SMNs**) in contrast to the longer Hyperfused Mitochondrial Networks (**HMNs**) of the HF-cells. To confirm this, we computed the 'Cell-Relative Length of mitochondrial network or non-network', [CRL mito-Net] or [CRL mito-nonNet]. This metric for a networked or non-worked mitochondria is the natural log transformed value of its length normalized by the total length of network or non-network of the cell it belongs to (**Suppl. Methods**). The networks with maximum [CRL mito-Net] for the mitochondrial populations of Cell 1- INT and Cell 2-HF are boxed and extracted in **Fig. 1B** and their network metrics are listed in **Suppl. Data 1**. Interestingly, frequency distribution of [CRL mito-Net] indicates more networks with higher value of this metric are found in the INT-cells than the HF-cells, while it is reverse for the [CRL mito-nonNet] (**Fig. 1D**). This data signifies that SMN enriched cells harbor multiple networks of comparable length as opposed to fewer HMNs in any cell. Therefore, we aimed to distinctly classify the SMNs and the HMNs using a threshold range of [CRL mito-Net] (**Fig. 1D**) (see appropriate Methods section for more details of the threshold). Classification using [CRL mito-Net] confirmed that the number of SMNs is ~5 fold higher than the HMNs in the total population of INT-cells and HF-cells **(Fig. S1H)**, as exemplified by Cell 1-INT and Cell 2-HF in **Fig. 1B**. Most importantly, [CRL mito-Net] based classification demonstrated marked enrichment of the identified SMNs in the INT-cells while confirming the expected enrichment of the identified HMNs in the HF-cells (**Fig. 1E**).

Thereafter, we quantified the physical network properties between the SMN and the HMNs using various metrics (see **Suppl. Methods** for definition and formulae) and compared the median and the coefficient of variation (indicating heterogeneity) (**Fig. 1F, Fig. S1I**). In comparison to the HMNs, the SMNs exhibit the following properties: **a)** ~2 fold smaller in size (assessed by total length) and are remarkably heterogenous in thickness (assessed by diameter); **b)** ~10 fold fewer mitochondrial nodes and edges (edges represent individual mitochondrial elements within a network and the nodes represent their intersection points; terminal free nodes are not counted). **c)** by and large comparable element size (assessed by element length) within a network; **d)** comparable network complexity (assessed by nodes or edge density), with remarkable heterogeneity; **e)** comparable overall and maximum connectivity. These metrics demonstrate that as compared to the HMNs, the SMNs are remarkably heterogenous in their thickness and network complexity, while their organization of the nodes and edges are distinct with comparable length of individual mitochondrial element within the networks.

Next, we asked if SMN enrichment can be linked to the transcriptomic network of the functional stem cell gene, KRT15, of the keratinocyte lineage (46). Therefore, we employed the recently reported hdWGCNA pipeline (see Methods) on our published scRNA-seq data. There, the KRT15^{hi} stem cells are enriched by the weak (W) Drp1 knockdown and depleted by the strong (S) Drp1 knockdown (kd) (20). First, we performed pairwise pseudo-bulk RNA-seq analyses to

198 identify the genes that are differentially expressed in the Drp1-kd (W) and Drp1-kd (S)
199 populations with respect to the NT control populations. hdWGCNA of the combined gene sets of
200 the above pairwise analyses identified the KRT15 transcriptomic interaction module with 10
201 genes directly interacting with KRT15 **(Fig. 1G, left, Fig. S2A).** Next, we performed cell cluster
202 analyses of the pooled data sets of the NT, Drp1-kd (W) data and Drp1-kd (S) populations.
203 Notably, 4 out of the above 10 directly interacting partners of KRT15 were confirmed in one of the
204 modules identified by hdWGCNA performed with the marker genes of the quiescent / slow-cycling
205 KRT15^{hi} stem cell cluster (SloCycl-K15^{hi} as in ref. (20)) **(Fig. 1G, right, Fig. 1H, Fig. S2B-C,**
206 **boxed)**. Most importantly, the KRT15 interacting genes undergo marked upregulation across all
207 cell clusters in the Drp1-kd (W) population that sustains enrichment of the stem cell linked INT
208 subpopulation harboring abundant SMNs **(Fig. 1I, Fig. S2D)**. On the other hand, two of those
209 genes (CRABP2, KRT4) undergo marked downregulation only in the SloCycl-K15^{hi} cells Drp1-kd
210 (S) population with abundant HF-cells with depleted SMNs.

211 In summary, we employed mito-SinComp structural analyses on the combined population
212 of Drp1 knockdown and control to design a metric, [CRL mito-Net], for distinguishing the SMNs
213 from the HMNs within individual cells (**Fig. 1J**). The SMNs are abundant in the INT-cells that are
214 prevalent in the stem cell enriched Drp1-kd (W) population (20). Whereas the SMNs are fewer in
215 the HF-cells that are prevalent in the stem cell depleted Drp1-kd (S) population (20). In
216 comparison to the HMNs, the SMNs are remarkably heterogenous, have distinct network
217 organization, and are linked to stemness transcriptomic network characterized by KRT15-
218 interacting genes identified by hdWGCNA analyses. Application of [CRL mito-Net] successfully
219 detected enrichment of SMNs in sorted neoplastic stem cells in yet another cell lineage (not
220 shown).

221

222 **Acute-1h exposure to stem cell enriching carcinogen depolarizes mitochondria and**
223 **converts HMNs to complex and heterogenous SMNs, by modulating their nodes and edges**

224 HaCaT keratinocytes that maintain 'intermediately-fused' or 'hyperfused' mitochondria
225 **(**similar to **Fig.1A)** are primed or blocked, respectively, for stem cell driven neoplastic
226 transformation driven by the model carcinogen TCDD (20). Here we find, acute 1 hour exposure
227 of HaCaTs to TCDD-1nM (T1) promptly depolarizes mitochondria with respect to Toluene (Tol)
228 vehicle control **(Fig. 2A** top**, Fig. S3A, Fig. S3B** top**)**. However, the higher dose, TCDD-10nM
229 (T10), needs 4 hours to cause the marked mitochondrial depolarization **(Fig. 2A, Fig. S3B**
230 bottom**)**. We hypothesized that the dose independent early mitochondrial depolarization by T1-1h
231 exposure causes mitochondrial priming for stemness to promote stem cell driven neoplasticity
232 observed particularly with prolonged T1 exposure (20). Given mitochondrial depolarization
233 causes alteration of mitochondrial shape in various systems tested (15, 47), we studied the
234 quantitative properties of mitochondrial structure after exposure to Tol-1h (vehicle control), T1-1h
235 (stem cell enriching dose) and T10-1h (control dose) **(Fig. 2B)**. We used live cells stably
236 expressing the mitochondrial structural probe mito-PSmO2 for determining structural features of
237 single mitochondrial components within single cells **(Fig. S3C)**. The 3D maps of networked and
238 non-networked mitochondria in the representative cells from experimental groups indicate lack of
239 large mitochondrial networks after T1-1h exposure, whereas the T10-1h exposed mitochondrial
240 networks appear to be similar to that of Tol-1h (**Fig. 2C)**. Consistently, the mito-SinCe metric
241 [Fission] suggests that T1-1h exposure elevates the contribution of mitochondrial fission in

maintaining mitochondrial shape, which is modest with T10-1h exposure **(Fig. 2D)**. However, the mito-SinCe metric [Fusion5] reveals that the reduced contribution of mitochondrial fusion is comparable between the T1-1h and T10-1h exposure.

To probe further, we performed mito-SinComp structural analyses, as described in **Fig. 1**, towards quantitative elucidation of the features of the mitochondrial networks and non-networks after TCDD exposure**.** Consistent with **Fig. 2D**, particularly T1-1h exposure reduces the average length of both networked and non-networked mitochondria within individual cells, while T10-1h exposure modestly reduces the network length only **(Fig. 2E, Fig. S3D-G)**. Thus, the data clearly demonstrates that T1-1h dose reduces the length of the overall mitochondrial population likely through modulation of fission, unlike T10-1h. Furthermore, the distribution of the [CRL mito-Net] metric demonstrates that in comparison to Tol-1h exposure, T1-1h exposure increases the cell-relative length of the mitochondrial networks, which happens to a lesser degree with T10-1h exposure **(Fig. 2F, left)**. The distribution of [CRL mito-nonNet] and individual mitochondrial length (networked and non-networked) remain largely comparable between the groups **(Fig. 2F, right, Fig. S3H)**. Importantly, [CRL mito-Net] based classification **(**as in **Fig. 1D)** reveals remarkable enrichment of SMNs and concomitant depletion of the HMNs specifically with T1-1h exposure, in comparison to the Tol-1hr exposure **(Fig. 2G).** T10-1h exposure exhibits lesser specificity of enrichment and depletion of SMNs and HMNs, respectively. This data strongly suggests that the HMNs are promptly converted to SMNs particularly with T1-1h exposure.

Analyses of various structural metrics reveal that the overall SMNs remain heterogenous in their thickness and their network complexity (nodes or edge density) even after T1-1h or T10-1h exposure **(Fig. 2H, Fig. S3I-J).** Whereas, T1-1h exposure dramatically reduces the network size and the number of nodes and edges of the HMNs, almost to the level of the SMNs (lower abundance of HMNs compromises the statistical significance assessment through multiple hypothesis testing). Notably, T1-1h exposure does not impact the size of the individual mitochondrial elements within the networks **(Fig. 2H).** These observations corroborate the T1-1h induced conversion of HMNs to SMNs (**Fig. 2G**), and further demonstrate that the conversion happens particularly by modulating the organization of the nodes and edges of the HMNs. Moreover, T1-1h exposure also reduces the network size of the SMNs and substantially elevates their level and heterogeneity of the network complexity, while T10-1h has modest or no impact **(Fig. 2H)**. In contrast, the dose dependent effect of T1-1h and T10-1h exposure is seen in their modest reduction of SMN thickness **(Fig. 2H)**.

Taken together, our mito-SinComp structural analyses demonstrate that the stem cell enriching TCDD dose (T1-1h) promptly converts the HMNs to SMNs of greater network complexity and heterogeneity, thus enriching these SMNs. Our data suggest that T1-1h, which elevates the [Fission] metric, alters network organization of the HMNs by modulating their nodes and edges to convert them to more complex SMNs. This could be brought about by regulated fission events at the mitochondrial nodes. Noteworthily, the SMNs do not further disassemble into smaller elements suggesting a possible role of counteracting mitochondrial fusion events in maintaining the SMNs. Our data also highlights involvement of robust mitochondrial depolarization in the SMN enrichment process, although the cause-and-effect relationship remains to be elucidated.

285 **Acute-1h exposure to stem cell enriching carcinogen sustains an intermediate level of**
286 **oxidative status in the SMNs of restricted network complexity**

287 Precise redox regulation is crucial for stem cell maintenance as well as for neoplastic
288 transformation (48, 49). Long term TCDD exposure causes oxidative stress which has been
289 linked to its carcinogenicity (50–52). Here, we probed into the involvement of TCDD induced
290 mitochondrial redox changes that could arise due to mitochondrial depolarization **(Fig. 2A)**.
291 Therefore, we studied the impact of Tol-1h (vehicle control), T1-1h (stem cell enriching dose), and
292 T10-1h (control dose) on the relationship between mitochondrial redox status and their network
293 properties using mito-SinComp structure-function analyses **(Fig. 2B).** Here, the redox function is
294 measured in the mitochondrial networks and non-networks identified in **Fig. 2**. We used our
295 previously validated combination of genetically encoded general redox probe for mitochondrial
296 matrix, mito-roGFP, and mitochondrial structural probe mito-PSmO2 (30) **(Fig. 3A)**. Mito-
297 SinComp redox analyses generates [Oxidation] values for individual mitochondrial network and
298 non-network, which can be averaged to obtain the $[\text{Oxidation}]_{Av}$ values of an individual cell (see
299 Main and Supplementary Methods for details). We validated the automated mito-SinComp
300 intensity measurements by their strong linear correlation with those obtained manually using
301 standard image analyses software of select single mitochondrial components **(Fig. S4A-B)**;
302 weaker linear correlation of averaged values of all single mitochondria within single cells indicates
303 heterogeneity of intracellular mitochondrial signal. Nonetheless, the $[\text{Oxidation}]_{Av}$ values per cell
304 for populations exposed to Tol, T1 and T10 for 1 and 4 hours obtained by automated mito-
305 SinComp overall match with that obtained manually from standard image analyses software **(Fig.**
306 **S4C)**.

307 Consistent with dramatic mitochondrial depolarization with 4 hours exposure to TCDD
308 **(Fig. 2A)**, we noted an overall decrease in mitochondrial $[\text{Oxidation}]_{Av}$ per cell with such exposure
309 **(Fig. S4C)**. However, the unique T1-1h induced depolarization **(Fig. 2A)** associates with a trend
310 in increase in the median [Oxidation] within individual cells **(Fig. S4C)**, networks and non-
311 networks **(Fig. 3B-C)**. HMNs exhibit a striking increase in [Oxidation] with T1-1h exposure (**Fig.**
312 **3C**), which is consistent with the pronounced impact of T1-1h on the structural features of the
313 HMNs towards converting them to SMNs (**Fig. 2**) (the data remains compromised in statistical
314 significance assessment due to lower number of HMNs). Furthermore, the apparent bimodal
315 distribution of [Oxidation] in the SMNs of the Tol-1h and the T1-1h groups reduces to a unimodal
316 distribution in the T10-1h group (**Fig. 3C**). To tease out the heterogeneity associated with the
317 bimodal distribution of oxidative status within the SMN population, we divided the distribution into
318 [Oxidation]-Hi / Int / Lo zones; zone demarcations were defined using the level of minimum
319 abundance between the two peaks of Tol-1h control **(Fig. 3C,** dashed orange line**)** and its
320 distance to the upper quartile level of the T10-1h control **(Fig. 3C,** solid orange lines**)**. The impact
321 of the T1-1h on reduction of SMN size and elevation of their network complexity ([Nodes or Edge
322 density]) (**Fig. 2**) is observed in all the 3 zones (**Fig. 3D**). However, the trend in pronounced
323 reduction of number of elements within individual networks is limited to the [Oxidation]-Int zone
324 (**Fig. S4D**). To probe further, we performed bivariate structure-function analyses between
325 [Oxidation] and individual structural parameters of the SMNs and quantified their abundance in
326 the defined [Oxidation] zones. We noted that the [Oxidation]-Int zone is overall enriched (~1.7 X)
327 with T1-1h induced SMNs and [Oxidation]-Lo zone is enriched (~2X) with T10-1h induced SMNs,
328 with respect to the Tol-1h group **(Fig. 3E,** % distribution on the right**)**. Interestingly, the bivariate
329 plot between [Node or Edge density] and [Oxidation] appears to be unique from other structural
330 parameters **(Fig. 3E, S4E)**. Particularly, the SMNs are primarily restricted within a lower level of

331 [Node or Edge density] only in the [Oxidation]-Int zone (**Fig. 3E**, vertical dashed line), with
332 maximal nodal connectivity also restricted in this redox zone **(Fig. S4D-E)**. In contrast, the other
333 structural parameters do not exhibit restricted distribution in the [Oxidation]-Int zone **(Fig. S4E)**.

334 Therefore, our mito-SinComp structure-function analyses is able to quantitively tease out
335 mitochondrial heterogeneity, while strongly demonstrating an association of mitochondrial redox
336 levels particularly with mitochondrial network complexity ([Nodes or Edge density]). Moreover, our
337 data demonstrates that acute exposure to particularly the stem cell enriching dose of TCDD (T1-
338 1h) increases the abundance of SMNs at an intermediate level of oxidative status. The redox
339 tuned SMNs in the intermediate redox level have restricted network complexity. In the
340 subsequent sections, we investigate if the early enrichment of the complex and redox tuned
341 SMNs underlie the mitochondrial priming of stemness driven neoplastic transformation.

342

343 **Acute-2.5h exposure to stem cell enriching carcinogen upregulates mtDNA genes while**
344 **connecting transcriptomes for mitochondrial energetics and cell cycle exit**

345 Maintenance of mitochondrial fission at a goldilocks level maintains stemness gene
346 expression profile established by TCDD-1nM driven transformation in the HaCaT keratinocyte cell
347 model (20). Here, we asked if the HMN to SMN conversion by T1-1h exposure, achieved with
348 mitochondrial depolarization and increase in mitochondrial fission **(Figs. 2-3),** can lead to altered
349 gene expression towards priming of neoplasticity. Therefore, we performed scRNA-seq of HaCaT
350 cells promptly following SMN enrichment i.e. after 2.5 hrs exposure to Tol (vehicle control), T1
351 (stem cell enriching dose) and T10 (control dose).

352 First, we performed pairwise pseudo-bulk analyses of the scRNA-seq data to study the
353 impact of TCDD on overall gene expression **(Fig. S5A)**. Interestingly, the TCDD induced
354 functional stemness gene, Aldh1A3 (38, 53) is comparably upregulated with T1-2.5h or T10-2.5h
355 exposure, while upregulation of canonical TCDD target gene, *CYP1B1* (54), is detected only with
356 T10-2.5h **(Fig. S5B)**. Furthermore, the nuclear genes encoding mitochondrial proteins from
357 MitoCarta database (55) were overall downregulated by both T1-2.5h and T10-2.5h with respect
358 to Tol-2.5h **(Fig. 4A)**. Although T10-2.5h downregulates a substantially greater number of genes
359 for mitochondrial proteins, T1-2.5h specifically downregulates PHB (maintains mitochondrial
360 shape and mtDNA, (56–58), ATP5F1E (regulates energetics, (59) and C1QBP (regulates
361 mitochondrial protein synthesis (60, 61) (**Fig. 4A**, empty triangles). On the contrary, genes
362 encoded by the mitochondrial DNA (mtDNA) heavy strand were upregulated particularly by T1-
363 2.5h exposure (represented by 5 mtDNA genes detected in the data set, **Fig. 4A**); the singular
364 gene encoded by the mtDNA light strand (*MT-ND6)* was downregulated by T10-2.5h. Estimation
365 of protein levels confirmed that TCDD impacts the mtDNA encoded proteins differently than the
366 nuclear DNA encoded mitochondrial proteins (exemplified by MT-CYB and NDUFB3, filled
367 triangles in **Fig. 4A**). Similar to the scRNA-seq findings, T1-2.5h or T10-2.5h exposure caused a
368 modest increase or a dramatic reduction in MT-CYB levels, respectively, with no impact of TCDD
369 on NDUFB3 **(Fig. 4B-C)**; the difference between the protein and mRNA levels could be due to
370 little turnover of NDUFB3 protein within 2.5 hours of exposure. Next, we performed GSEA based
371 functional annotation of all differentially expressed genes from the pairwise pseudo-bulk analyses
372 of the scRNA-seq data **(Fig.S5A, Suppl Data. 2).** We found that both T1-2.5h or T10-2.5h
373 exposure downregulate genes involved in mitochondrial energetics and cell cycle, confirming

374 TCDD driven cell cycle exit (34–39); the fewer upregulated mtDNA genes were not detected in
375 any functional category **(Fig. 4D, Suppl. Data 2)**. On the other hand, the T10-2.5h driven
376 upregulation cell signaling genes are not observed with T1-2.5h.

377 Next, to study the cell cycle exit related transcriptomic interaction of the mitochondrial
378 energetics genes and cell cycle genes we performed hdWGCNA with the gene set of pairwise T1
379 / T10 vs Tol analyses described above. Relevantly, we probed into the presence mitochondrial
380 energetics genes (MitoCarta) and cell cycle genes (REACTOME) among the top 20 hub genes of
381 the identified transcriptomic interaction modules identified by hdWGCNA. Among the modules
382 obtained with gene set from the (T1 vs Tol)-2.5h analysis, maximum number of MitoEnergetics
383 (10) genes exhibit transcriptomic interaction with CellCycle (10) genes during cell cycle exit **(Fig.
384 4E,** boxed**)**. On the other hand, with the gene set from the (T10 vs Tol)-2.5h analysis, the T1-2.5h
385 and T10-2.5h groups were comparable for the mitoEnergetics-CellCycle transcriptomic interaction
386 modules **(Fig.S5C)**. Moreover, the gene connectivity within the cell cycle exit related
387 [mitoEnergetics-CellCycle] modules are strikingly complex in the above two T1-2.5h groups in
388 comparison to that of the T10-2.5h group, as reflected by the markedly higher number of edges in
389 their hub-gene network plots **(Fig. 4F)**. Interestingly, within the T1-2.5h-mitoEneregetics-
390 CellCycle-A module, the glycolytic enzyme GAPDH, with maximum degree connectivity **(Fig.
391 S5D)**, connects the mitoEnergetics and CellCycle genes. Notably, we did not detect any of the
392 mtDNA genes in any mitoEnergetics-CellCycle modules although mtDNA genes are integral part
393 of mitochondrial energetics circuitry.

394 Taken together our data demonstrates that acute exposure to particularly the stem cell
395 enriching TCDD dose (T1-2.5h) upregulates mtDNA heavy strand genes while causing cell cycle
396 exit (reflected by downregulation of cell cycle genes). Our data indicates that mtDNA genes and
397 mitoEnergetics-CellCycle transcriptomic network, induced promptly with the establishment of the
398 redox tuned SMNs (**Fig. 2-3**), prime the initiation of neoplastic transformation driven by the stem
399 cell enriching carcinogen dose (20).

400

401 **Acute-2.5h exposure to stem cell enriching carcinogen establishes MT-ND1-
402 KRT15(stemness) transcriptomic interaction in non-transformed proliferating cells prior to
403 their cell cycle exit**

404 Keratin-15 (KRT15) is a well-known functional marker for epidermal stem cells,
405 particularly in the keratinocyte lineage (46). We previously reported that TCDD-1nM induced
406 enrichment of quiescent-neoplastic-KRT15^{hi}-stem-cells happens with concomitant decrease in
407 cells with lower expression of mt-DNA genes in keratinocytes (20). Here we investigated if the
408 acute upregulation of mtDNA genes particularly by T1-2.5h exposure **(Fig. 4A)** is linked to KRT15
409 expression.

410 First, we performed scRNA-seq analyses to detect any emergence of the KRT15^{hi} stem
411 cell cluster with exposure to Tol-2.5h (vehicle control), T1-2.5h (stem cell enriching dose) and
412 T10-2.5h (control dose). We identified the cell clusters on a UMAP plot, quantified their
413 abundance **(Fig.5A, Fig.S6A)**, and assigned cluster functionality by GSEA on their respective
414 gene markers **(Fig.S6B, Suppl. Data 3)**. Consistent with TCDD induced overall cell cycle exit
415 **(Fig. 4D),** we found reduced abundance of the CellCycle^{hi} i.e. 'Proliferating' cells and increase in
416 that of the CellCycle^{lo} i.e. 'CC-Exiting' cells with both T1-2.5h or T10-2.5h exposure (**Fig.5A,**

Fig.S6A). Noteworthily, of all 18 members of KRT family genes, the contribution of the stem cell gene KRT15 is prominently highest in defining the CC-Exiting cluster due to its upregulation in the cells of this cluster **(Fig. 5B**, **Fig. S6C)**. This data suggests that the commencement of stemness (defined by KRT15 expression) is linked to cell cycle exit happening within 2.5 hours of TCDD exposure. Therefore, we re-designated the CC-Exiting cluster as CC-Exiting-K15^{hi} **(Fig. 5A)**. Additionally, T1-2.5h and T10-2.5h exposure reduce the abundance of 'Cytokine' producing cells, and modestly increase the number of 'Differentiated(KRTs)' cells (designated based on downregulation of cell cycle genes along upregulation of multiple keratin family genes). Noteworthily, the T1-2.5h driven upregulation of mtDNA heavy strand genes (**Fig. 4A**) happens across all cell clusters with maximum in Proliferating cells and minimum in CC-Exiting-K15^{hi} cells **(Fig. 5C, Fig.S6D).** This data suggests a direct impact of T1-2.5h on mtDNA gene expression that is likely mediated through the mitochondrial structure-function alterations **(Fig. 2-3).** Notably, MT-ND1, MT-ND4 and MT-ND5, crucial components of the major site of mitochondrial ROS production namely Complex I (62), underwent the most prominent increase with T1-2.5h exposure that was not detected in T10-2.5h exposure (**Fig. 5C,** boxed). The components of Complex III and IV are upregulated with both T1-2.5h and T10-2.5h exposure, although more with the former.

Next, we aimed at identifying any mtDNA gene co-expression modules with KRT15 and/or other relevant genes within each cell cluster using hdWGCNA and further assigned functionality to the listed modules using GSEA **(Fig. S7A, Suppl Data 3).** Expectedly, the distinct mtDNA (see Methods for reassignment) and the CellCycle modules are identified in almost all cell clusters across the Tol-2.5h, T1-2.5h and T10-2.5h groups **(Fig. 5D, S7B-D)**. Importantly, the mtDNA genes are found to interact with the stem-cell gene KRT15 only in the Proliferating cells of the T1-2.5h group **(Fig. 5C,** boxed**)**. Notably, KRT15 is downregulated in the Proliferating cells that exhibits maximum upregulation of mtDNA genes (**Fig. 5B-C**). Furthermore, the mtDNA-KRT15(stemness) interaction module includes the gene HES1 **(Fig. 5C)**, which is regulated to maintain quiescence (20, 63, 64) and was dramatically upregulated in T1 induced quiescent-KRT15^{hi}-stem-cell enriched transformed population (20). Hub-gene network analyses of the mtDNA-KRT15(stemness) module reveals a distinct network of interacting mtDNA genes, out of which only redox related MT-ND1 is directly connected to KRT15 **(Fig. 5E-F)**. In turn, within the T1-2.5h-Proliferating-mtDNA-KRT15(stemness) module, KRT15 is directly connected to meaningful partners namely its paralog KRT19, SERPINB13 of keratinocyte lineage (65), quiescence regulator HES1 (20, 63, 64) and redox scavenger GPX2 (66) **(Fig. 5E-F)**.

In summary, we conclude that enrichment of the redox tuned SMNs, by the stem cell enriching TCDD exposure, is followed by establishment of the redox relevant mt-ND1(Complex I)-KRT15(stemness) transcriptomic interaction in the proliferating cells before they exit cell cycle. Our findings also indicate that cell cycle exit related upregulation of KRT15 is linked to downregulation of mtDNA genes, which commences establishment of the reciprocal relationship of the KRT15^{hi} and the mtDNA^{lo} clusters observed in the stem cell enriched T1 transformed population (20). These results suggest that such mtDNA-KRT15(stemness) transcriptomic interactions established after SMN enrichment and prior to TCCD induced cell cycle exit underlie the priming of stemness within the first 3 hours of exposure only to the low carcinogen dose.

461 **Transformation with stem cell enriching carcinogen sustains SMN enrichment and MT-**
462 **{ND1 / CYB}--KRT15(stemness) transcriptomic interaction particularly in late S phase.**

463 Carcinogens, including TCDD, lead to neoplastic transformation after prolonged exposure
464 (50–52). We investigated if the priming related SMN enrichment **(Fig. 2)** and the mtDNA-
465 KRT15(stemness) transcriptomic interaction established by the stem cell enriching TCDD dose
466 **(Fig. 5)** is sustained even after neoplastic transformation. Here, we performed mito-SinComp and
467 hdWGCNA analyses of our published mito-SinCe and scRNA-seq datasets, respectively, of
468 HaCaT cells transformed by 1nM or 10nM TCDD (TF1**,** stem cell enriched or TF10, control dose)
469 using the non-transformed Parental (P) controls as necessary (20).

470 Similar to the cells with T1-1h or T10-1h acute exposure **(Fig. 2F)**, SMN and HMN
471 abundance is distinctly different between the TF1 and TF10 cell populations, as demonstrated by
472 mito-SinComp structural analyses **(Fig. 6A, Fig. S8A)**. However, TF1 cell population exhibits
473 enrichment of both SMNs and HMNs in individual transformed cells **(Fig. 6A)**, in contrast to the
474 marked conversion of HMN to SMNs by acute T1-1h exposure **(Fig. 2F)**. This suggests that
475 HMNs re-occurred in the TF1 cells after the priming event during the transformation process.
476 Nonetheless, the SMNs maintain higher heterogeneity than the HMNs, most prominently in their
477 network complexity (Edge/Node Density) **(Fig. 6B)**. Also, TF1 SMNs maintain higher
478 heterogeneity and are modestly thinner in comparison to those of the TF10 SMNs **(Fig. 6B, S8B)**.
479 However, in contrast to the cells undergoing priming by T1-1h dose, the properties of HMNs in
480 TF1 group are distinct from the SMNs in that group and remain more comparable to those of
481 TF10 group **(Fig. 6B, S8B)**. Next, we quantified the relative abundance of SMNs over HMNs in
482 each cell **(Fig. 6C, Fig. S8C).** We found that 29% of TF1 and 15% of TF10 cells harbor greater
483 number of SMNs than HMNs (" %SMN / %HMN " >1.1) whereas 64% TF1 and 80% of TF10 cells
484 harbor greater number of HMNs than SMNs (" %SMN / %HMN " <0.9) **(Fig. 6D)**. These data
485 together suggest that neoplastic transformation with long term exposure to the stem cell enriching
486 T1 dose allows one third of the transformed cells (TF1) to maintain abundance of SMNs that
487 retain heterogeneity in their network properties. In contrast, such a phenotype is substantially
488 weaker in cells transformed with long term T10 exposure (TF10).

489 Next, we addressed if the SMN enrichment in the TF1 cells are linked to any mtDNA-
490 KRT15(stemness) transcriptomic interaction module. Pairwise pseudobulk-RNAseq analyses of
491 the TF1 and TF10 cells in comparison to the parental cells confirmed the key observation of the
492 T1-1h or T10-1h exposure (**Fig. 4A**). Particularly, the SMN enriched TF1 population exhibits
493 specific upregulation of mtDNA heavy strand genes encoding components of Complex I and
494 downregulation of the mtDNA regulator PHB, which is not observed in the TF10 population **(Fig.**
495 **6E)**. Notably, the MT-ND1 gene with direct transcriptomic connection to KRT15 gene **(Fig. 5E, F)**
496 is downregulated in TF10 along with other mtDNA genes **(Fig. 6E).** On the other hand, the
497 nuclear genes encoding mitochondrial proteins showed a similar trend between the TF1 vs P and
498 TF10 vs P comparative groups **(Fig. S8D).** Importantly, hdWGCNA performed with the gene sets
499 obtained from the TF1 vs P analyses identified the lineage specific stem cell genes KRT15 and
500 SOX4 exclusively in one of the modules of the SMN and stem cell enriched TF1 population **(Fig.**
501 **S8E, boxed)**; only two mitochondrial energetics genes, other than the mtDNA genes, were
502 detected in the identified modules**.** In contrast, corresponding hdWGCNA performed for the gene
503 set obtained from the TF10 vs P analyses did not show any such interactions although one
504 module with mtDNA genes was identified **(Fig. S8E, bottom).**

505 TCDD driven carcinogenesis of keratinocytes models cutaneous squamous cell
506 carcinoma (cSCC) (50–52). Therefore, we aimed at confirming the distinction of mtDNA genes
507 observed between TF1 and TF10 population in the available scRNA-seq data from SCC patient
508 samples (67). We performed pairwise pseudo-bulk RNA-seq analyses of average expression of
509 mtDNA and other relevant genes between cutaneous SCC tumor and adjacent tissue available
510 from patients. A total of 9 out of 10 patients exhibit decrease in mtDNA in the tumors in
511 comparison to the adjacent normal tissue **(Fig. 6F, top panel).** This confirms our observation with
512 TF10 cells that form xenografts with SCC features (20). These patients also showed a decrease
513 in keratin genes in the tumor suggesting reversal of differentiation in the tumor cells **(Fig. 6F,**
514 middle panel, boxed**).** In contrast, one patient exhibits already low levels of keratin genes in the
515 adjacent normal tissue that does not further change in the tumor, suggesting a different state of
516 the normal cells **(Fig. 6F,** boxed**)**. Interestingly, this singular patient also exhibits prominent
517 increase in mtDNA genes in the tumor **(Fig. 6F,** boxed**),** similar to the SMN and stem cell
518 enriched TF1 cells that forms xenografts of primitive nature with lower tumor incidence (20).
519 Notably, the behavior of the nuclear encoded gene for the mitochondrial protein NDUFB3 (used
520 as control in **Fig. 4B-C)** is similar across all the 10 patients (**Fig. 6F**).

521 Next, we aimed at identifying the transcriptomic interaction modules in individual cell
522 clusters identified by scRNA-seq analyses of our published Parental (P), SMN and stem cell
523 enriched TF1 and TF10 cell populations, where the S-Late cells transition to the quiescent-
524 neoplastic-KRT15^{hi}-stem-cells (20). Therefore, we performed hdWGCNA on each cell cluster of
525 the TF1 and TF10 transformed populations to conclude about transcriptomic interaction in
526 transformed cells. Interestingly, among all the cell cycle stages detected (**Fig. S8F**), only the S-
527 Late cells of the TF1 population exhibit the relevant mtDNA-KRT15(stemness) direct
528 transcriptomic interaction in one module **(Fig. 6G-I).** In the TF1 population, KRT15 directly
529 interacts with both Complex I and Complex III components, namely MT-ND1 and MT-CYB,
530 respectively. In contrast, no direct mtDNA-KRT15(stemness) connections are detected in the
531 identified less complex mtDNA-KRT15(stemness) transcriptomic modules of the Cytokine
532 expressing cells of the TF1 and TF10 populations **(Fig. 6H-I).** Importantly, only the late S phase
533 cells of the TF1 population harbour an mtDNA-KRT15-HES1 transcriptomic interaction **(Fig. 6I),**
534 which was detected with T1 exposure **(Fig. 5E).** Taken together, our data demonstrates that the
535 MT-{ND1 / CYB}--KRT15(stemness) transcriptomic interactions established in the late S phase
536 are linked to the cell cycle exit to maintain the quiescent-neoplastic-KRT15^{hi}-stem-cells in the TF1
537 population.

538 In summary, our results demonstrate that the early SMN enrichment, the associated
539 upregulation of mtDNA genes and the mtDNA-stemness transcriptomic interaction of the non-
540 transformed proliferating cells continue to sustain even after neoplastic transformation. The
541 mtDNA-stemness transcriptomic interaction is particularly detected in the late S phase cells and
542 is potentially linked to their cell cycle exit to maintain the quiescent neoplastic stem cells (20). In
543 the transformed population, MT-ND1(Complex-I)-KRT15(stemness) and MT-CYB(Complex-III)-
544 KRT15(stemness) transcriptomic interactions are detected, implicating both the complexes for
545 mitochondrial ROS production (62). Our patient sample analyses also provide key validation of
546 the data from our cell line model, while also highlighting patient heterogeneity in the potential
547 mitochondria driven priming status of individuals.

548

Discussion

Studies on mitochondrial heterogeneity have revealed a more complex role of mitochondria in cancer and other pathophysiological conditions (1, 5, 14, 68, 69). Quantitative understanding of mitochondrial heterogeneity is required to elucidate the precise involvement of mitochondria on cellular pathophysiology. Here we tease out the significance of the intracellular mitochondrial heterogeneity in cancer initiation by developing and employing a quantitative analytical method for studying structure-function of single mitochondrial components. This mito-SinComp analysis distinguishes the physical mitochondrial networks from non-networks, identifies the Small-Mitochondrial-Networks (SMNs) and the Hyperfused-Mitochondrial-Networks (HMNs), and characterizes their structure-function properties**.** We further link findings from mito-SinComp analyses to stemness transcriptomic network involving mtDNA, by employing hdWGCNA on scRNA-seq data. Based on our findings from cell populations with early exposure to the model carcinogen TCDD and their neoplastic counterparts, we propose that early enrichment of redox-tuned small networks of mitochondria primes neoplasticity by establishing mtDNA-stemness transcriptomic network even prior to cell cycle exit towards specifying quiescent neoplastic stem cells **(Fig. 7).**

First, we detect enrichment of heterogenous SMNs linked to the transcriptomic network of the functional stem cell gene KRT15 in a non-transformed keratinocyte population **(Fig. 1),** where stemness was modulated by genetic manipulation of mitochondrial fission (20). Next, we demonstrate that the HMNs of the non-transformed keratinocytes are promptly converted to characteristically heterogenous and complex SMNs when the cells are exposed to low dose of the model carcinogen TCDD (**Fig. 2**), which enriches KRT15^{hi} neoplastic stem cells during transformation (20). HMN to SMN conversion is associated with dramatic mitochondrial depolarization and is brought about by modulation of the nodes and edges of the HMNs. The resulting heterogenous SMNs have their redox levels particularly linked to their network complexity (i.e. density of nodes and edges) (**Fig. 2,3**). Such early SMN enrichment is promptly followed by upregulation of mtDNA genes and establishment of a MT-ND1-KRT15(stemness) transcriptomic interaction in the proliferating non-transformed cells prior to their cell cycle exit **(Fig. 4, 5).** The neoplastic stem cell enriched transformed population indeed sustains the SMN enrichment while the MT-{ND1 / CYB}-KRT15(stemness) transcriptomic interaction is detected particularly in the Late-S phase before cell cycle exit **(Fig. 6).** Importantly, the control TCDD dose that does not cause pronounced enrichment of KRT15^{hi} stem cells (20) fails to establish the pronounced early enrichment of SMNs and its linked MT-{ND1 / CYB}-KRT15(stemness) transcriptomic interaction **(Figs 2-6).** The key data of the model carcinogen induced modulation of mtDNA-KRT15(stemness) gene expression from the model keratinocyte lineage is recapitulated in cSCC patient tumors, with notable patient heterogeneity. **(Fig. 6F).** This data implies that modulation of mtDNA gene expression in cSCC patients could be an early event of mitochondria driven priming of their tumor development.

Network forming ability of mitochondria is governed by the mitochondrial fission and fusion proteins. The mito-SinComp analyses of single mitochondrial networks and non-networks suggested a mechanism of conversion of HMNs to SMNs. To form the SMNs, the stem cell enriching carcinogen primarily reorganizes the HMNs at the nodes and their connected edges, while largely retaining the length of the mitochondrial elements **(Fig. 1F, 2H).** Such a mechanism

594 would involve induction of mitochondrial fission particularly at the nodes of the HMNs.
595 Consistently, stem cell enriching carcinogen elevates the [Fission] metric **(Fig.2D),** which can be
596 potentially triggered by activation of Drp1 driven mitochondrial fission (not shown). Thus, active
597 levels of mitochondrial fission in the cells with weaker Drp1 knockdown are able to enrich the
598 SMNs **(Fig 1J).** Therefore, our data indicates that marked inhibition of neoplastic transformation
599 by obliteration of Drp1 activity (20, 40, 41) may be due to inhibition Drp1 driven fission at nodes
600 of the HMNs, thus preventing their conversion to the SMNs. It remains to be studied if the SMNs
601 differ from HMNs in reported mitochondrial network functionalities namely, mitochondrial quality
602 control, equilibration or maintenance of mtDNA and other mitochondrial contents, transmission of
603 signal or analytes within the cell and imparting evolutionary advantage (70–73).

604 Enrichment of SMNs implies that their breaking down into individual mitochondrial
605 elements is prevented, which can be brought about by repressed Drp1 activity in concert with
606 counteracting fusion proteins. This conception of mitochondrial fission and fusion cycles
607 reconciles various apparently contradictory findings where fission or fusion regulators have been
608 causatively linked to stem cell regulation (19–21, 32, 33, 74–76). We also speculate that the
609 mitochondrial fission and fusion cycles involved in SMN generation and maintenance could
610 modulate the reductive metabolism sustained by the P5CS enzyme in the regions of reduced
611 ATP synthase activity (14), which could be in the mitochondrial zones of reduced ATP synthesis
612 we found in ~10% of some cancer cells (30). Indeed, we found reduction of ATP5F1E gene
613 expression in association with SMN enrichment and mtDNA-KRT15(stemness) interaction **(Fig.**
614 **4A)**. Moreover, fine-tuned repression of Drp1 that primes stemness (20) also elevates expression
615 of P5CS in the mtDNA^{lo} cell cluster (not shown).

616 It is reasonable to speculate that reduction in ATP synthesis is induced by mitochondrial
617 priming related mitochondrial depolarization that is linked to the prompt HMNs to SMNs
618 conversion. Studies with higher temporal resolution would reveal if mitochondrial depolarization
619 precisely controls assembly of fission sites at the HMNs nodes (possibility A in **Fig. 7**), or
620 mitochondrial fission driven removal of network elements depolarizes the SMNs (possibility B in
621 **Fig. 7**). Nonetheless, such precise regulation of the mitochondrial fission and/or fusion events
622 may the involve PHB driven regulation of mitochondrial shape and mtDNA (77, 78), that is altered
623 particularly during mitochondrial priming and with neoplastic stem cell enrichment **((Fig. 4A,**
624 **Fig.6E).** MtDNA aberrations impact stemness (79, 80), while greater than two-fold elevation of
625 mtDNA copy number occurs during the differentiation of various stem cells (3 and references
626 therein). Our study raises the possibility of a specific mtDNA regulation during cell cycle exit
627 towards specification of quiescent stem cells, potentially brought about by Prohibitin.

628 Redox regulation is critical in cancer development (48), and mitochondria are a crucial
629 hub of redox signaling that is controlled by precise regulation of mitochondrial energetics circuitry
630 (2, 81). Spatiotemporal heterogeneity in mitochondrial redox regulation and its crosstalk with
631 mitochondrial structural properties are documented (82–84). Here, for the first time we identified
632 the property of 'network complexity' of the SMNs to be linked to their redox levels **(Fig.2G-H, 3D-**
633 **E)**, suggesting SMNs formation as a potential spatio-temporally controlled mechanism of fine-
634 tuning redox signaling. In the context of mitochondrial priming of stem cells, our study
635 demonstrates the following 3 aspects of redox regulation. First, the impact of the oxidative
636 carcinogen TCDD on mitochondrial redox levels varies based on the mitochondrial network status
637 (**Fig. 3B-C**). Second, importance of an intermediate zone of [Oxidation] with restricted network
638 complexity emerges in the concept of priming for stemness **(Figs. 3D,E).** Third, TCDD driven

639 mitochondrial priming involves interaction of the stemness gene KRT15 and mitochondrial
640 Complex I (**Fig. 5E**, **Fig. 6I**) or Complex III (**Fig. 6I**) that are the main sites of mitochondrial ROS
641 production (62). These observations raise the possibility that SMN driven tuning of redox
642 signalling may be important towards maintaining stemness gene expression profile, given
643 disturbing the tuned redox levels of stem cells disrupts their properties (85–87).

644 Redox regulation of S phase of cell proliferation cycle has been documented (88–92).
645 Cell cycle exit and acquisition of quiescence is critical to maintaining stem cell pool and
646 functionality (93). Upregulation of mtDNA genes during TCDD driven priming happens as
647 transcriptomic interactions are established between cell cycle and mitochondrial energetics genes
648 (**Fig. 4 D-F**). Moreover, the MT-ND1-KRT15(stemness) transcriptomic interaction is established
649 before non-transformed cells exit cell cycle during priming and particularly in Late-S phase in the
650 transformed population (**Fig. 5D-F, 6G-I**). We showed that the cellular decision of bifurcation of
651 the KRT15^{hi} and its reciprocal mtDNA^{lo} cell populations is likely made in the Late-S phase cells
652 (20). Therefore, our data generates the speculation that the MT-ND1-KRT15(stemness)
653 transcriptomic interaction is involved in redox regulated cell cycle exit for enrichment of the
654 quiescent-neoplastic-KRT15^{hi} stem-cells involving HES1 (**Fig. 5D, Fig. 6I**).

655 In conclusion, using combinatorial approach of quantitative microscopy and single cell
656 transcriptomics employed on experiments with a model carcinogen, we elucidate a biological
657 mechanism of cancer initiation involving stemness specification. We propose that conversion of
658 HMNs to SMNs, by modulating the complexity of mitochondrial networks, is a mechanism of
659 priming non-transformed cells for stem cell driven neoplasticity. Mechanistically, the enriched
660 SMNs would tune the mitochondrial redox balance to support transcriptomic interactions required
661 to specify a stem cell state to support neoplastic transformation. Further probing of our
662 fundamental findings in the light of cancer heterogeneity may allow refinement of various
663 proposed mitochondria based targeted cancer therapies (11).
664
665

666 Materials and Methods

667

668 **Cell culture, mitochondrial staining, confocal microscopy, immunoblotting** : Immortalized
669 skin keratinocyte cell line HaCaT, the previously derived TCDD transformed lines and the stable
670 lines expressing mito-PSmO2 and mito-roGFP were cultured following standard protocols (20,
671 44). Staining of TCDD exposed cells with TMRE or mitotracker green was performed while
672 maintaining TCDD in the staining solution, as described (20). Confocal microscopy for mito-SinCe
673 analyses was performed as described (30). The resulting confocal micrographs were utilized for
674 mito-SinComp analysis following appropriate quality control steps (30). Immunoblotting was
675 performed with TCDD exposed cells using standard methods using commercial antibodies to
676 NDUFB3, β-Actin (Santa Cruz Biotechnology), MT-CYB (Invitrogen), Tom20 (Cell Signaling
677 Technology), and compatible secondary antibodies.

678 **Development of mito-SinComp analysis for studying structure-function relationship of**
679 **single mitochondria :** Mito-SinComp analysis for single mitochondrial components is an
680 extension of our previously established single cell analytical approach mito-SinCe that uses the
681 primarily uses the open source MitoGraph algorithm for mitochondrial structural analyses (30). To
682 perform mito-SinComp analyses, we included function analyses for single mitochondrial
683 component identified by MitoGraph within single cells. In brief, the mito-SinComp analysis uses

684 3D confocal micrographs with appropriate combinations of compatible probes reporting
685 mitochondrial structure and function separately. Our customized, modular script for mito-SinComp
686 structure-function analysis comprises several steps (detailed in Supplementary Methods, **Fig.S9**).

687 The steps involve: **a)** identifying the 'structure' and 'function' channels; **b)** applying
688 MitoGraph for mitochondrial segmentation and identifying single mitochondrial components
689 (networks and non-networks); **c)** calculating their structural properties; **d)** calculating their redox
690 functional property by converting the MitoGraph output into pixel coordinates, calculating the
691 intensity values from the corresponding 'function' channels, converting them to average pixel
692 intensity ratio to obtain redox values for each element and then each component, and finally
693 validating the intensity values (**Fig.S4B**). The output of mito-SinComp analyses is a
694 comprehensive data file (*.csv) holding the relevant details for individual mitochondria in
695 individual cells; rows with point_ids under line_ids under cc_ids while columns with relevant
696 values for each id. This file is used to obtain the structural-function parameters and for creating
697 3D graphs for visualization. For intra-cellular comparisons of SMNs and HMNs, the *.vtk files
698 generated by MitoGraph for individual cells were analyzed and visualized using the open-source
699 software ParaView-v5.13.0 (https://www.paraview.org/). All plots were generated in Python using
700 appropriate modules.

701 To distinguish between SMNs and HMNs we employed a thresholding approach using
702 the [CRL mito-Net] metric, in conjunction with the previously defined cellular [Fusion1] metric (the
703 percent length of the longest component length in a cell (30)). The cell with the minimum Fusion1
704 value was identified for the HF-cells group, and the network with the maximum [CRL mito-Net]
705 value within this cell was used as a threshold to demarcate the boundary between the SMN and
706 HMN zones. The same threshold was used for all analyses after confirming the distribution of the
707 length parameters for networks and non-networks.

708 **Single-Cell RNA Seq Analyses and hdWGCNA :** TCDD exposed cells were processed for
709 scRNA-seq using the 10X Genomics platform and analyses was performed using Seurat (v4.3.3),
710 as described before (20). Notably, the cells were tested for > 90% viability before scRNA-seq,
711 and only cells expressing a minimum of 2000 detectable genes were included using
712 'nFeature_RNA' filter. This filtering also excluded dead cells with >10% mtDNA gene expression
713 in all our data sets analyzed. This allowed us to exclude the **percent.mt** filter that uses mtDNA
714 based exclusion of dead cells. Same filters were used for processing publicly available raw data
715 from cSCC patients (67). Seurat objects were processed, integrated, visualized and analysed for
716 relevant downstream analyses including pairwise differential gene expression analyses (using
717 FindMarkers function), cell cluster analyses (using FindAllMarkers function) and Gene Set
718 Enrichment Analysis (GSEA) for cell cluster annotation, using workflow described before (20, 44)
719 **(Suppl Data 2-3).**

720 We applied hdWGCNA method on scRNA-seq data to identifies transcriptomic networks
721 (94) (95) following the workflow outlined in **Fig. S10** (also see Suppl Methods). We used
722 integrated Seurat objects for both pseudobulk and cell cluster based analyses, considered the top
723 20 / 25 genes (ranked by kME) to visualize transcriptomic interactions through hub-gene network
724 plots. Functional annotation of the hdWGCNA modules was performed using GSEA where the
725 modules with ≥ 5 mtDNA genes as the leading-edge genes were reassigned as 'mtDNA' in our
726 analyses. Edge distance and the number of edges were quantified using TOM, providing insights
727 into gene connectivity and interaction strength within the network.

Statistical Analyses: Individual experiments were performed at least 3 times, and appropriate statistics were applied. Appropriate statistical analyses for single cell microscopy were conducted using either Excel or Python (SciPy); The Kolmogorov-Smirnov test was applied to histogram and ridge plots; the Mann-Whitney U test to violin and box plots; and the Chi-square test to bivariate scatter plots. Corresponding p-values were calculated and adjusted for multiple hypotheses testing using the Holm-Bonferroni correction method. The hdWGCNA used inbuilt statistical analyses as required.

Data Availability: The waw, analyzed and meta data of scRNA-seq experiment have been deposited in the Gene expression Omnibus (accession number awaited). All data matrices, scripts, and hdWGCNA results will be deposited in public repositories upon publication, to ensure transparency and reproducibility for future research.

Acknowledgments: The research was supported by NIH (R33 ES025662/ES/NIEHS) and DBT-Wellcome Trust India Alliance (IA/S/20/2/505198/WTDBT); D.P. and B.S. were supported by NIH (R33 ES025662/ES/NIEHS), S.A. was supported by DBTRA/2023-24/NE/Ashoka/19; M.S. was supported by DBT-JRF- DBT/2023-24/Ashoka Uni/2196; B.W. was supported by DBT-Wellcome Trust India Alliance (IA/S/20/2/505198/WTDBT); B.G. was supported by DBT/2022-23/ASHOKA/2156. We acknowledge UAB Flow Cytometry and Single Cell Services Core (supported by P30 AR048311, P30 AI027667) and the Dr. Mike Crowley from the Heflin Genomics Core for scRNA-seq, We sincerely thank Akshara Kulkarni, Diya Prasad for their assistance in the execution of the project, and Dr. LS Shashidhara, Dr. Alok Bhattacharya and Dr. Gautam Menon for critically reading the manuscript.

751 ## References

752

753 1. A. Suomalainen, J. Nunnari, Mitochondria at the crossroads of health and disease. *Cell* **187**,
754 2601–2627 (2024).

755 2. C. R. Reczek, N. S. Chandel, ROS-dependent signal transduction. *Curr Opin Cell Biol* **33**, 8
756 (2015).

757 3. S. Agarwala, S. Dhabal, K. Mitra, Significance of quantitative analyses of the impact of
758 heterogeneity in mitochondrial content and shape on cell differentiation. *Open Biol* **14** (2024).

759 4. M. Granath-Panelo, S. Kajimura, Mitochondrial heterogeneity and adaptations to cellular
760 needs. *Nat Cell Biol* **26**, 674–686 (2024).

761 5. S. B. Vafai, V. K. Mootha, Mitochondrial disorders as windows into an ancient organelle.
762 *Nature* **491**, 374–383 (2012).

763 6. I. Martínez-Reyes, N. S. Chandel, Cancer metabolism: looking forward. *Nat Rev Cancer* **21**,
764 669–680 (2021).

765 7. S. Vyas, E. Zaganjor, M. C. Haigis, Mitochondria and Cancer. *Cell* **166**, 555–566 (2016).

766 8. J. J. Loh, S. Ma, Hallmarks of cancer stemness. *Cell Stem Cell* **31**, 617–639 (2024).

767 9. B. C. Prager, Q. Xie, S. Bao, J. N. Rich, Cancer Stem Cells: The Architects of the Tumor
768 Ecosystem. *Cell Stem Cell* **24**, 41–53 (2019).

769 10. C. L. Jones, A. Inguva, C. T. Jordan, Targeting Energy Metabolism in Cancer Stem Cells:
770 Progress and Challenges in Leukemia and Solid Tumors. *Cell Stem Cell* **28**, 378–393 (2021).

771 11. K. Vasan, M. Werner, N. S. Chandel, Mitochondrial Metabolism as a Target for Cancer
772 Therapy. *Cell Metab* **32**, 341–352 (2020).

773 12. B. Spurlock, J. M. A. Tullet, J. L. Hartman, K. Mitra, Interplay of mitochondrial fission-fusion
774 with cell cycle regulation: Possible impacts on stem cell and organismal aging. *Exp Gerontol*
775 **135**, 110919 (2020).

776 13. B. Glancy, Y. Kim, P. Katti, T. B. Willingham, The Functional Impact of Mitochondrial
777 Structure Across Subcellular Scales. *Front Physiol* [Preprint] (2020).

778 14. K. W. Ryu, *et al.*, Cellular ATP demand creates metabolically distinct subpopulations of
779 mitochondria. *Nature 2024* 1–9 (2024). https://doi.org/10.1038/s41586-024-08146-w.

780 15. R. Quintana-Cabrera, L. Scorrano, Determinants and outcomes of mitochondrial dynamics.
781 *Mol Cell* [Preprint] (2023).

782 16. D. C. Chan, Mitochondrial Dynamics and Its Involvement in Disease. *Annual Review of*
783 *Pathology: Mechanisms of Disease* **15**, 235–259 (2020).

784 17. L. C. Tábara, M. Segawa, J. Prudent, Molecular mechanisms of mitochondrial dynamics.
785 *Nature Reviews Molecular Cell Biology 2024* 1–24 (2024). https://doi.org/10.1038/s41580-024-
786 00785-1.

787 18. M. Song, K. Mihara, Y. Chen, L. Scorrano, G. W. Dorn, Mitochondrial fission and fusion
788 factors reciprocally orchestrate mitophagic culling in mouse hearts and cultured fibroblasts.
789 *Cell Metab* **21**, 273–286 (2015).

790 19. J. Prieto, *et al.*, Early ERK1/2 activation promotes DRP1-dependent mitochondrial fission
791 necessary for cell reprogramming. *Nat Commun* **7** (2016).

792 20. B. Spurlock, *et al.*, Fine-tuned repression of Drp1-driven mitochondrial fission primes a
793 "stem/progenitor-like state" to support neoplastic transformation. *Elife* **10** (2021).

794 21. X. Zhong, *et al.*, Mitochondrial Dynamics Is Critical for the Full Pluripotency and Embryonic
795 Developmental Potential of Pluripotent Stem Cells. *Cell Metab* **29**, 979-992.e4 (2019).

796 22. K. Mitra, C. Wunder, B. Roysam, G. Lin, J. Lippincott-Schwartz, A hyperfused mitochondrial
797 state achieved at G1-S regulates cyclin E buildup and entry into S phase. *Proc Natl Acad Sci*
798 *U S A* **106**, 11960–11965 (2009).

799 23. S. M. Rafelski, *et al.*, Mitochondrial Network Size Scaling in Budding Yeast. *Science* **338**, 822
800 (2012).

801 24. M. Ouellet, G. Guillebaud, V. Gervais, D. Lupien St-Pierre, M. Germain, A novel algorithm
802 identifies stress-induced alterations in mitochondrial connectivity and inner membrane
803 structure from confocal images. *PLoS Comput Biol* **13**, 1–23 (2017).

804 25. H. S. Ilamathi, *et al.*, A new automated tool to quantify nucleoid distribution within
805 mitochondrial networks. *Scientific Reports 2021 11:1* **11**, 1–14 (2021).

806 26. A. Rohani, J. A. Kashatus, D. T. Sessions, S. Sharmin, D. F. Kashatus, Mito Hacker: a set of
807 tools to enable high-throughput analysis of mitochondrial network morphology. *Sci Rep* **10**
808 (2020).

809 27. M. Karbowski, *et al.*, Quantitation of mitochondrial dynamics by photolabeling of individual
810 organelles shows that mitochondrial fusion is blocked during the Bax activation phase of
811 apoptosis. *J Cell Biol* **164**, 493–499 (2004).

812 28. E. F. Iannetti, J. A. M. Smeitink, J. Beyrath, P. H. G. M. Willems, W. J. H. Koopman,
813 Multiplexed high-content analysis of mitochondrial morphofunction using live-cell microscopy.
814 *Nature Protocols 2016 11:9* **11**, 1693–1710 (2016).

815 29. A. E. Y. T. Lefebvre, D. Ma, K. Kessenbrock, D. A. Lawson, M. A. Digman, Automated
816 segmentation and tracking of mitochondria in live-cell time-lapse images. *Nat Methods* **18**,
817 1091–1102 (2021).

818 30. B. Spurlock, *et al.*, New quantitative approach reveals heterogeneity in mitochondrial
819 structure–function relations in tumor-initiating cells. *J Cell Sci* **132** (2019).

820 31. R. Liang, *et al.*, Restraining Lysosomal Activity Preserves Hematopoietic Stem Cell
821 Quiescence and Potency. *Cell Stem Cell* **26**, 359-376.e7 (2020).

822 32. F. Bonnay, *et al.*, Oxidative Metabolism Drives Immortalization of Neural Stem Cells during
823 Tumorigenesis. *Cell* **182**, 1490-1507.e19 (2020).

824 33. M. J. Wu, *et al.*, Epithelial-Mesenchymal Transition Directs Stem Cell Polarity via Regulation
825 of Mitofusin. *Cell Metab* **29**, 993-1002.e6 (2019).

826 34. L. Perez-Castro, *et al.*, The AHR target gene scinderin activates the WNT pathway by
827 facilitating the nuclear translocation of β-catenin. *J Cell Sci* **135** (2022).

828 35. I. Teino, *et al.*, Impact of AHR Ligand TCDD on Human Embryonic Stem Cells and Early
829 Differentiation. *Int J Mol Sci* **21**, 1–24 (2020).

830 36. A. Der Vartanian, *et al.*, PAX3 Confers Functional Heterogeneity in Skeletal Muscle Stem Cell
831 Responses to Environmental Stress. *Cell Stem Cell* **24**, 958-973.e9 (2019).

832 37. K. P. Singh, F. L. Casado, L. A. Opanashuk, T. A. Gasiewicz, The aryl hydrocarbon receptor
833 has a normal function in the regulation of hematopoietic and other stem/progenitor cell
834 populations. *Biochem Pharmacol* [Preprint] (2009).

835 38. S. Kim, E. Dere, L. D. Burgoon, C. C. Chang, T. R. Zacharewski, Comparative analysis of
836 AhR-mediated TCDD-elicited gene expression in human liver adult stem cells. *Toxicological*
837 *Sciences* **112**, 229–244 (2009).

838 39. V. Shukla, K. Iqbal, H. Okae, T. Arima, M. J. Soares, EFFECTS OF ARYL HYDROCARBON
839 RECEPTOR LIGAND TCDD ON HUMAN TROPHOBLAST CELL DEVELOPMENT. *bioRxiv*
840 (2024). https://doi.org/10.1101/2024.08.27.609205.

841 40. J. A. Kashatus, *et al.*, Erk2 phosphorylation of Drp1 promotes mitochondrial fission and
842 MAPK-driven tumor growth. *Mol Cell* **57**, 537–551 (2015).

843 41. M. N. Serasinghe, *et al.*, Mitochondrial division is requisite to RAS-induced transformation and
844 targeted by oncogenic MAPK pathway inhibitors. *Mol Cell* **57**, 521 (2015).

845 42. D. Tondera, *et al.*, SLP-2 is required for stress-induced mitochondrial hyperfusion. *EMBO J*
846 **28**, 1589–1600 (2009).

847 43. L. C. Gomes, G. Di Benedetto, L. Scorrano, During autophagy mitochondria elongate, are
848 spared from degradation and sustain cell viability. *Nat Cell Biol* **13**, 589–598 (2011).

849 44. S. Agarwala, M. Saini, D. Parker, K. Mitra, Enrichment of carcinogen-driven “mitochondria-
850 primed” human skin stem cells and their identification using single-cell analyses. *STAR Protoc*
851 **4** (2023).

852 45. B. Spurlock, V. S. Hanumanthu, K. Mitra, Strategy of isolating “primed” tumor initiating cells
853 based on mitochondrial transmembrane potential. *Bio Protoc* **11** (2021).

854 46. T. S. Purba, *et al.*, Human epithelial hair follicle stem cells and their progeny: Current state of
855 knowledge, the widening gap in translational research and future challenges. *BioEssays* **36**,
856 513–525 (2014).

857 47. A. R. Fenton, T. A. Jongens, E. L. F. Holzbaur, Mitochondrial dynamics: Shaping and
858 remodeling an organelle network. *Curr Opin Cell Biol* **68**, 28–36 (2021).

859 48. L. B. Sullivan, N. S. Chandel, Mitochondrial reactive oxygen species and cancer. *Cancer*
860 *Metab* **2**, 17 (2014).

861 49. C. L. Bigarella, R. Liang, S. Ghaffari, Stem cells and the impact of ROS signaling.
862 *Development (Cambridge)* **141**, 4206–4218 (2014).

863 50. A. Poland, D. Palen, E. Glover, Tumour promotion by TCDD in skin of HRS/J hairless mice.
864 *Nature* **300**, 271–273 (1982).

865 51. J. Huff, G. Lucier, A. Tritscher, Carcinogenicity of TCDD: experimental, mechanistic, and
866 epidemiologic evidence. *Annu Rev Pharmacol Toxicol* **34**, 343–372 (1994).

867 52. R. Baan, *et al.*, A review of human carcinogens--Part F: chemical agents and related
868 occupations. *Lancet Oncol* **10**, 1143–1144 (2009).

869 53. T. J. Dunn, R. Lindahl, H. C. Pitot, Differential gene expression in response to 2,3,7,8-
870 tetrachlorodibenzo-p-dioxin (TCDD). Noncoordinate regulation of a TCDD-induced aldehyde
871 dehydrogenase and cytochrome P-450c in the rat. *Journal of Biological Chemistry* **263**,
872 10878–10886 (1988).

873 54. P. DiMeglio, *et al.*, Activation of the Aryl Hydrocarbon Receptor Dampens the Severity of
874 Inflammatory Skin Conditions. *Immunity* **40**, 989 (2014).

875 55. S. Rath, *et al.*, MitoCarta3.0: an updated mitochondrial proteome now with sub-organelle
876 localization and pathway annotations. *Nucleic Acids Res* **49**, D1541–D1547 (2021).

877 56. H. Liu, *et al.*, Prohibitin 1 regulates mtDNA release and downstream inflammatory responses .
878 *EMBO J* **41** (2022).

879 57. K. Kasashima, M. Sumitani, M. Satoh, H. Endo, Human prohibitin 1 maintains the
880 organization and stability of the mitochondrial nucleoids. *Exp Cell Res* **314**, 988–996 (2008).

881 58. T. Tatsuta, T. Langer, Prohibitins. *Current Biology* **27**, R629–R631 (2017).

882 59. C. Von Ballmoos, A. Wiedenmann, P. Dimroth, Essentials for ATP synthesis by F1F0 ATP
883 synthases. *Annu Rev Biochem* **78**, 649–672 (2009).

884 60. V. Fogal, *et al.*, Mitochondrial p32 Protein Is a Critical Regulator of Tumor Metabolism via
885 Maintenance of Oxidative Phosphorylation. *Mol Cell Biol* **30**, 1303 (2010).

886 61. M. Yagi, *et al.*, p32/gC1qR is indispensable for fetal development and mitochondrial
887 translation: importance of its RNA-binding ability. *Nucleic Acids Res* **40**, 9717 (2012).

888 62. M. P. Murphy, How mitochondria produce reactive oxygen species. *Biochem J* **417**, 1–13
889 (2009).

890 63. M. Moriyama, *et al.*, Multiple roles of Notch signaling in the regulation of epidermal
891 development. *Dev Cell* **14**, 594–604 (2008).

892 64. L. Sang, H. A. Coller, J. M. Roberts, Control of the reversibility of cellular quiescence by the
893 transcriptional repressor HES1. *Science* **321**, 1095–1100 (2008).

894 65. J. A. Irving, R. N. Pike, A. M. Lesk, J. C. Whisstock, Phylogeny of the serpin superfamily:
895 implications of patterns of amino acid conservation for structure and function. *Genome Res*
896 **10**, 1845–1864 (2000).

897 66. R. S. Esworthy, J. H. Doroshow, F. F. Chu, The beginning of GPX2 and 30 years later. *Free*
898 *Radic Biol Med* **188**, 419 (2022).

899 67. A. L. Ji, *et al.*, Multimodal Analysis of Composition and Spatial Architecture in Human
900 Squamous Cell Carcinoma. *Cell* **182**, 497-514.e22 (2020).

901 68. W. Chen, H. Zhao, Y. Li, Mitochondrial dynamics in health and disease: mechanisms and
902 potential targets. *Signal Transduction and Targeted Therapy 2023 8:1* **8**, 1–25 (2023).

903 69. D. C. Chan, Mitochondrial Dynamics and Its Involvement in Disease. *Annu Rev Pathol* **15**,
904 235–259 (2020).

905 70. M. P. Viana, *et al.*, Mitochondrial Fission and Fusion Dynamics Generate Efficient, Robust,
906 and Evenly Distributed Network Topologies in Budding Yeast Cells. *Cell Syst* **10**, 287-297.e5
907 (2020).

908 71. B. Glancy, *et al.*, Mitochondrial reticulum for cellular energy distribution in muscle. *Nature* **523**,
909 617–620 (2015).

910 72. J. Nunnari, *et al.*, Mitochondrial transmission during mating in Saccharomyces cerevisiae is
911 determined by mitochondrial fusion and fission and the intramitochondrial segregation of
912 mitochondrial DNA. *Mol Biol Cell* **8**, 1233–1242 (1997).

913 73. A. Kowald, T. B. L. Kirkwood, Evolution of the mitochondrial fusion - Fission cycle and its role
914 in aging. *Proc Natl Acad Sci U S A* **108**, 10237–10242 (2011).

915 74. R. Sênos Demarco, B. S. Uyemura, C. D'Alterio, D. L. Jones, Mitochondrial fusion regulates
916 lipid homeostasis and stem cell maintenance in the Drosophila testis. *Nat Cell Biol* **21**, 710–
917 720 (2019).

918 75. M. Khacho, *et al.*, Mitochondrial Dynamics Impacts Stem Cell Identity and Fate Decisions by
919 Regulating a Nuclear Transcriptional Program. *Cell Stem Cell* **19**, 232–247 (2016).

920 76. R. Iwata, P. Casimir, P. Vanderhaeghen, Mitochondrial dynamics in postmitotic cells regulate
921 neurogenesis. *Science* **369**, 858–862 (2020).

922 77. H. Liu, *et al.*, Prohibitin 1 regulates mtDNA release and downstream inflammatory responses.
923 *EMBO J* **41** (2022).

924 78. G. Della-Flora Nunes, *et al.*, Prohibitin 1 is essential to preserve mitochondria and myelin
925 integrity in Schwann cells. *Nature Communications 2021 12:1* **12**, 1–16 (2021).

926 79. M. J. Birket, *et al.*, A reduction in ATP demand and mitochondrial activity with neural
927 differentiation of human embryonic stem cells. *J Cell Sci* **124**, 348–358 (2011).

928 80. J. M. Facucho-Oliveira, J. C. John St., The relationship between pluripotency and
929 mitochondrial DNA proliferation during early embryo development and embryonic Stem Cell
930 differentiation. *Stem Cell Rev Rep* **5**, 140–158 (2009).

931 81. K. M. Holmström, T. Finkel, Cellular mechanisms and physiological consequences of redox-
932 dependent signalling. *Nature Reviews Molecular Cell Biology 2014 15:6* **15**, 411–421 (2014).

933 82. P. H. G. M. Willems, R. Rossignol, C. E. J. Dieteren, M. P. Murphy, W. J. H. Koopman, Redox
934 Homeostasis and Mitochondrial Dynamics. *Cell Metab* **22**, 207–218 (2015).

935 83. W. Wang, *et al.*, Superoxide flashes in single mitochondria. *Cell* **134**, 279–290 (2008).

936 84. Z. Ying, *et al.*, Transient Activation of Mitoflashes Modulates Nanog at the Early Phase of
937 Somatic Cell Reprogramming. *Cell Metab* **23**, 220–226 (2016).

938 85. C. E. Bauer, S. Elsen, T. H. Bird, Mechanisms for redox control of gene expression. *Annu*
939 *Rev Microbiol* **53**, 495–523 (1999).

940 86. M. Fratelli, *et al.*, Gene expression profiling reveals a signaling role of glutathione in redox
941 regulation. *Proc Natl Acad Sci U S A* **102**, 13998–14003 (2005).

942 87. H. Y. Hsu, M. H. Wen, Lipopolysaccharide-mediated reactive oxygen species and signal
943 transduction in the regulation of interleukin-1 gene expression. *Journal of Biological Chemistry*
944 **277**, 22131–22139 (2002).

945 88. J. Chiu, I. W. Dawes, Redox control of cell proliferation. *Trends Cell Biol* **22**, 592–601 (2012).

946 89. J. C. Patterson, *et al.*, ROS and Oxidative Stress Are Elevated in Mitosis during
947 Asynchronous Cell Cycle Progression and Are Exacerbated by Mitotic Arrest. *Cell Syst* **8**, 163-
948 167.e2 (2019).

949 90. D. G. Kirova, *et al.*, A ROS-dependent mechanism promotes CDK2 phosphorylation to drive
950 progression through S phase. *Dev Cell* **57**, 1712 (2022).

951 91. D. P. Byrne, *et al.*, Aurora A regulation by reversible cysteine oxidation reveals evolutionarily
952 conserved redox control of Ser/Thr protein kinase activity. *Sci Signal* **13** (2020).

953 92. S. G. Menon, *et al.*, “Redox Regulation of the G 1 to S Phase Transition in the Mouse Embryo
954 Fibroblast Cell Cycle 1” (2003).

955 93. C. T. J. van Velthoven, T. A. Rando, Stem Cell Quiescence: Dynamism, Restraint, and
956 Cellular Idling. *Cell Stem Cell* **24**, 213–225 (2019).

957 94. S. Horvath, J. Dong, Geometric interpretation of gene coexpression network analysis. *PLoS*
958 *Comput Biol* **4** (2008).

959 95. S. Morabito, F. Reese, N. Rahimzadeh, E. Miyoshi, V. Swarup, hdWGCNA identifies co-
960 expression networks in high-dimensional transcriptomics data. *Cell Reports Methods* **3** (2023).

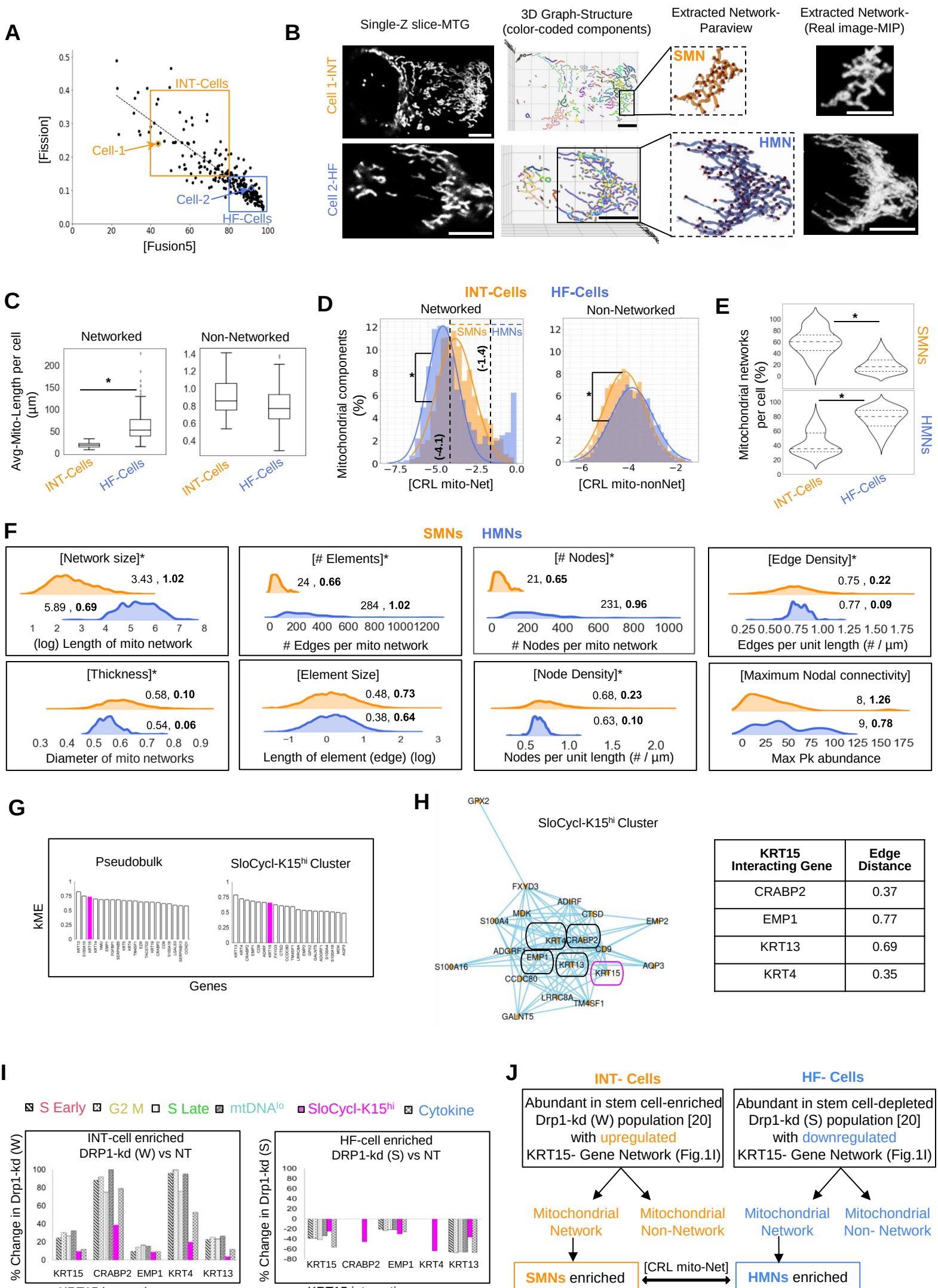
A
INT-Cells
Cell-1
Cell-2
HF-Cells
[Fission]
[Fusion5]
B
Single-Z slice-MTG
3D Graph-Structure (color-coded components)
Extracted Network-Paraview
Extracted Network-(Real image-MIP)
Cell 1-INT
Cell 2-HF
SMN
HMN
C
Avg-Mito-Length per cell (µm)
Networked
Non-Networked
INT-Cells
HF-Cells
D
INT-Cells
HF-Cells
Networked
Non-Networked
SMNs
HMNs
(-1.4)
(-4.1)
Mitochondrial components (%)
[CRL mito-Net]
[CRL mito-nonNet]
E
Mitochondrial networks per cell (%)
SMNs
HMNs
INT-Cells
HF-Cells
F
SMNs
HMNs
[Network size]*
3.43 , 1.02
5.89 , 0.69
(log) Length of mito network
[# Elements]*
24 , 0.66
284 , 1.02
Edges per mito network
[# Nodes]*
21, 0.65
231, 0.96
Nodes per mito network
[Edge Density]*
0.75 , 0.22
0.77 , 0.09
Edges per unit length (# / µm)
[Thickness]*
0.58, 0.10
0.54, 0.06
Diameter of mito networks
[Element Size]
0.48, 0.73
0.38, 0.64
Length of element (edge) (log)
[Node Density]*
0.68, 0.23
0.63, 0.10
Nodes per unit length (# / µm)
[Maximum Nodal connectivity]
8, 1.26
9, 0.78
Max Pk abundance
G
Pseudobulk
SloCycl-K15hi Cluster
kME
Genes
H
SloCycl-K15hi Cluster
GPX2
FXYD3
ADIRF
MDK
CTSD
S100A4
EMP2
KRT4
CRABP2
ADGRF1
CD9
EMP1
KRT13
S100A16
AQP3
KRT15
CCDC80
LRRC8A
TM4SF1
GALNT5
KRT15 Interacting Gene | Edge Distance
CRABP2 | 0.37
EMP1 | 0.77
KRT13 | 0.69
KRT4 | 0.35
I
S Early
G2 M
S Late
mtDNAlo
SloCycl-K15hi
Cytokine
INT-cell enriched DRP1-kd (W) vs NT
HF-cell enriched DRP1-kd (S) vs NT
% Change in Drp1-kd (W)
% Change in Drp1-kd (S)
KRT15
CRABP2
EMP1
KRT4
KRT13
KRT15 interacting genes
J
INT- Cells
HF- Cells
Abundant in stem cell-enriched Drp1-kd (W) population [20] with upregulated KRT15- Gene Network (Fig.1I)
Abundant in stem cell-depleted Drp1-kd (S) population [20] with downregulated KRT15- Gene Network (Fig.1I)
Mitochondrial Network
Mitochondrial Non-Network
Mitochondrial Network
Mitochondrial Non- Network
SMNs enriched
[CRL mito-Net]
HMNs enriched

Fig.1

Figure. 1: Single mitochondrial analyses identify and characterize the physical Small-Mitochondrial-Networks that are linked to stemness transcriptomic networks. A. Scatter plot of [Fission] versus [Fusion5] metrics from mito-SinCe analysis of individual cells stained with Mitotracker Green in a combined population with varying levels of Drp-1 knockdown {re-analysed from (20)}; range for INT-cells and HF-cells are demarcated by coloured boxes. **B.** Representative images of single cells from INT-Cells and HF-Cells populations marked in **A**; Single optical slices and 3D graph from mito-SinComp analysis with networks are shown. The sample SMN and HMN were magnified and visualized using ParaView software from Cell 1-INT and Cell 2-HF, respectively, with corresponding network cut out from the raw image. Scale bar: 5 µm. **C.** Box plot of Avg-Mito-Length per cell of networked and non-networked mitochondria in INT and HF groups. **D.** Histogram distribution of [CRL mito-Net] or [CRL mito-nonNet], with demarcation of thresholds (dashed line) for SMNs (−4.1 to −1.4) and HMNs (≥−1.4) in the network plot (see Methods for details) **E.** Violin plot of mitochondrial networks per cell in the SMN and HMN categories in INT and HF groups, with median (dashed line) and the quartile ranges (dotted lines) shown. **F.** Ridgeline plot comparing the distribution of structural parameters between SMNs and HMNs (see Supplementary methods for the description of the parameters); Median and Coefficient of Variation are indicated for each parameter, latter in bold. **G.** kME plot of KRT15 transcriptomic interaction modules, identified using hdWGCNA, of the Drp1-kd (W) and Drp1-kd (S) datasets compared to NT control {original data published in (20)}. **H.** Hub-Gene Network Plot of the SloCycl-K15^{hi} module identified in **G**, with direct KRT15 transcriptomic connections are outlined (left). The table shows edge distance of KRT15 with its direct connections. **I.** Bar plots showing percentage change in median values for INT group enriched DRP1-kd (W) and HF-cell enriched DRP1-kd (S) with respect to control, NT across colour-coded cell clusters. **J.** Schematic of the summary of mito-SinComp structural analyses **(B-F)** and scRNA-seq analyses **(G-I)** of the combined population with varying levels of Drp-1 knockdown. (* signifies Holmes-Bonferroni corrected p-value < 0.05).

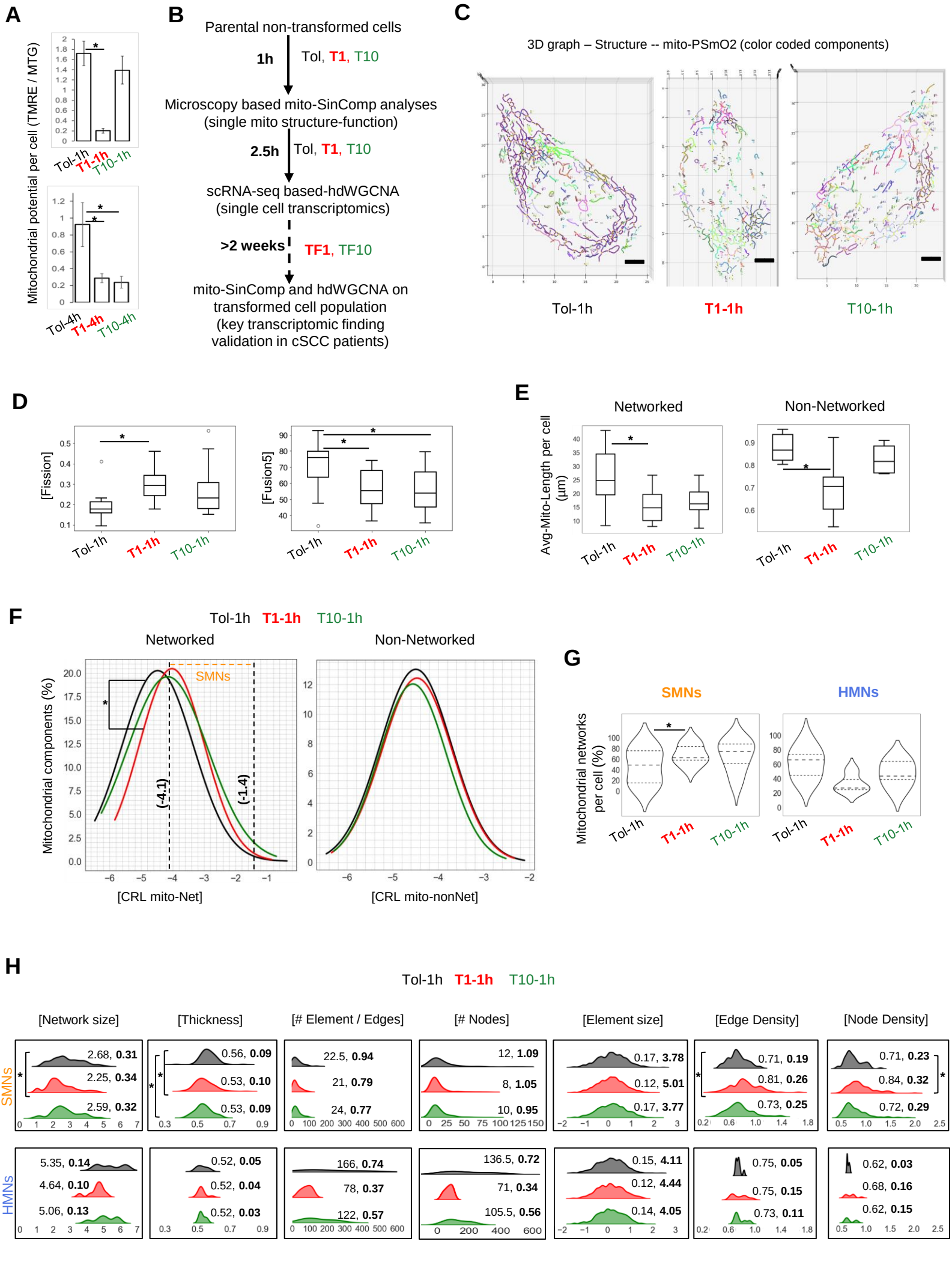
A
Mitochondrial potential per cell (TMRE / MTG)
Tol-1h
T1-1h
T10-1h
Tol-4h
T1-4h
T10-4h
B
Parental non-transformed cells
1h
Tol, T1, T10
Microscopy based mito-SinComp analyses
(single mito structure-function)
2.5h
Tol, T1, T10
scRNA-seq based-hdWGCNA
(single cell transcriptomics)
>2 weeks
TF1, TF10
mito-SinComp and hdWGCNA on
transformed cell population
(key transcriptomic finding
validation in cSCC patients)
C
3D graph – Structure -- mito-PSmO2 (color coded components)
Tol-1h
T1-1h
T10-1h
D
[Fission]
[Fusion5]
Tol-1h
T1-1h
T10-1h
E
Networked
Non-Networked
Avg-Mito-Length per cell (µm)
Tol-1h
T1-1h
T10-1h
F
Tol-1h T1-1h T10-1h
Networked
Non-Networked
SMNs
Mitochondrial components (%)
(-4.1)
(-1.4)
[CRL mito-Net]
[CRL mito-nonNet]
G
SMNs
HMNs
Mitochondrial networks per cell (%)
Tol-1h
T1-1h
T10-1h
H
Tol-1h T1-1h T10-1h
[Network size]
[Thickness]
[# Element / Edges]
[# Nodes]
[Element size]
[Edge Density]
[Node Density]
SMNs
HMNs
2.68, 0.31
2.25, 0.34
2.59, 0.32
0.56, 0.09
0.53, 0.10
0.53, 0.09
22.5, 0.94
21, 0.79
24, 0.77
12, 1.09
8, 1.05
10, 0.95
0.17, 3.78
0.12, 5.01
0.17, 3.77
0.71, 0.19
0.81, 0.26
0.73, 0.25
0.71, 0.23
0.84, 0.32
0.72, 0.29
5.35, 0.14
4.64, 0.10
5.06, 0.13
0.52, 0.05
0.52, 0.04
0.52, 0.03
166, 0.74
78, 0.37
122, 0.57
136.5, 0.72
71, 0.34
105.5, 0.56
0.15, 4.11
0.12, 4.44
0.14, 4.05
0.75, 0.05
0.75, 0.15
0.73, 0.11
0.62, 0.03
0.68, 0.16
0.62, 0.15

Fig. 2

Figure. 2: Acute-1h exposure to stem cell enriching carcinogen depolarizes mitochondria and converts hyperfused mitochondrial networks (HMNs) to more complex small mitochondrial networks (SMNs). A. Mitochondrial potential per cell measured as the ratio of TMRE to MTG signal from individual HaCaT cells from confocal micrographs of Tol, T1-1h, T10-1h (top) and Tol, T1-4h, T10-4h (bottom) groups. **B.** Schematic of the experimental regime using mito-SinComp and scRNA-seq analyses for studying acute impact of TCDD exposure that leads to eventual neoplastic transformation. **C.** Representative 3D graph of single cells from mito-SinComp analysis from Tol-1h, T1-1h and T10-1h groups. Scale bar: 5 µm **D.** Box plot of [Fission] and [Fusion5] metrics of individual cells from mito-SinCe analyses of Tol-1h, T1-1h and T10-1h groups. **E.** Box plot of Avg-Mito-Length per cell of networked and non-networked mitochondria from Tol-1h, T1-1hand T10-1h groups. **F.** Histogram distribution of [CRL mito-Net] or [CRL mito-nonNet] metrics, with demarcation of thresholds (dashed line) for SMNs and HMNs in the network plot (as in **Fig. 1D**). **G.** Violin plot of mitochondrial networks per cell in the SMN and HMN categories in Tol-1h, T1-1h and T10-1h groups, with median (dashed line) and the quartile ranges (dotted lines) shown. **H.** Ridgeline plots comparing the distribution of named structural parameters between SMNs and HMNs from Tol-1h, T1-1h and T10-1h groups; Median and Coefficient of Variation are indicated for each parameter, latter in bold. (* signifies Holmes-Bonferroni corrected p-value < 0.05).

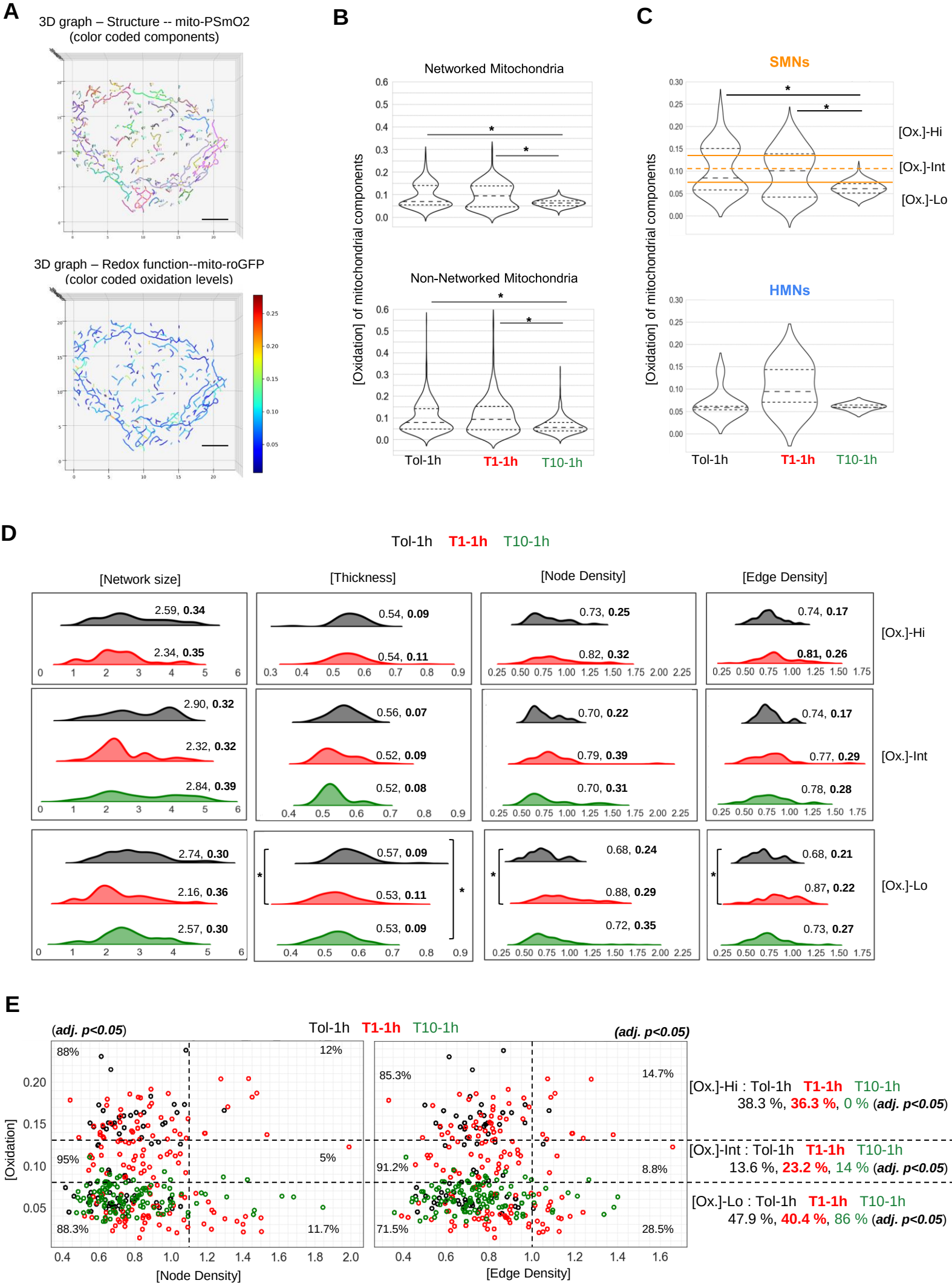
A
3D graph – Structure -- mito-PSmO2
(color coded components)
3D graph – Redox function--mito-roGFP
(color coded oxidation levels)
B
Networked Mitochondria
Non-Networked Mitochondria
[Oxidation] of mitochondrial components
Tol-1h
T1-1h
T10-1h
C
SMNs
HMNs
[Ox.]-Hi
[Ox.]-Int
[Ox.]-Lo
D
Tol-1h T1-1h T10-1h
[Network size]
[Thickness]
[Node Density]
[Edge Density]
2.59, 0.34
2.34, 0.35
0.54, 0.09
0.54, 0.11
0.73, 0.25
0.82, 0.32
0.74, 0.17
0.81, 0.26
2.90, 0.32
2.32, 0.32
2.84, 0.39
0.56, 0.07
0.52, 0.09
0.52, 0.08
0.70, 0.22
0.79, 0.39
0.70, 0.31
0.74, 0.17
0.77, 0.29
0.78, 0.28
2.74, 0.30
2.16, 0.36
2.57, 0.30
0.57, 0.09
0.53, 0.11
0.53, 0.09
0.68, 0.24
0.88, 0.29
0.72, 0.35
0.68, 0.21
0.87, 0.22
0.73, 0.27
E
(adj. p<0.05)
Tol-1h T1-1h T10-1h
(adj. p<0.05)
88%
12%
95%
5%
88.3%
11.7%
85.3%
14.7%
91.2%
8.8%
71.5%
28.5%
[Oxidation]
[Node Density]
[Edge Density]
[Ox.]-Hi : Tol-1h T1-1h T10-1h
38.3 %, 36.3 %, 0 % (adj. p<0.05)
[Ox.]-Int : Tol-1h T1-1h T10-1h
13.6 %, 23.2 %, 14 % (adj. p<0.05)
[Ox.]-Lo : Tol-1h T1-1h T10-1h
47.9 %, 40.4 %, 86 % (adj. p<0.05)

Fig. 3

Figure 3. Acute-1h exposure to stem cell enriching carcinogen sustains an intermediate oxidative status in the SMNs of restricted nodal complexity. A. Representative 3D graphs of single cells from mito-SinComp analyses showing distribution of mitochondrial components (networks and non-networks) colour-coded by structure (top), oxidation levels (bottom) with scale shown. **B.** Violin plot of [Oxidation] of individual mitochondrial components in the networked and non-networked category in Tol-1h, T1-1h and T10-1h groups, with median (dashed line) and the quartile ranges (dotted lines) shown. **C.** Violin plot of [Oxidation] of individual mitochondrial components in SMNs and HMNs category in Tol-1h, T1-1h and T10-1h groups, with median (dashed line) and the quartile ranges (dotted lines) shown; SMNs are divided into three zones based on high, intermediate and low oxidation levels ([Ox.]-Hi, [Ox.]-Int and Ox-Lo) with the criteria described in the appropriate Results section. **D.** Ridgeline plots comparing the distribution of the named structural parameters of SMNs from Tol-1h, T1-1h and T10-1h groups within each of the above three oxidation zones; Median and Coefficient of Variation are indicated for each parameter, latter in bold. **E.** Scatter plot of [Oxidation] vs [Edge/Node density] for individual SMNs in Tol-1h, T1-1h and T10-1h groups. The horizontal and the vertical dashed lines indicate the demarcation of the [Oxidation] and the [Edge/Node Density] zones, respectively. The percentage abundance of SMNs in each zone is mentioned with $p<0.05$, showing Chi-square goodness of fit analysis. (* signifies Holmes-Bonferroni corrected p-value < 0.05).

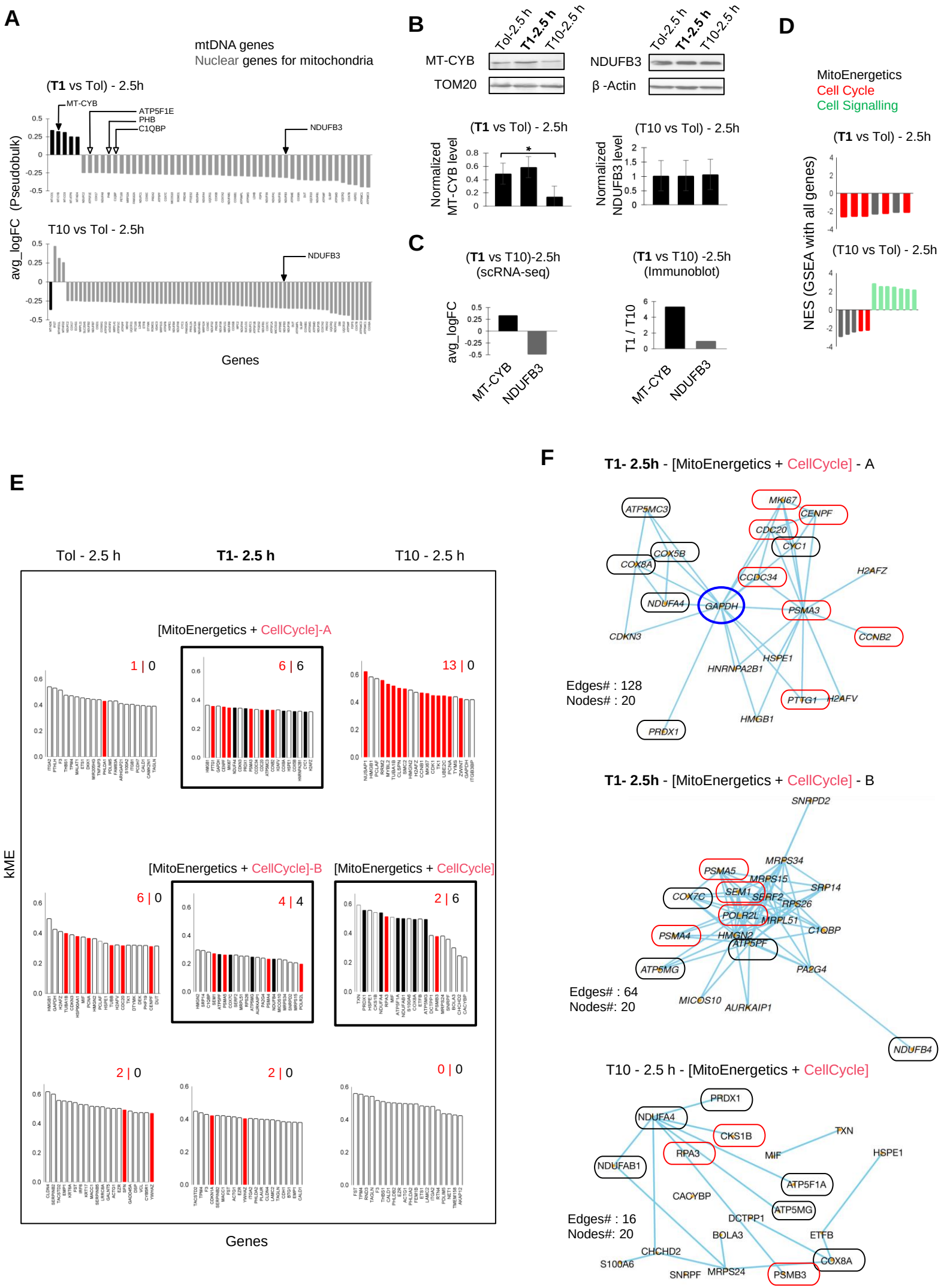
A
mtDNA genes
Nuclear genes for mitochondria
(T1 vs Tol) - 2.5h
MT-CYB
ATP5F1E
PHB
C1QBP
NDUFB3
avg_logFC (Pseudobulk)
T10 vs Tol - 2.5h
NDUFB3
Genes
B
Tol-2.5 h
T1-2.5 h
T10-2.5 h
MT-CYB
TOM20
NDUFB3
β -Actin
(T1 vs Tol) - 2.5h
Normalized MT-CYB level
(T10 vs Tol) - 2.5h
Normalized NDUFB3 level
C
(T1 vs T10)-2.5h (scRNA-seq)
avg_logFC
MT-CYB
NDUFB3
(T1 vs T10) -2.5h (Immunoblot)
T1 / T10
MT-CYB
NDUFB3
D
MitoEnergetics
Cell Cycle
Cell Signalling
(T1 vs Tol) - 2.5h
NES (GSEA with all genes)
(T10 vs Tol) - 2.5h
E
Tol - 2.5 h
T1- 2.5 h
T10 - 2.5 h
[MitoEnergetics + CellCycle]-A
1 | 0
6 | 6
13 | 0
[MitoEnergetics + CellCycle]-B
[MitoEnergetics + CellCycle]
6 | 0
4 | 4
2 | 6
2 | 0
2 | 0
0 | 0
kME
Genes
F
T1- 2.5h - [MitoEnergetics + CellCycle] - A
ATP5MC3
MKI67
CENPF
CDC20
CYC1
COX5B
COX8A
CCDC34
H2AFZ
NDUFA4
GAPDH
PSMA3
CDKN3
CCNB2
HSPE1
HNRNPA2B1
Edges# : 128
Nodes# : 20
PTTG1
H2AFV
HMGB1
PRDX1
T1- 2.5h - [MitoEnergetics + CellCycle] - B
SNRPD2
MRPS34
PSMA5
MRPS15
SRP14
COX7C
SEM1
SRRF2
RPS26
POLR2L
MRPL51
C1QBP
PSMA4
HMGN2
ATP5PF
ATP5MG
PA2G4
Edges# : 64
Nodes#: 20
MICOS10
AURKAIP1
NDUFB4
T10 - 2.5 h - [MitoEnergetics + CellCycle]
PRDX1
NDUFA4
CKS1B
TXN
RPA3
MIF
HSPE1
NDUFAB1
ATP5F1A
CACYBP
ATP5MG
Edges# : 16
Nodes#: 20
DCTPP1
BOLA3
ETFB
CHCHD2
S100A6
COX8A
SNRPF
MRPS24
PSMB3

Fig. 4

Figure 4. Acute-2.5h exposure to stem cell enriching carcinogen upregulates mtDNA genes, while establishing transcriptomic interaction between mitochondrial energetics and cell cycle exit. A. T1-2.5h vs Tol-2.5h and T10-2.5h vs Tol-2.5h pairwise pseudobulk analyses on scRNA-seq data; only expression of genes encoding mitochondrial proteins (MitoCarta) are shown here, with solid triangles indicating MT-CYB and NDUFB3 genes chosen for validation in **B**, while open triangles denote genes uniquely modulated in T1-2.5h **B.** Immunoblot analysis of MT-CYB (left) and NDUFB3 (right), with TOM20 and β-actin as loading controls in Tol-2.5h, T1-2.5h and T10-2.5h groups. Levels of MT-CYB and NDUFB3 were normalized to their respective loading controls (bottom); * signifies p value < 0.05 from Student's t-test. **C.** Pseudobulk analyses from **A** for MT-CYB and NDUFB3 (left) and ratio of relative expression for these molecules in T1 vs T10 from **B** (right). **D.** Normalized Enrichment Scores (NES) from Gene Set Enrichment Analysis (GSEA) of all genes from pseudobulk analyses described in **A**. **E.** kME Plots of all modules identified with hdWGCNA, using all genes from T1-2.5h vs Tol- 2.5h pairwise pseudobulk analysis; [MitoEnergetics + CellCycle] modules are boxed. **F.** Hub-Gene Network plots for the top 20 hub genes of the boxed modules in **E,** with number of edges and nodes indicated, mitochondrial and cell genes are outlined, and GAPDH circled.

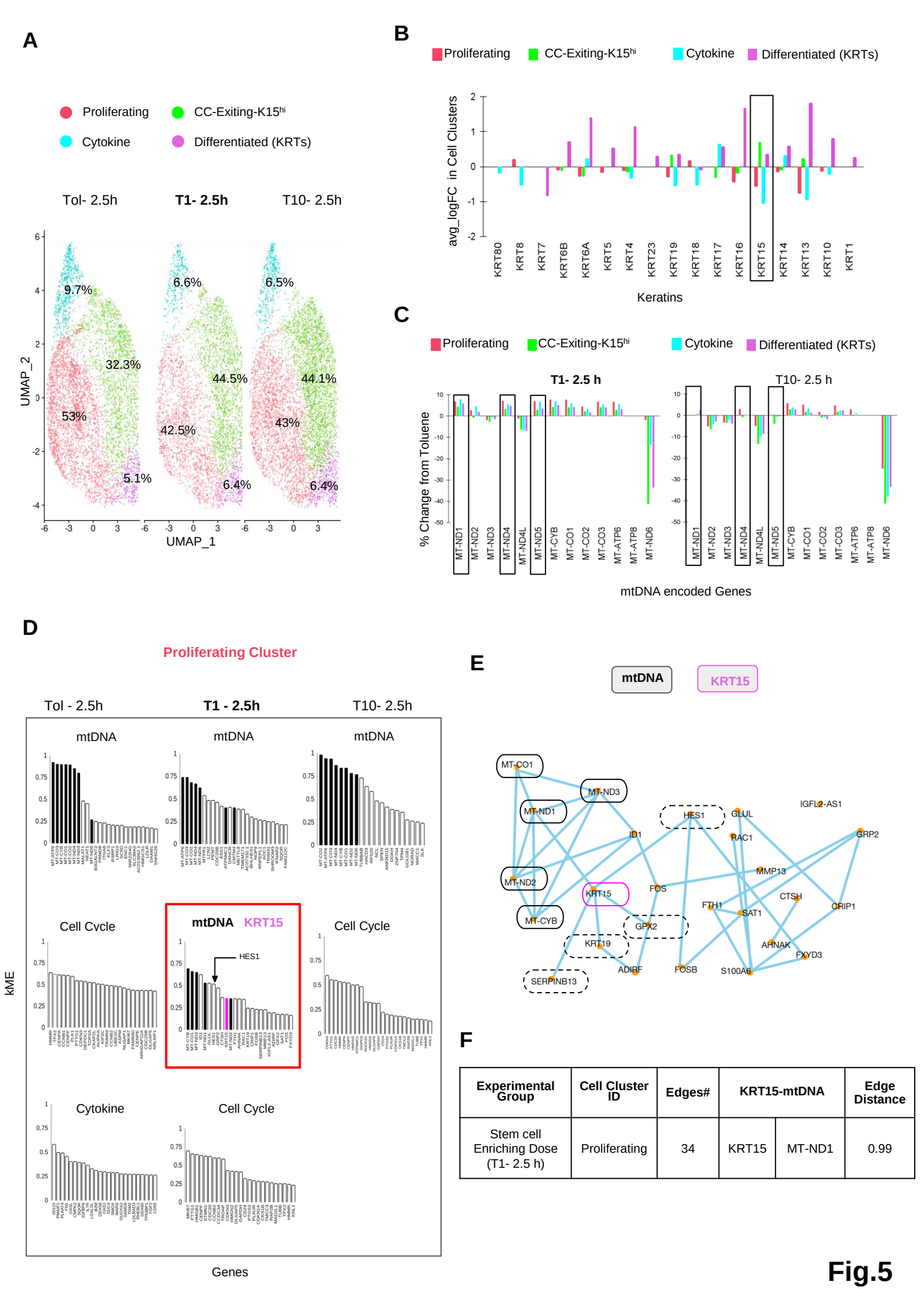

Experimental Group	Cell Cluster ID	Edges#	KRT15-mtDNA		Edge Distance
Stem cell Enriching Dose (T1- 2.5 h)	Proliferating	34	KRT15	MT-ND1	0.99

Fig.5

Figure 5. Acute-2.5h exposure to stem cell enriching carcinogen establishes transcriptomic interaction between mtDNA genes and stemness gene KRT15 in non-transformed proliferating cells prior to their cell cycle exit. A. UMAP plot displaying scRNA-seq derived clusters within cell populations of the Tol-2.5h, T1-2.5h and T10-2.5h groups; the numbers indicate % abundance of cells in each cluster based on **Fig. S6A** and the identity of the clusters are based on top10 marker genes across clusters and GSEA. **B.** Bar plots showing cluster-specific average logFC of all Keratin genes in the named cell clusters, with stem cell-specific KRT15 boxed. (also see **Fig. S6D** for raw data on KRT15). **C.** Bar plots showing percentage change in median expression of mtDNA-encoded genes for T1-2.5h or T10-2.5h groups from Tol-2.5h group across clusters (also see **Fig. S6C** for raw data); MT-ND1 is boxed. **D.** kME plots showing transcriptomic interaction modules obtained using hdWGCNA, which were functionally annotated using GSEA; the modules of Proliferating cluster are shown where interaction between mtDNA genes and KRT15 is detected (boxed). **E.** Hub-Gene Network plot displaying the top 25 genes from the boxed module identified in **D**; Nodes of mtDNA-encoded genes, KRT15 and its directly interacting genes are outlined. **F.** Table displaying edge number and distance for the direct transcriptomic connection between KRT15 and MT-ND1 from **E**.

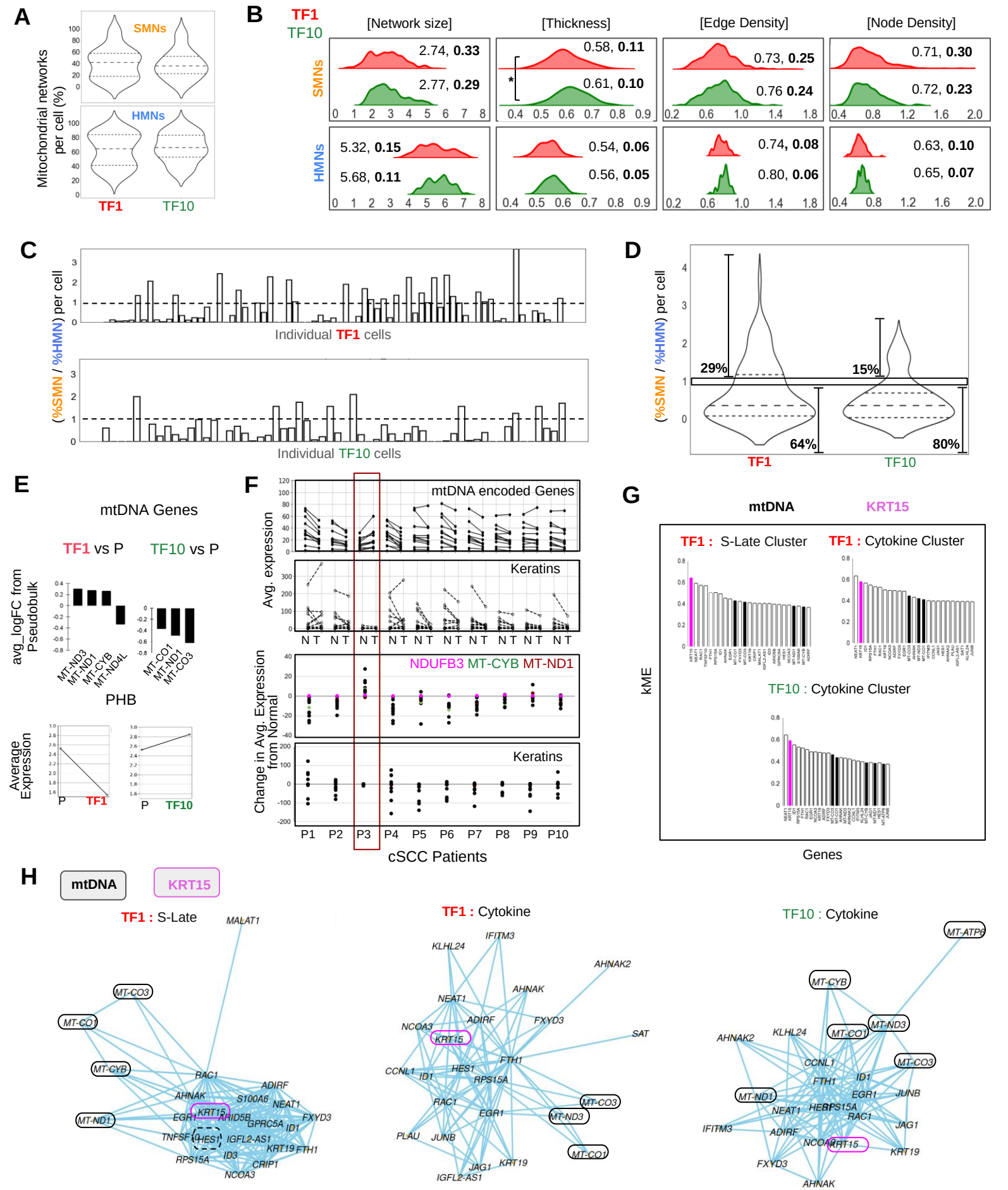

I

Experimental Group	Cell Cluster ID	Edges #	KRT15-direct connections (only relevant ones mentioned)		Edge Distance
TF1 (enriched with SMN and stem cells)	S Late	310	KRT15	MT-CYB	0.99
				MT-ND1	0.99
				HES1	0.44
	Cytokine	159	No mtDNA or HES1 connection		
TF10	Cytokine	210	Only HES1 connection		

Fig. 6

Figure 6. Transformation with stem cell enriching carcinogen sustains SMN enrichment and maintains the mtDNA-KRT15 transcriptomic interaction particularly in late S phase. A. Violin plot of mitochondrial networks per cell in SMN and HMN categories in TF1 and TF10 transformed populations, with median (dashed line) and the quartile ranges (dotted lines) shown. **B.** Ridgeline plots comparing the distribution of the named structural parameters between SMNs and HMNs from TF1 and TF10 groups; Median and Coefficient of Variation are indicated for each parameter, latter in bold. (* signifies Holmes-Bonferroni corrected p-value < 0.05). **C.** Bar chart showing (%SMN / %HMN) per cell among TF1 and TF10 groups. **D.** Violin plot showing (%SMN / %HMN) per cell in TF1 and TF10 groups, with median (dashed line) and the quartile ranges (dotted lines) shown; the percentages of population above 1.1 and below 0.9 are mentioned. **E.** Overall differential gene expression for mtDNA genes using pseudo-bulk RNA-seq analysis (top) and average expression for Prohibitin (PHB) (bottom) for TF1 and TF10 compared to Parental (P) control. **F.** Absolute average expression (top two) and its change in tumor (T) from normal (N) (bottom two) for mtDNA encoded genes and major Keratins for scRNA-seq data of cSCC Patient (P) data (n=10) from Ji. et al., 2020 (67) (N- Normal and T-Tumor). **G.** kME plots of KRT15 transcriptomic interaction modules using hdWGCNA of the TF1 and TF10 datasets compared to P control {original data published in (20)}. **H.** Hub-Gene Network Plot of the TF1: S Late module identified and TF1 / TF10: Cytokine modules identified in **G. I.** Direct transcriptomic connections of KRT15 with mtDNA and HES1 in the cell clusters shown, as outlined in **H**; the table shows edge distance of these direct connections.

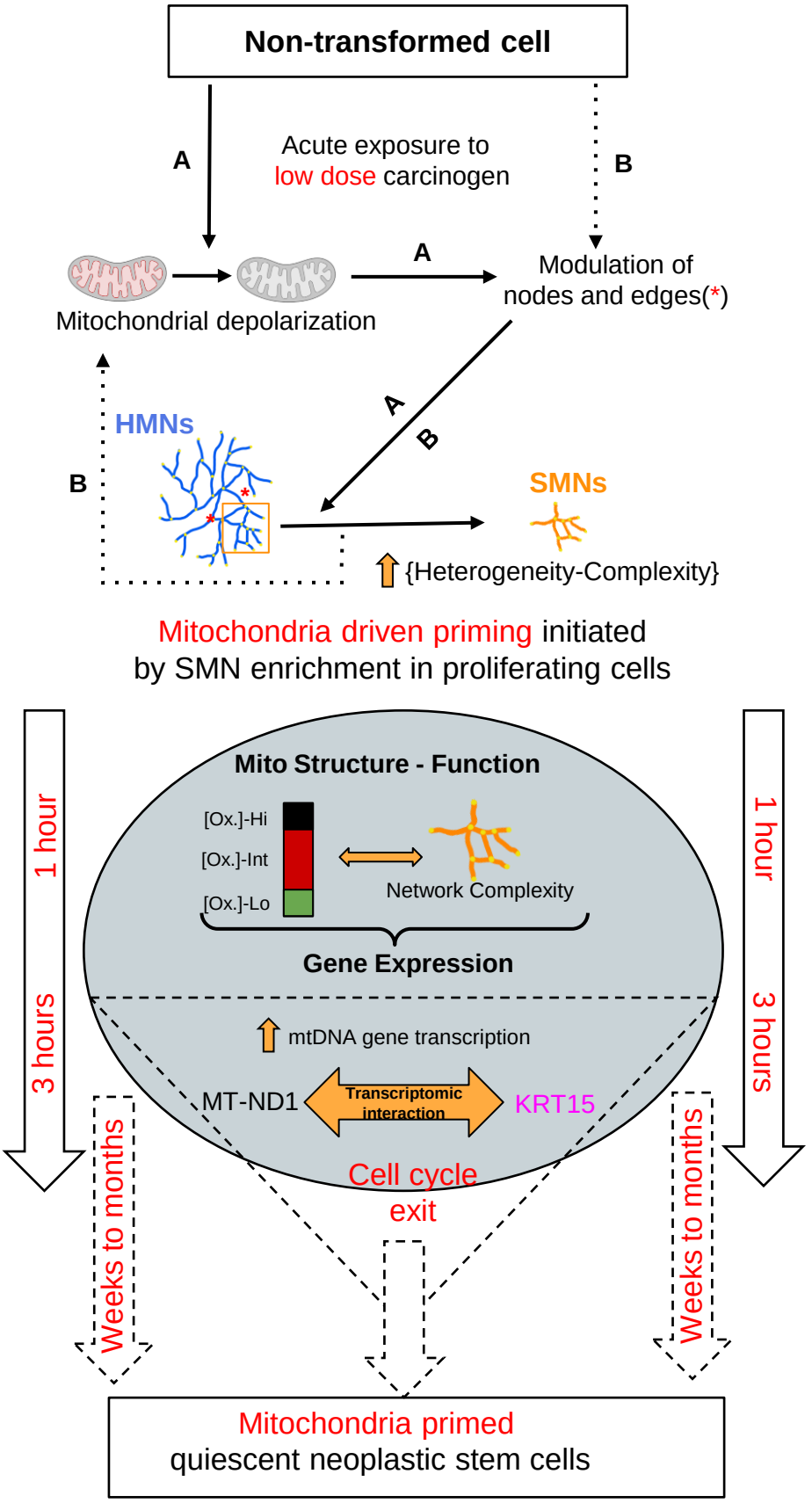
Non-transformed cell
A
Acute exposure to
low dose carcinogen
B
A
Modulation of
nodes and edges(*)
Mitochondrial depolarization
A
B
HMNs
B
SMNs
{Heterogeneity-Complexity}
Mitochondria driven priming initiated
by SMN enrichment in proliferating cells
1 hour
3 hours
Mito Structure - Function
[Ox.]-Hi
[Ox.]-Int
[Ox.]-Lo
Network Complexity
Gene Expression
mtDNA gene transcription
MT-ND1
Transcriptomic interaction
KRT15
Cell cycle
exit
1 hour
3 hours
Weeks to months
Weeks to months
Mitochondria primed
quiescent neoplastic stem cells

Fig. 7

Figure 7. Schematic illustration of the concept of mitochondrial priming of neoplastic transformation following acute exposure to low carcinogenic dose. The model summarizes data from **Fig. 2 to 6.** We propose early enrichment of redox-tuned small mitochondrial physical networks prime neoplasticity by establishing mtDNA-stemness transcriptomic networks prior to cell cycle exit towards maintenance of quiescence neoplastic stem cells. The preferred hypothesis (A) is that acute low-dose carcinogen exposure causes mitochondrial depolarization, which triggers the conversion of HMNs to SMNs by reorganization of the physical nodes and edges of the HMNs. This results in the enrichment of SMNs with greater Network—{Heterogeneity-Complexity} to sustain optimal redox levels towards establishing transcriptomic connection between KRT15 and redox specific mtDNA genes. The alternative hypothesis (B) is that acute low-dose carcinogen exposure reorganizes the mitochondrial network structure to convert HMNs into SMNs, which leads to mitochondrial depolarization.

Supporting Information for

Quantitative analyses of structure-function heterogeneity of individual mitochondrial components reveal an early role of small-mitochondrial-networks in priming neoplastic transformation

Mayank Saini[1#], Swati Agarwala[1#], Biratal Wagle[1], Brian Spurlock[2], Bharti Golchha[1], Danitra Parker[2] and Kasturi Mitra[1,2*]

Email: kasturi.mitra@ashoka.edu.in

This PDF file includes:

Supporting text
Figures S1 - S15 with their legends
SI References

Other supporting materials for this manuscript include the following:

Data S1 - S3

Supplementary Methods

Development of mito-SinComp analysis:

The mito-SinComp analysis uses 3D confocal micrographs with appropriate combinations of compatible probes reporting mitochondrial structure and function separately. The images are required to be amenable for MitoGraph analyses as described before (1, 2). Mito-SinComp analysis requires a Linux or MacOS system to run natively. It can be run on Windows through the Windows Subsystem for Linux (WSL) or another Virtual Machine application like VirtualBox. We developed mito-SinComp analysis using Ubuntu 24.04 LTS with VTK 9.0 modifying the open source code for MitoGraph (https://github.com/vianamp/MitoGraph) and after installing all essential libraries and packages (build-essential, cmake, git, r-base, wget, os, sys, libvtk9-dev, libgl1-mesa-dev, freeglut3-dev, qtbase5-dev, qtdeclarative5-dev, libqt5opengl5-dev, pandas, networkx, igraph, PIL, numpy, tifffile, matplotlib.pyplot). Our customized modular script for mito-SinComp structure-function analyses includes the following steps (**Fig. S9**):

1. Identifying the 'structure' and 'function' channels: Our 3D confocal micrographs for mitochondrial structure (shape) -- function (redox) analyses have 3 channels, excited by 405 nm (function-1), 488 nm (function-2) and 555 nm lasers (structure). MitoGraph exclusively uses only designated structure channel to obtain the binary image through an adaptive thresholding process (3). Therefore, we aimed to obtain the intensity values of the 'function' channels in the pixels of the MitoGraph binary image. Here, we used "splitter.py" function to separate the channels using the AICSImageIO and tifffile libraries. Each channel is then saved as an individual Z-stack in TIFF format as 'structure' and 'function' channels.

2. Running MitoGraph: The open source MitoGraph (v3.0) script is included to obtain the MitoGraph output files as described before (1, 2).

3. Identifying individual mitochondrial components: Mitograph produces the following three outputs containing distinct types of information: a) connected Components ("cc") on interconnected elements; b) mitochondrial elements ("line id") on individual mitochondrial segments; c) points on the mitochondrial skeleton ("point id") on individual data points. Each "point id" belongs to a "line id", and each "line id" belongs to a cc. This information is distributed across the following output files: a) *mitograph.txt* contains information about "point id", "line id", and the length of each "line id"; b) *mitograph.cc* file links "node id" to the "cc" they belong to, c) *mitograph.coo* file provides geometric positions (x, y, z coordinates) for each "node id". To streamline our analysis, we consolidated this data into a single, tidy data frame. To incorporate "cc" information into the *mitograph.txt* file for network-level analysis, we identified which "point id" entries are also "node id" entries, where nodes are the terminating points of a "line id". Towards this, we first computed the Euclidean distance between each pair of "point id" (from *mitograph.txt*) and "node id" (from *mitograph.coo*). Thereafter, we identified the "point id" - "node id" pair with the smallest distance to identify the "point id" that corresponds to each "node id". Once the "nodes" were identified, we used the *mitograph.cc* file to link the cc information to each "node id". This enables us to append "cc" information to the *mitograph.txt* file. Thus, the resulting final data frame integrates "cc", "line id", "point id", x, y, z coordinates and "nodes" in a single *.csv file where the structural and functional properties will be included after having calculated as described below. Thus, a comprehensive data file is created for further downstream analyses.

4. Calculating structural properties for networks and non-networks: We first identified the individual networks and non-networks from the connected components ("cc"), which include both networked and non-networked components. Here, we employed a filtering approach based on the number of edges and nodes. Specifically, any connected component with one edge and two nodes, along with their corresponding data, was classified as a non-networked component. All remaining connected components, along with their corresponding data, were categorized as networked components. This classification enabled the separate analysis of networked and non-networked components, facilitating a more focused examination of their distinct properties. The following table includes the definition and formulae of all the structural parameters studied.

Name of metric	**Definition**	**Formulae**
Length of an individual element in μm -Networks	Length of an individual mitochondrial element within a network	$L\text{-}E_{Net}$
Length of an individual element/edge in μm - Networks (log) [Element Size]	Natural log transformed values of length of an individual mitochondrial element within a network	$\ln(L\text{-}E_{Net})$
Length of an individual mitochondrial component in μm - Network	The total length of individual mitochondrial elements that constitute a networked mitochondrial component.	$L_{Net} = \Sigma L\text{-}E_{Net}$
Length of an individual mitochondrial component in μm - Non-Network	Length of individual mitochondrial elements that constitute a non-networked mitochondrial component.	$L_{nNet} = L\text{-}E_{nNet}$
Length of individual mitochondrial component in μm - Network (log) [Network Size]	The total length of individual mitochondrial elements that constitute a networked mitochondrial component.	$\ln(L_{Net})$
Length of individual mitochondrial component in μm - Non-Network (log) [Non-Network Size]	Length of individual mitochondrial elements that constitute a non-networked mitochondrial component.	$\ln(L_{nNet})$
Number of elements per networked mitochondrial component [# Element / Edges]	Total number of mitochondrial elements/edges that constitute a networked mitochondrial component	$\#E_{Net}$

Name of metric	Definition	Formulae
Total number of mitochondrial components per cell [# Components]	Total number of mitochondrial components that are present in a cell which includes networked and non-networked components	#Comp=#Net+#nNet
Total number of mitochondrial components per cell-Networks [# Networks]	Total number of networked mitochondrial components that are present in a cell.	#Net
Total number of mitochondrial components per cell-Non Networks [# Non-Networks]	Total number of non-networked mitochondrial components that are present in a cell.	#nNet
Total length of mitochondrial components per cell in µm [Sum L_{comp}]	Total length of mitochondrial components that are present in a cell which includes networked and non-networked components	Sum $L_{comp}=\Sigma(L_{Net}+L_{nNet})$
Total length of mitochondrial components per cell in µm -Networks [Sum L_{Net}]	Total length of networked mitochondrial components that are present in a cell.	Sum $L_{Net}=\Sigma L_{Net}$
Total length of mitochondrial components per cell in µm -Non Networks [Sum L_{nNet}]	Total length of non-networked mitochondrial components that are present in a cell.	Sum $L_{nNet}=\Sigma L_{nNet}$
Abundance of mitochondrial components per cell (%)-Networks	It is the percentage of networked mitochondrial components that are present in a cell	(#Net/#Comp) *100
Abundance of mitochondrial components per cell (%)-Non Networks	It is the percentage of non-networked mitochondrial components that are present in a cell	(#nNet/#Comp) *100
Average length of	Total length of all networked mitochondrial	(Sum L_{Net}) / (#Net)

Name of metric	Definition	Formulae
mitochondrial component per cell in µm - Networks	components divided by the number of networked components within a cell	
Average length of mitochondrial component per cell in µm - Non-Networks	Total length of all non-networked mitochondrial components divided by number of non-networked components within a cell	(Sum L_{nNet}) / (#nNet)
Relative length of an individual mitochondrial component within a cell-Networks [CRL mito-Net]	Natural log of the length of a networked mitochondrial component divided by the total length of all the networked components of the cell that the former component is a part of	ln{(L_{Net}) / (Sum L_{Net})}
Relative length of an individual mitochondrial components within a cell-Non networks [CRL mito-nonNet]	Natural log of the length of a non-networked mitochondrial component divided by the total length of all the non-networked components of the cell that the former component is a part of	ln{(L_{nNet}) / (Sum L_{nNet})}
Diameter in µm per networked mitochondrial component [Thickness];	It is calculated assuming each mitochondrial network is a cylinder and derived from using the formulae for volume of a cylinder where radius is half of diameter (D); Vnet is the volume of the network and Lnet is the length of the network. (as obtained from MitoGraph within the mito-SinComp pipeline)	$D = 2\sqrt{\frac{Vnet}{\pi Lnet}}$
[Fission]; [Fusion5]	As previously published (1)	-
Pk of nodes	No. of edges / element arising from a single node. (4, 5)	-
Number of nodes per networked mitochondrial component [# Nodes]	Number of nodes that are present in a networked mitochondrial component excluding free ends.	# Nodes
Number of nodes per length of a networked component [Node Density]	Number of nodes (excluding free ends) divided by the length of the networked component that they belong to	#Nodes/L_{Net}
Number of edges / elements per length of a networked component [Edge Density]	Number of edges / elements divided by the length of the networked component that they belong to	#Elements (#Edges)/L_{Net}

Name of metric	Definition	Formulae
Max Pk of a node times their count per network [Maximum Nodal Connectivity]	It is product of maximum Pk of a node with their count within a networked mitochondrial component	Max Pk * Count
Abundance of SMNs per cell (%)	Number of SMNs divided by total number of networked mitochondrial component within a cell	(#SMNs/#Net) *100
Abundance of HMNs per cell (%)	Number of HMNs divided by total number of networked mitochondrial component within a cell	(#HMNs/#Net) *100
Abundance of mitochondrial components-Networks (%) for [CRL mito-Net]	Percentage of networked components in a certain bin range of their length distribution	(#Net in a bin/ #Net in that population) *100
Abundance of mitochondrial components- Non-Networks (%) for [CRL mito-nonNet]	Percentage of non-networked components in a certain bin range of their length distribution	(#nNet in a bin/ #nNnet in that population) *100

5. Calculating function for networks and non-networks: The redox function was calculated by obtaining the average pixel intensity ratio of individual cc by mapping the 'function' information to the 'structure' information obtained as above. This was achieved following the steps below:

a. Converting MitoGraph output to pixel coordinates: MitoGraph was run using Z-stack for the structure channel using *runMitograph.py* function in a batch processing mode for all cells within a single directory. Mitograph outputs the geometric coordinates (x, y, z) of the mitochondrial skeleton as per the provided scale when running Mitograph. The pixel coordinates (x_pixel, y_pixel, z_pixel) can be retrieved from the geometric coordinates through using the scale using the formula, Where *D* represents either x, y or z. This is then rounded to the nearest integer, as pixel coordinates are a discrete quantity.

$$D_{pixel} = \frac{D}{D_{scale}}$$

The table below shows an example of the results of this process, where the scale for *x* and *y* is 0.104 and is 0.5 for z.

line_id	point_id	x	y	z	x_pixel	y_pixel	z_pixel
0	0	8.97867	4.85333	2.33333	86	47	5
0	1	8.85002	4.95192	2.41975	85	48	5
0	2	8.73600	4.99200	2.50000	84	48	5
1	0	17.42000	6.05800	2.37500	168	58	5
1	1	17.27913	5.89616	2.43519	166	57	5

The conversion is confirmed by the overall overlap of the calculated pixel coordinates (in red) with the MIP of the structural channel, as exemplified in the image below.

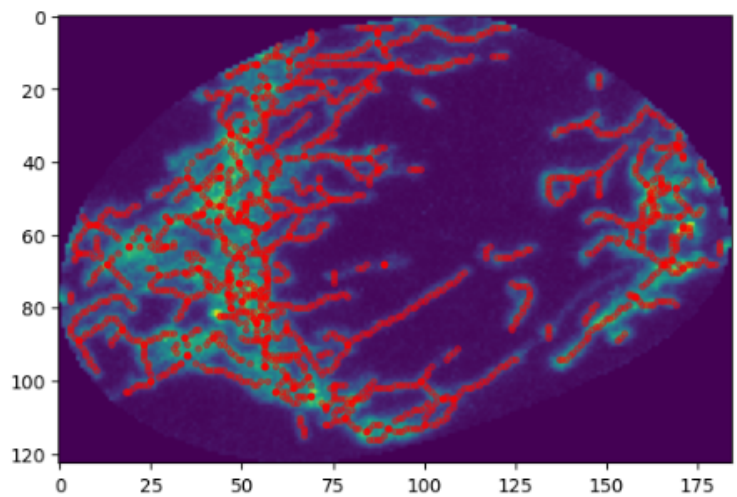

b.<u>Obtaining the intensity values of the pixel coordinates from individual 'function' channels:</u> The Z-stacks Tiff images are converted into a three dimensional array using tifffile library. The intensity value of each pixel coordinate generated in step 5 is calculated from the individual functional channels. The average intensity of the 9 pixels in a 1X3X3 voxel is calculated and assigned to the central pixel. This is repeated for every x, y, z pixel calculated in step 5. In the following example, in the slice of an image at z = 2, , intensity of a_{222} is the average of all the colored pixels.

$$z = 2, \begin{pmatrix} b_{11} & b_{12} & b_{13} & b_{14} & b_{15} \\ b_{21} & a_{211} & a_{212} & a_{213} & b_{25} \\ b_{31} & a_{221} & a_{222} & a_{223} & b_{35} \\ b_{41} & a_{231} & a_{232} & a_{233} & b_{45} \\ b_{51} & b_{52} & b_{53} & b_{54} & b_{55} \end{pmatrix}$$

$$Pixel\ intensity\ of\ a_{222} = \frac{a_{211} + a_{212} + a_{213} + a_{221} + a_{222} + a_{223} + a_{231} + a_{232} + a_{333}}{9}$$

c. <u>Obtaining pixel intensity ratio to reflect redox function</u>**:** Once the pixel_intensity for each pixel is obtained (step 6), this information is put into the "pixel_intensity_channel_*N*" column, where "*N*" reflects which, channel was selected. For calculating the pixel intensity ratio at the individual cc level, the intensities for each channel are grouped according to their "cc_id" and averaged to find the pixel intensity of the "cc". These values are validated as described in the main text. The ratio of these averages gives the "cc_pixel_intensity_ratio", as exemplified below for an individual "cc".

x_pixel	y_pixel	z_pixel	pixel_intensity_channel_1	pixel_intensity_channel_2
105	55	17	256.5	12.75
106	54	17	243.5	35
107	54	18	374	18
108	54	18	483.5	34.25
109	55	18	463.5	17
110	56	18	342.75	0

cc_pixel_intensity_ratio
0.05407279
0.05407279
0.05407279
0.05407279
0.05407279
0.05407279

$$cc\ pixel\ intensity\ channel\ 1 = \frac{256.5 + 243.5 + 374 + 483.5 + 463.5 + 342.75}{6}$$

$$cc\ pixel\ intensity\ channel\ 2 = \frac{12.75 + 35 + 18 + 34.25 + 17 + 0}{6}$$

$$cc\_pixel\_intensity\_ratio = \frac{19.5}{360.625} = 0.05407$$

d. Visualizing single networks and non-networks within single cells in 3D graphs: Visualization of the data from the comprehensive data file is performed using the *3D_generate_graphs.py* script. The data is plotted by looping through each "**cc**" and each "**line id**". The individual points in each "**line id**" are then plotted to ensure that the order of the points is preserved in the visualization. To distinguish between shapes, each "**cc**" is assigned a random and unique color. These shapes are then rendered in a 3D space. The same process is repeated for generating the LUT of the 'function'values, where the color code represents redox function of individual element.

High Dimensional weighted gene correlation network analyses (hdWGCNA) :

hdWGCNA (6), smorabit.github.io/hdWGCNA/) was used to identify gene interaction modules amongst differentially expressed genes (> 0.25 avg_logFC, $<10^{-5}$ p_val_adj, pct ≥ 0.25 in pseudobulk analyses using FindMarkers function) and amongst the characteristic marker genes for the identified cell clusters (> 0.25 avg_logFC, $<10^{-5}$ p_val_adj). QC plots of nCounts_RNA distributions were used to establish lower thresholds for outlier removal (**Figs. S11A-B, S12A, S13A, S14A, S15A**). This processed integrated Seurat object is used as an input for respective hdWGCNA, both at the pseudobulk and cell cluster levels.

The hdWGCNA object was initialized, and metacells were constructed using K-nearest neighbors (KNN) (**Figs. S11C-D, S12B-C, S13B-C, S14B-C, S15B-C**). Gene expression matrices were constructed, and pairwise Pearson's correlations were computed, transformed into adjacency matrices using a soft-thresholding power approach (**Figs. S11E, S12D, S13D, S14D, S15D**), and used to construct networks using Topological Overlap Measures (TOM) values The hdWGCNA algorithm ensured a scale-free topology during signed network construction for each hdWGCNA object for both pseudobulk and cell cluster. Transcriptomic modules were detected using hierarchical clustering and TOM, with module eigengenes (MEs) computed for further analysis. Module connectivity (kME) values were calculated to identify hub genes characterized by high kME values. Selection of specific parameter cut-offs for hdWGCNA are elaborated below:

a. K-nearest neighbors (KNN)-based dimensionality reduction: Metacells for each experimental/control group (pseudobulk) and specific clusters were constructed using KNN, leveraging biological similarity to define cellular subpopulations in each hdWGCNA object. Pearson correlation-based density plots guided the selection of K value of 20 with a maximum of 10 shared neighbors for an average of 5000 cells in each population, optimizing the balance between capturing local structure and minimizing noise in sparse data (**Figs. S11C-D, S12B-C, S13B-C, S14B-C, S15B-C**).

b. Soft Thresholding Power (β): The optimal β value was selected by evaluating the scale-free topology fit index, to enhance strong correlations and reduce weaker ones, aiming for the lowest power where the network closely approximated a scale-free structure. The β values between 6 and 10 were determined as optimal, balancing network sparsity with scale-free topology at both pseudobulk and cell cluster based hdWGCNA objects (solid black circles on plots in (**Figs. S11E, S12D, S13D, S14D, S15D**). This transformation enabled robust, biologically meaningful signed networks across cellular subpopulations

c. Module Connectivity (kME): kME measures the correlation between a gene's expression profile and its module eigengene, indicating the gene's alignment with the module's expression pattern. High kME values suggest that a gene has a central role within the module, while low values indicate a less integral role. Genes in each module were ranked by kME, identifying the top 20 in pseudobulk (**Fig. 1G, 4E**) and top 25 (**Fig. 5D**) in cell cluster-based hdWGCNA for functional significance. This kME analysis highlighted closely interacting clusters, enabling us to identify top ranking hub genes within a network. with high connectivity of KRT15, its interactors, and mtDNA genes within the biological network of connectivity and interaction strength within the biological network (**Fig. 5E**).

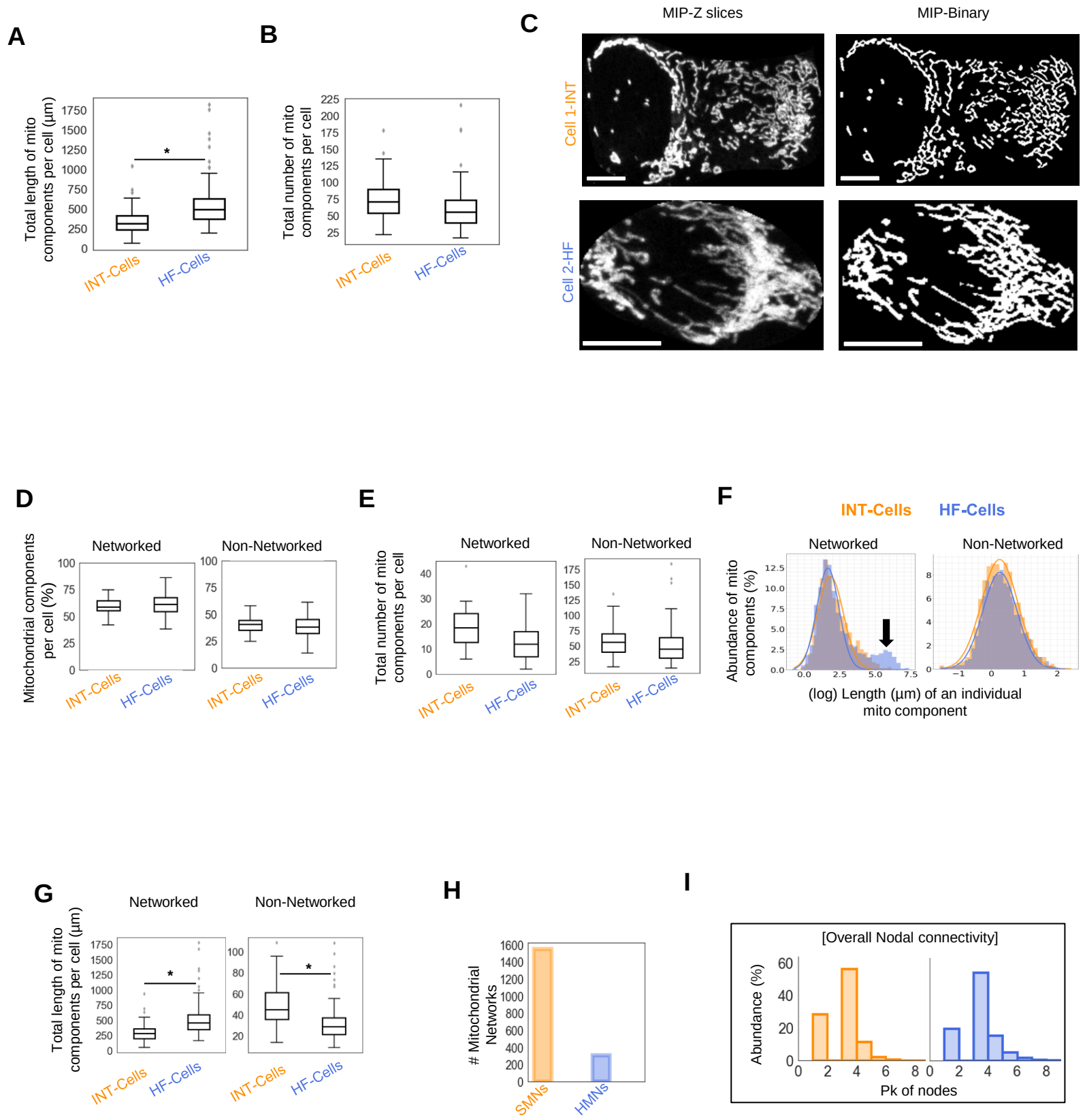
A
Total length of mito components per cell (µm)
1750
1500
1250
1000
750
500
250
0
*
INT-Cells
HF-Cells
B
Total number of mito components per cell
225
200
175
150
125
100
75
50
25
INT-Cells
HF-Cells
C
MIP-Z slices
MIP-Binary
Cell 1-INT
Cell 2-HF
D
Mitochondrial components per cell (%)
Networked
Non-Networked
100
75
50
25
0
INT-Cells
HF-Cells
E
Total number of mito components per cell
Networked
Non-Networked
40
30
20
10
0
175
150
125
100
75
50
25
INT-Cells
HF-Cells
F
INT-Cells
HF-Cells
Networked
Non-Networked
Abundance of mito components (%)
12.5
10.0
7.5
5.0
2.5
0.0
0.0
2.5
5.0
7.5
8
6
4
2
0
−1
0
1
2
(log) Length (µm) of an individual mito component
G
Total length of mito components per cell (µm)
Networked
Non-Networked
1750
1500
1250
1000
750
500
250
0
*
100
80
60
40
20
*
INT-Cells
HF-Cells
H
Mitochondrial Networks
1600
1400
1200
1000
800
600
400
200
0
SMNs
HMNs
I
[Overall Nodal connectivity]
Abundance (%)
60
40
20
0
0
2
4
6
8
0
2
4
6
8
Pk of nodes

Fig. S1

Figure S1. Development of mitoSinComp structural analyses. A. Box plot of the total length of mitochondrial components (including networks and non-networks) per cell in INT and HF groups. **B.** Box plot of the total number of mitochondrial components (including networks and non-networks) per cell in INT and HF groups. **C.** Representative maximum intensity projection (MIP) of original Z slices and Binary from mitoGraph code used in mito-SinComp analysis described in **Fig-1B**; Scale bar: 5 µm. **D.** Box plot of mitochondrial components per cell in networked and non-networked categories in INT-cells and HF-cells groups. **E.** Box plot of the total number of mitochondrial components per cell in networked and non-networked categories in INT-cells and HF-cells groups. **F.** Histogram distribution of log-transformed lengths of individual mitochondrial components in networked and non-networked categories (ignoring their cell identity) in INT-cells and HF-cells groups. **G.** Box plot of the total length of mitochondrial components per cell in networked and non-networked categories in INT-cell and HF-cell groups. **H.** Bar chart showing the number of mitochondrial networks in SMNs and HMNs categories in INT-cell and HF-cell groups. **I.** Histogram plots representing overall nodal connectivity (* signifies Holmes-Bonferroni corrected p-value < 0.05).

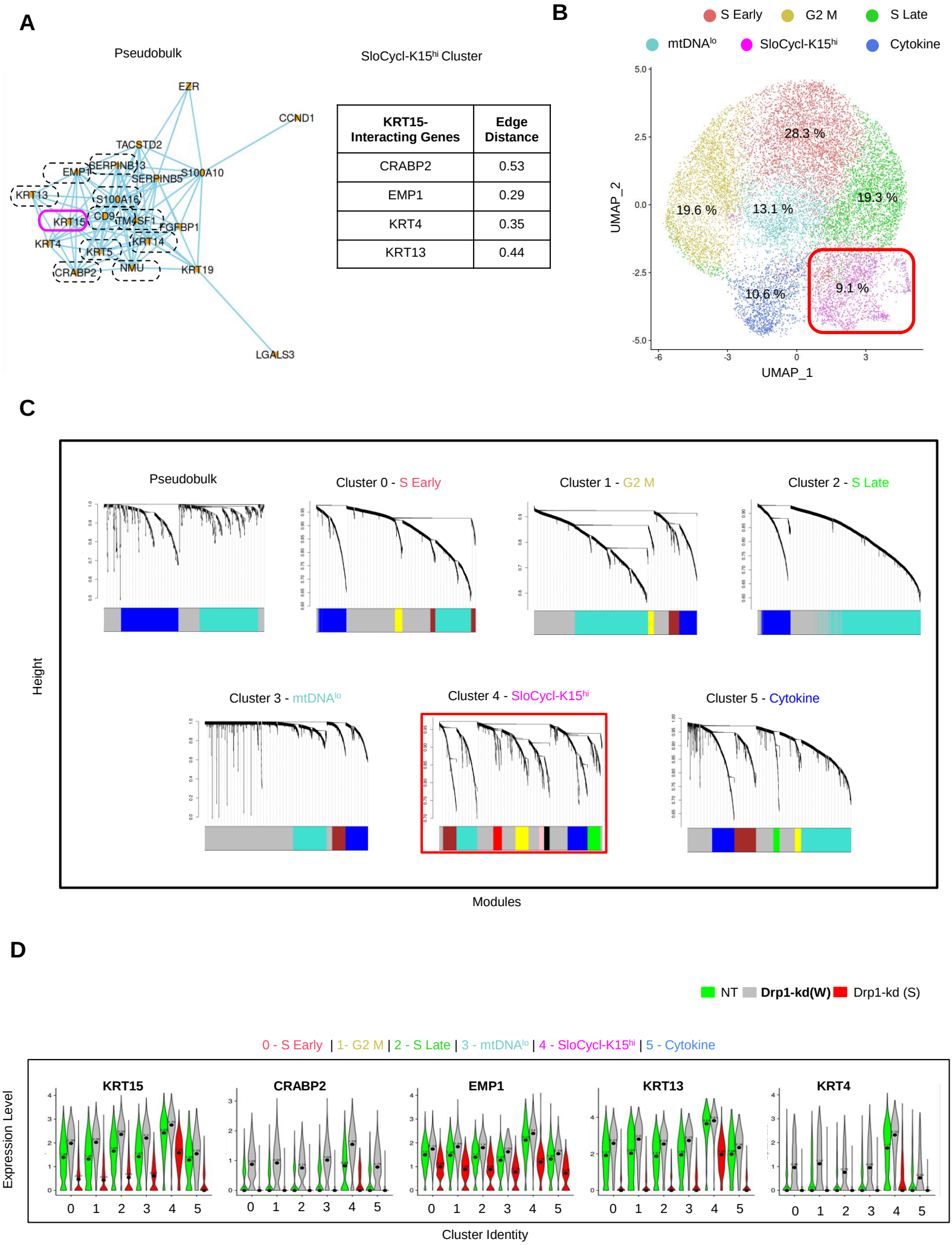

KRT15-Interacting Genes	Edge Distance
CRABP2	0.53
EMP1	0.29
KRT4	0.35
KRT13	0.44

Fig. S2

Figure S2. Employment of hdWGCNA to identify stemness transcriptomic network. A. Hub-Gene Network plot for the module from the pseudobulk analyses identifying the KRT15 module in the left panel of **Fig.1G**. Direct KRT15 transcriptomic connections are outlined with dashed lines, with KRT15 outlined in purple (left). The table depicts the edge distance of the direct transcriptomic connections of KRT15 in the module identified in the SloCycl-K15^{hi} cluster in right panel of **Fig. 1G**. **B.** UMAP plot depicting the color-coded scRNA-seq derived clusters (0-5) with the pooled data of DRP1-kd (W), DRP1-kd (S) and NT (control) populations, with the SloCycl-K15^{hi} cluster outlined; numbers denote percentages of cells within each cluster derived from the pie chart for the clusters (not shown). **C.** Dendrograms depicting hierarchical clustering of adjacency-based dissimilarity to identify color-coded co-expression modules, where grey module represents genes with no significant co-expression; dendrograms from both pseudobulk and cell cluster based analyses shown. **D.** Violin plots depicting gene expression of KRT15 and its direct transcriptomic connections across scRNA-seq derived clusters in the DRP1-kd (W), DRP1-kd (S) and NT (control) populations.

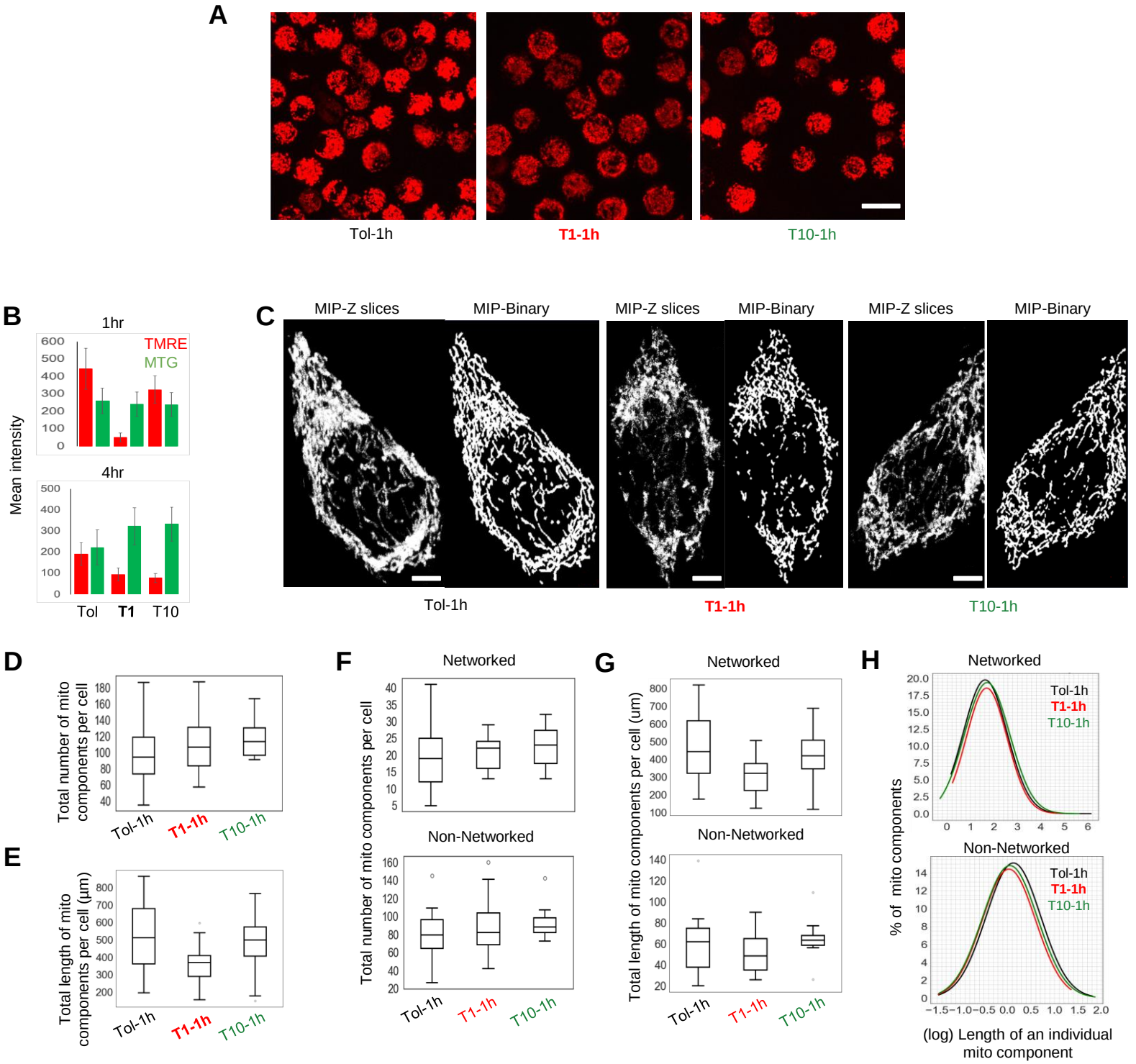
A
Tol-1h
T1-1h
T10-1h
B
1hr
TMRE
MTG
4hr
Mean intensity
Tol
T1
T10
C
MIP-Z slices
MIP-Binary
Tol-1h
T1-1h
T10-1h
D
Total number of mito components per cell
E
Total length of mito components per cell (µm)
F
Networked
Non-Networked
Total number of mito components per cell
G
Total length of mito components per cell (um)
H
% of mito components
(log) Length of an individual mito component

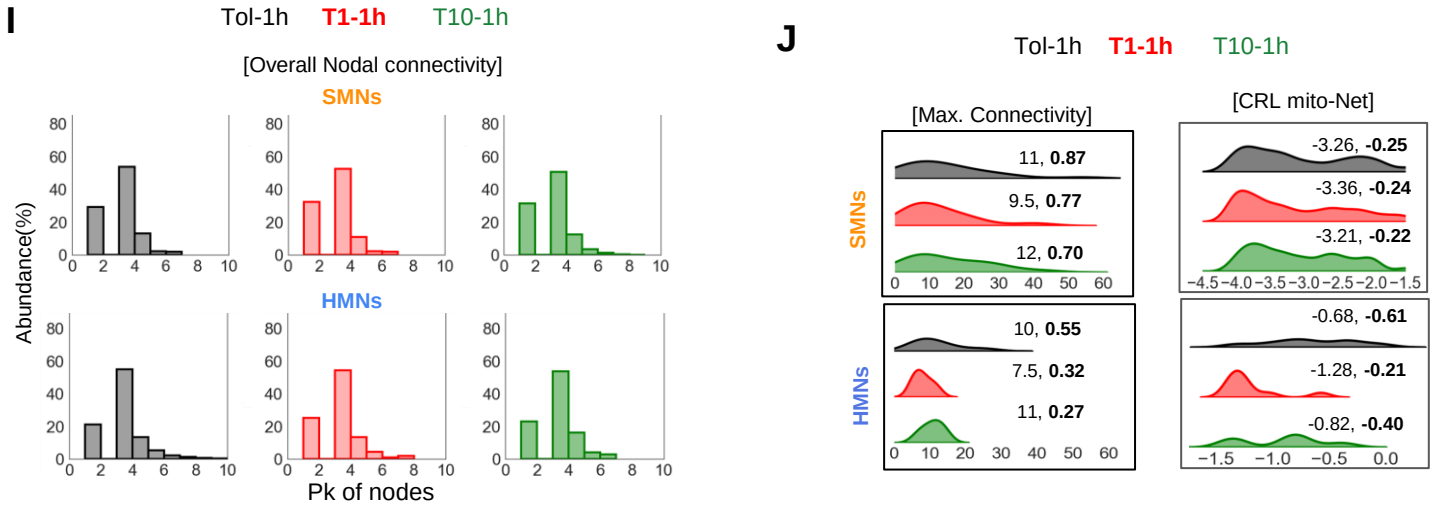
I
Tol-1h
T1-1h
T10-1h
[Overall Nodal connectivity]
SMNs
HMNs
Abundance(%)
Pk of nodes
J
[Max. Connectivity]
[CRL mito-Net]
SMNs
HMNs
11, 0.87
9.5, 0.77
12, 0.70
10, 0.55
7.5, 0.32
11, 0.27
-3.26, -0.25
-3.36, -0.24
-3.21, -0.22
-0.68, -0.61
-1.28, -0.21
-0.82, -0.40

Fig. S3

Figure. S3. Studying the impact of T1-1h and T10-1h exposure on mitochondrial potential and mitochondrial structural properties employing mito-SinComp structural analyses. A. Maximum Intensity Projections of Z-slices of TMRE-stained HaCaT cells after Tol-1h, T1-1h, T10-1h treatment. Scale bar: 20 µm. **B.** Bar chart showing the mean fluorescent intensity of MTG and TMRE from individual HaCaT cells from confocal micrographs of Tol-1h, T1-1h, T10-1h (top) and Tol-4h, T1-4h and T10-4h (bottom) groups. **C.** Representative maximum intensity projection (MIP) of original Z slices and Binary from mitoGraph code used in mtio-SinComp analysis described in **Fig. 2**; Scale bar: 5 µm. **D.** Box plot of the total number of mitochondrial components (including networks and non-networks) per cell in Tol-1h, T1-1h and T10-1h groups. **E.** Box plot of the total length of mitochondrial components (including networks and non-networks) per cell in Tol-1h, T1-1h and T10-1h groups **F.** Box plot of the total number of mitochondrial components per cell in networked and non-networked categories in Tol-1h, T1-1h and T10-1h groups. **G.** Box plot of the total length of mitochondrial components per cell in networked and non-networked categories in Tol-1h, T1-1h and T10-1h groups. **H.** Histogram distribution of log-transformed raw lengths of individual mitochondrial components in networked and non-networked category in Tol-1h, T1-1h and T10-1h groups. **I.** Histogram showing overall nodal connectivity of SMNs and HMNs in Tol-1h, T1-1h and T10-1h groups. **J.** Ridgeline plot comparing the distribution of structural parameters between SMNs and HMNs from Tol-1h, T1-1hand T10-1h groups; Median and Coefficient of Variation are indicated for each parameter, latter in bold. (* signifies Holmes-Bonferroni corrected p-value < 0.05)

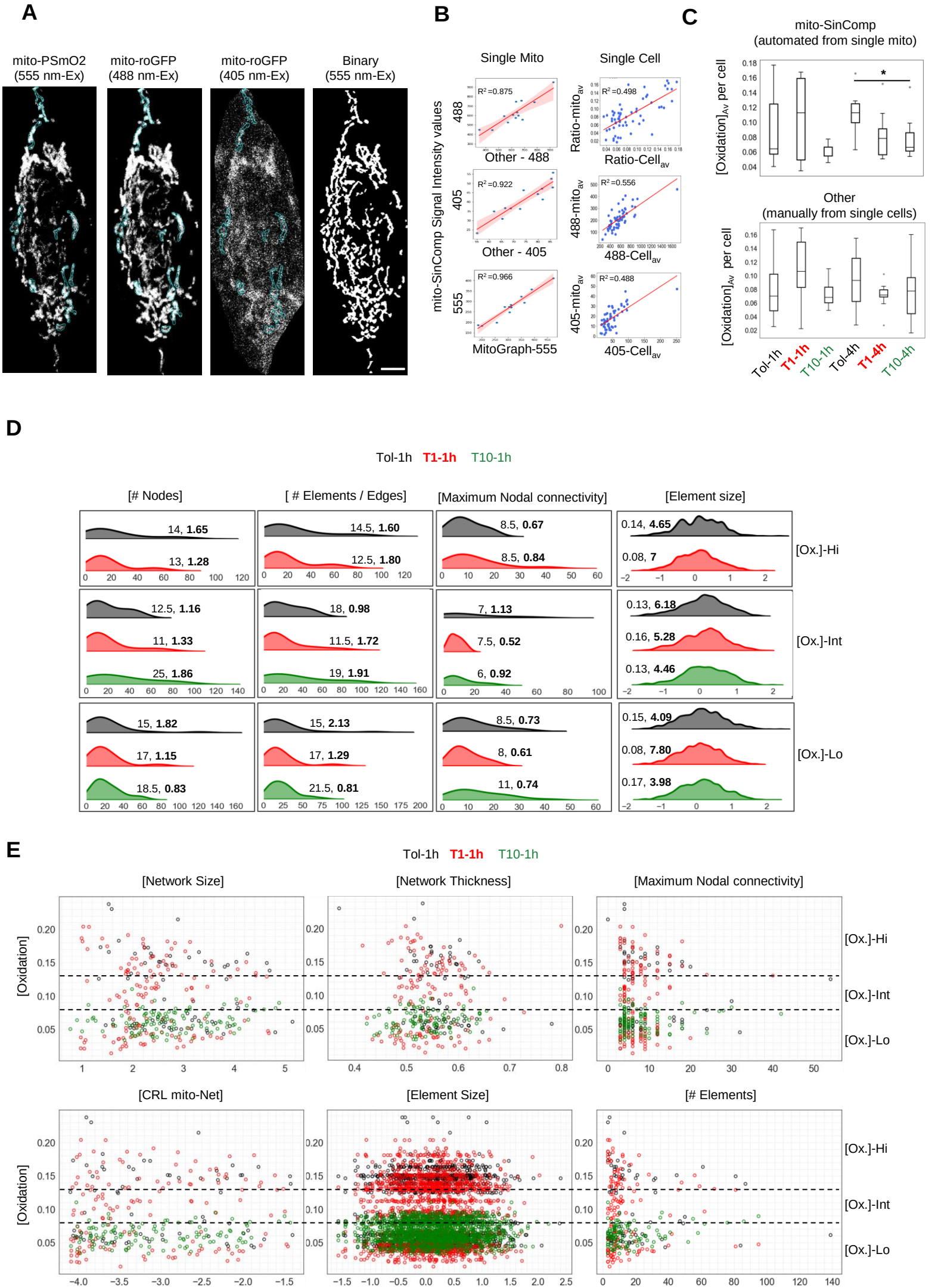
A
mito-PSmO2 (555 nm-Ex)
mito-roGFP (488 nm-Ex)
mito-roGFP (405 nm-Ex)
Binary (555 nm-Ex)
B
Single Mito
Single Cell
mito-SinComp Signal Intensity values
488
Other - 488
405
Other - 405
555
MitoGraph-555
Ratio-mito$_{av}$
Ratio-Cell$_{av}$
488-mito$_{av}$
488-Cell$_{av}$
405-mito$_{av}$
405-Cell$_{av}$
C
mito-SinComp (automated from single mito)
Other (manually from single cells)
[Oxidation]$_{Av}$ per cell
Tol-1h
T1-1h
T10-1h
Tol-4h
T1-4h
T10-4h
D
Tol-1h T1-1h T10-1h
[# Nodes]
[# Elements / Edges]
[Maximum Nodal connectivity]
[Element size]
[Ox.]-Hi
[Ox.]-Int
[Ox.]-Lo
E
Tol-1h T1-1h T10-1h
[Network Size]
[Network Thickness]
[Maximum Nodal connectivity]
[CRL mito-Net]
[Element Size]
[# Elements]
[Oxidation]

Fig. S4

Figure. S4. Studying the impact of T1-1h and T10-1h exposure on mitochondria employing mito-SinComp structure-function analyses. A. Representative Maximum Intensity Projection (MIP) of single cell from the mtio-SinComp structure-function analysis described in **Fig. 3**; shown are the channels corresponding to the mitochondrial structure (mito-PsMO2) or function (mito-roGFP) probes and the MitoGraph binary image. Scale bar: 5 µm. **B.** Bivariate plot of signal intensity values obtained using mito-SinComp structure-function script and that from ImageJ. Values are for 13 individual mitochondrial component (network or non-network) outlined in the representative cell in **A** (Left); Similar comparison shown for averaged values at the single-cell level (Right). **C.** Box plot of the $[\text{Oxidation}]_{Av}$ per cell, as calculated using the automated mito-SinComp script (top) and manually from single cells using image analysis software (bottom). **D.** Ridgeline plot comparing the distribution of structural parameters of SMNs between three zones of oxidation from Tol-1h, T1-1h and T10-1h groups; Median and Coefficient of Variation are indicated for each parameter, the latter in bold. **E.** Scatter plot of [Oxidation] vs various structure parameters for individual SMNs in Tol-1h, T1-1h and T10-1h groups; the dashed line indicates bifurcation into three [Oxidation] zones as described in the appropriate Results section.

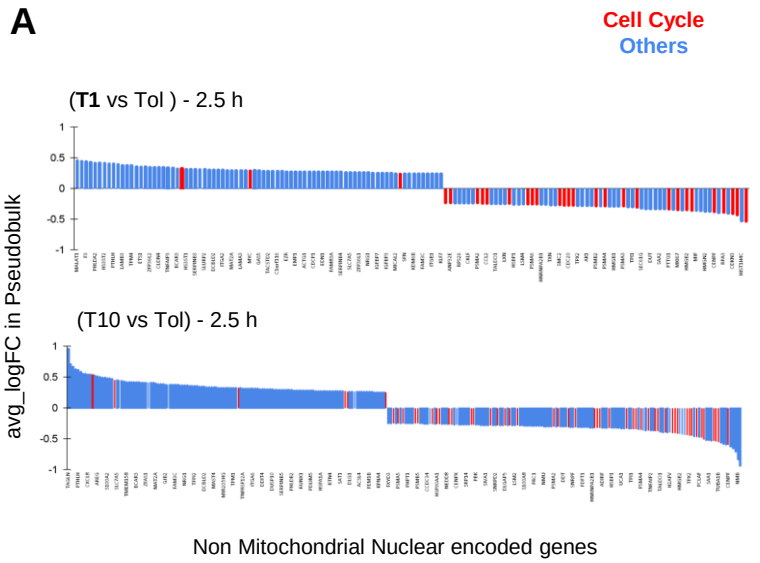

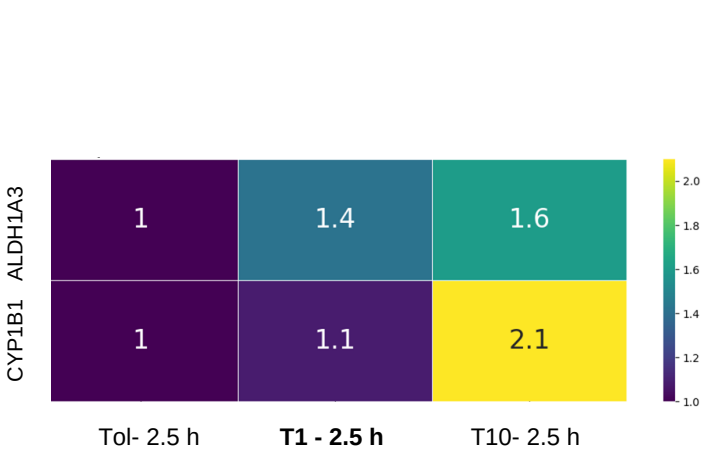

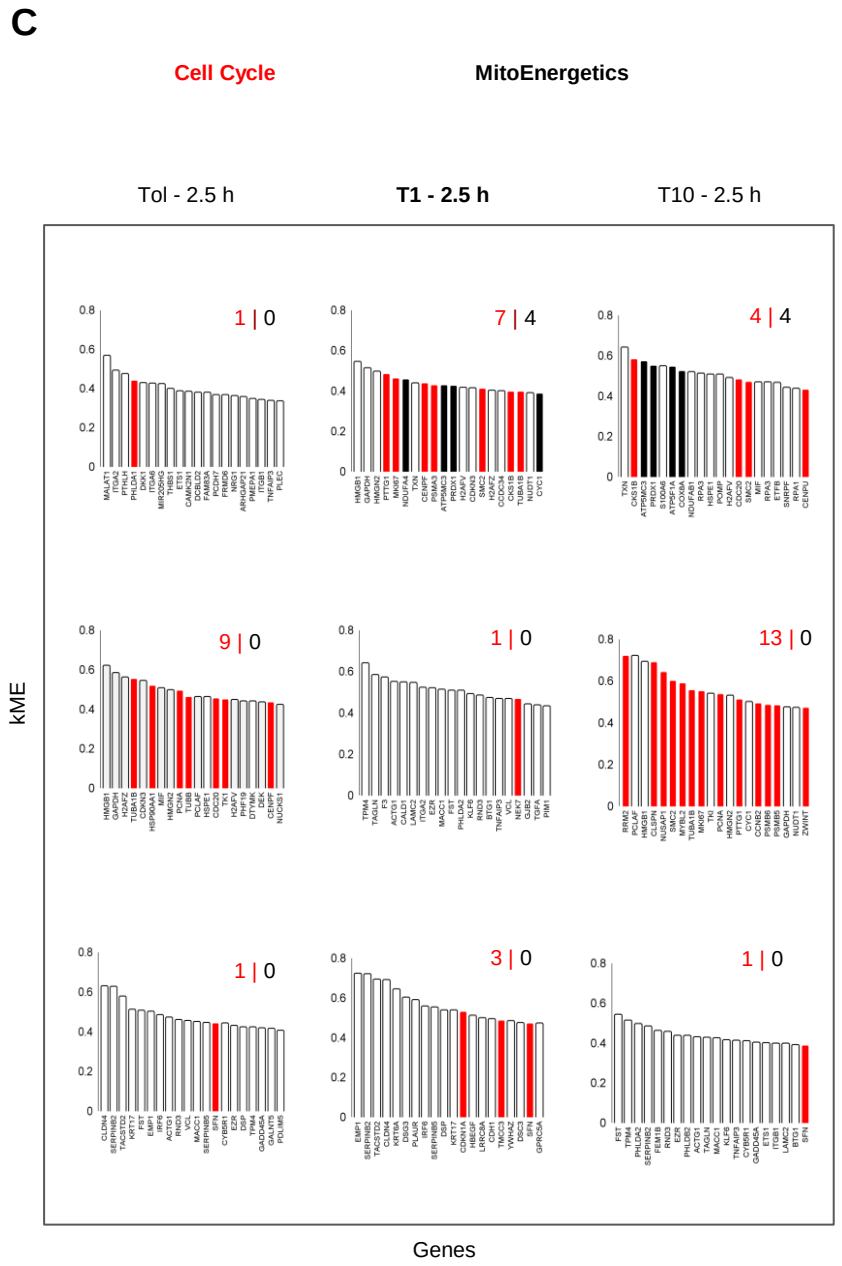

D

Genes	Direct Connections #
GAPDH	16
PSMA3	12
CDC20	7
MKI67	5
CYC1	5
CENPF	4
HMGB1	3
PTTG1	3
NDUFA4	3
CCDC34	3
ATP5MC3	3
H2AFV	3
COX8A	3
COX5B	3
CDKN3	2
HSPE1	2
HNRNPA2B1	2
PRDX1	1
CCNB2	1
H2AFZ	1

Fig. S5

Figure S5. Studying the impact of T1-2.5h and T10-2.5h exposure using hdWGCNA on pseudo-bulk pairwise analyses. A. Bar plots showing the modulation of expression of non-mitochondrial nuclear encoded genes Pairwise pseudo-bulk analyses T1-2.5h vs Tol-2.5h and T10-2.5h vs Tol-2.5h using Seurat's 'FindMarkers' (FM) function on scRNA-seq data; only are shown here. **B.** Heat map showing average gene expression of CYP1B1 and ALDHA3 induced by TCDD. Color intensity represents average expression values, with a scale from 1 (low) to 2 (high). Warmer colors indicate higher expression levels. **C.** Corresponding kME plots of modules using hdWGCNA modules, for pairwise pseudobulk analyses of T10-2.5h with respect to Tol-2.5h. Mitochondrial energetics genes are labelled in black, and cell cycle genes are labelled in red **D.** Tabulation of Degree Connectivity (in terms of direct connections) for the top20 genes identified in the hdWGCNA-derived modules as in **C**. GAPDH shows the maximum connectivity with cell cycle and mitochondrial genes on either side of the network as shown in **Fig. 4F**.

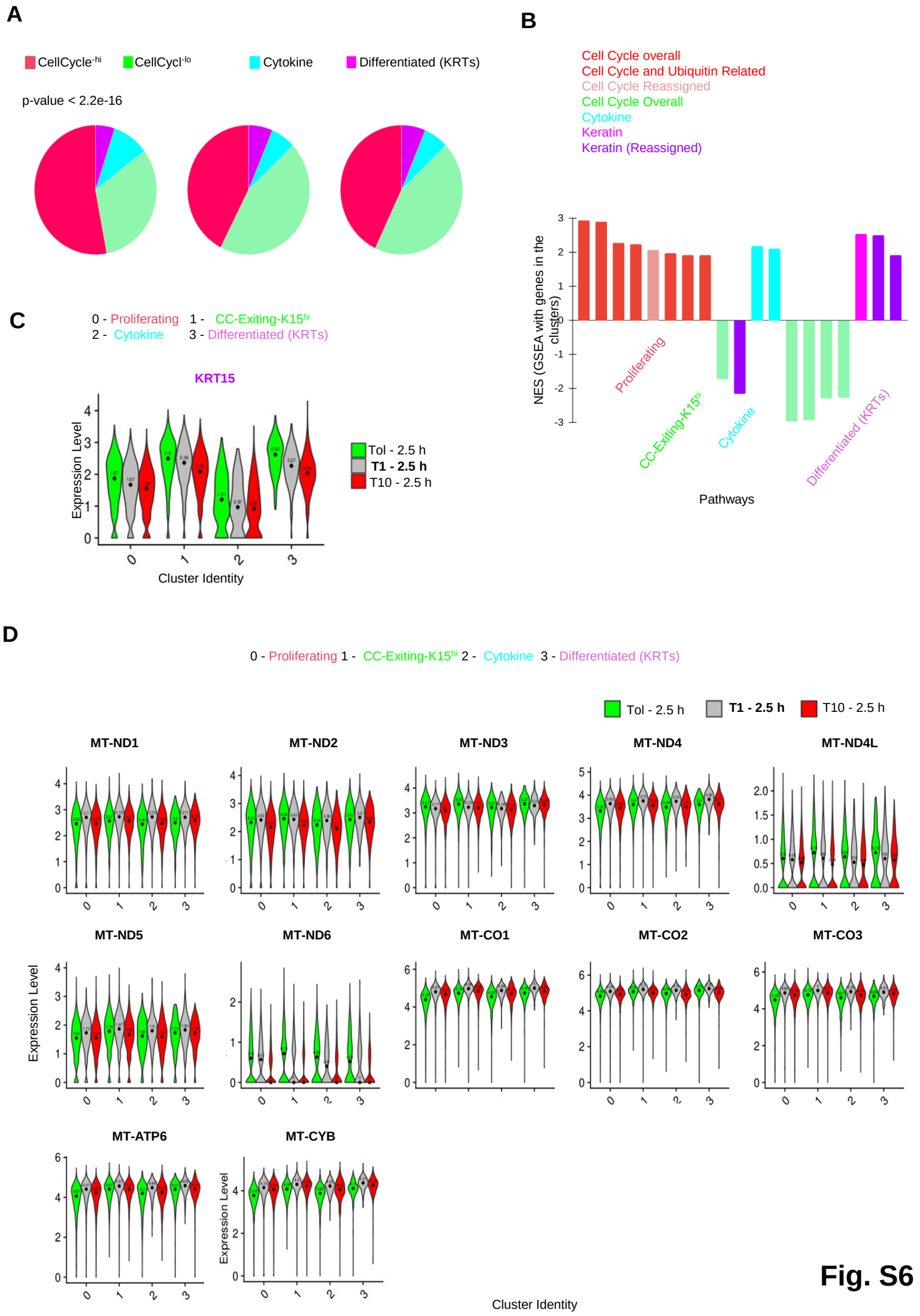
A
CellCycle-hi
CellCycl-lo
Cytokine
Differentiated (KRTs)
p-value < 2.2e-16
B
Cell Cycle overall
Cell Cycle and Ubiquitin Related
Cell Cycle Reassigned
Cell Cycle Overall
Cytokine
Keratin
Keratin (Reassigned)
NES (GSEA with genes in the clusters)
Proliferating
CC-Exiting-K15hi
Cytokine
Differentiated (KRTs)
Pathways
C
0 - Proliferating
1 - CC-Exiting-K15hi
2 - Cytokine
3 - Differentiated (KRTs)
KRT15
Expression Level
Cluster Identity
Tol - 2.5 h
T1 - 2.5 h
T10 - 2.5 h
D
0 - Proliferating 1 - CC-Exiting-K15hi 2 - Cytokine 3 - Differentiated (KRTs)
Tol - 2.5 h
T1 - 2.5 h
T10 - 2.5 h
MT-ND1
MT-ND2
MT-ND3
MT-ND4
MT-ND4L
MT-ND5
MT-ND6
MT-CO1
MT-CO2
MT-CO3
MT-ATP6
MT-CYB
Expression Level
Cluster Identity

Fig. S6

Figure S6. Studying the impact of T1-2.5h and T10-2.5h exposure on scRNA-seq derived clusters. A. Piechart displaying the percentage distribution of scRNA-seq derived cell clusters in Tol-2.5h, T1-2.5h and T10-2.5h cell populations. Chi-square test p-values are indicated. B. Normalized enrichment scores (NES) of functional pathways identified by GSEA for marker genes of Clusters 0-3. Functional annotations based on leading-edge genes are listed on top, with color-coded clusters arranged as in **Fig. 5A. C.** Violin plots showing expression levels of the stem cell gene KRT15 in Tol-2.5h, T1-2.5h and T10-2.5h cell populations across scRNA-seq derived cell clusters (0-3). **D.** Violin plots showing the expression of mtDNA genes in Tol-2.5h, T1-2.5h and T10-2.5h cell populations across scRNA-seq derived cell clusters (0-3).

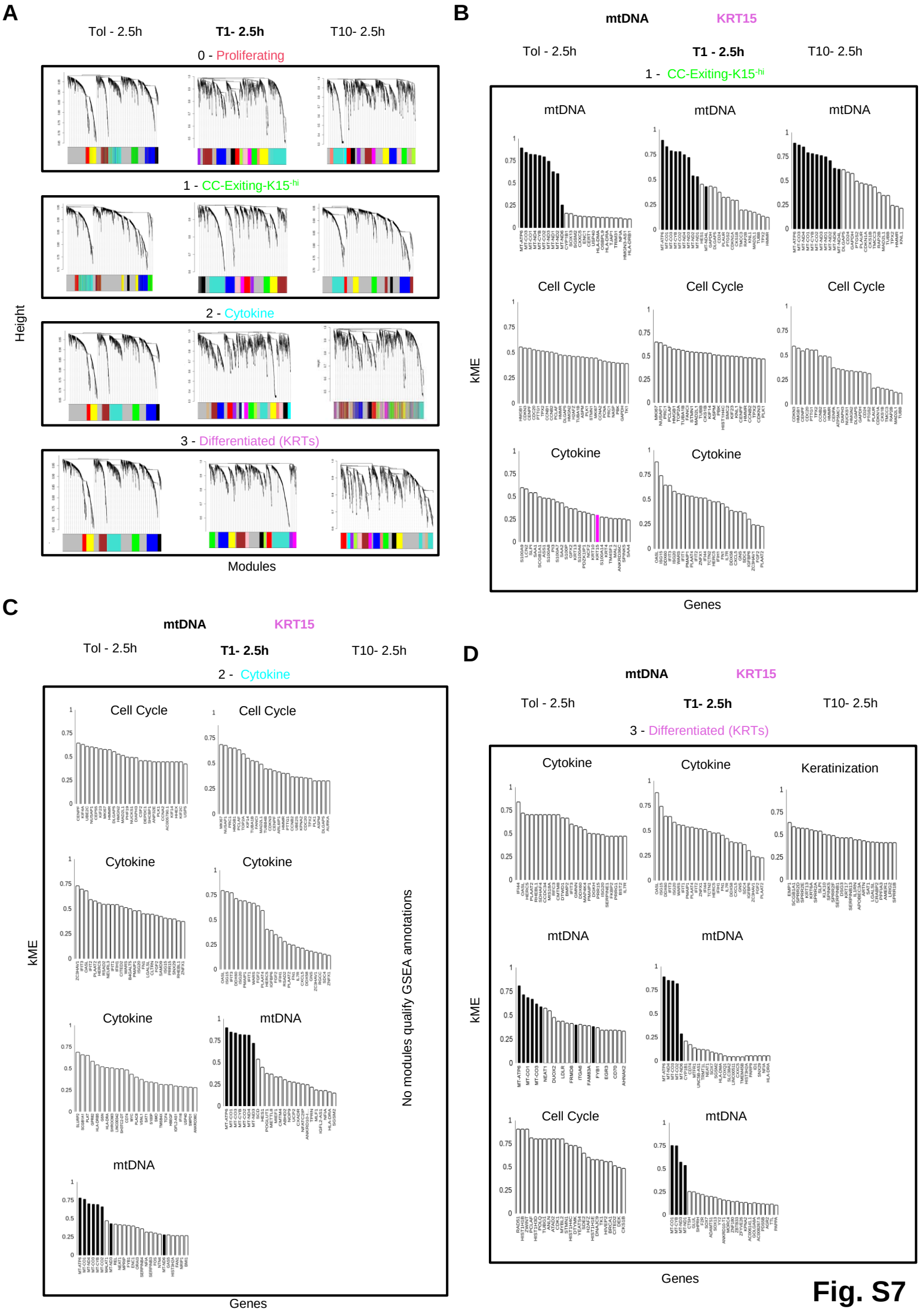
A
Tol - 2.5h
T1- 2.5h
T10- 2.5h
0 - Proliferating
1 - CC-Exiting-K15-hi
2 - Cytokine
3 - Differentiated (KRTs)
Height
Modules
B
mtDNA
KRT15
Tol - 2.5h
T1 - 2.5h
T10- 2.5h
1 - CC-Exiting-K15-hi
mtDNA
Cell Cycle
Cytokine
kME
Genes
C
mtDNA
KRT15
Tol - 2.5h
T1- 2.5h
T10- 2.5h
2 - Cytokine
Cell Cycle
Cytokine
mtDNA
kME
Genes
No modules qualify GSEA annotations
D
mtDNA
KRT15
Tol - 2.5h
T1- 2.5h
T10- 2.5h
3 - Differentiated (KRTs)
Cytokine
Keratinization
mtDNA
Cell Cycle
kME
Genes

Fig. S7

Figure S7. Studying the impact of T1-2.5h and T10-2.5h exposure on gene co-expression modules using hdWGCNA on single cell clusters. A. Dendrograms generated through hierarchical clustering of adjacency-based dissimilarity to identify distinct co-expression color coded modules (grey denotes no significant coexpression) for Tol-2.5h, T1-2.5h and T10-2.5h hdWGCNA objects across scRNA-seq derived cell clusters. **B.** kME Plots from hdWGCNA, for non mtDNA-KRT15 interacting modules of scRNASeq derived CC-Exiting-K15^{hi} cell cluster for Tol-2.5h, T1-2.5h and T10-2.5h cell population. **C.** Plot similar to **Fig. S7B** for Cytokine cluster. **D.** Plot similar to **Fig. S7B** for Differentiated (KRTs) cluster.

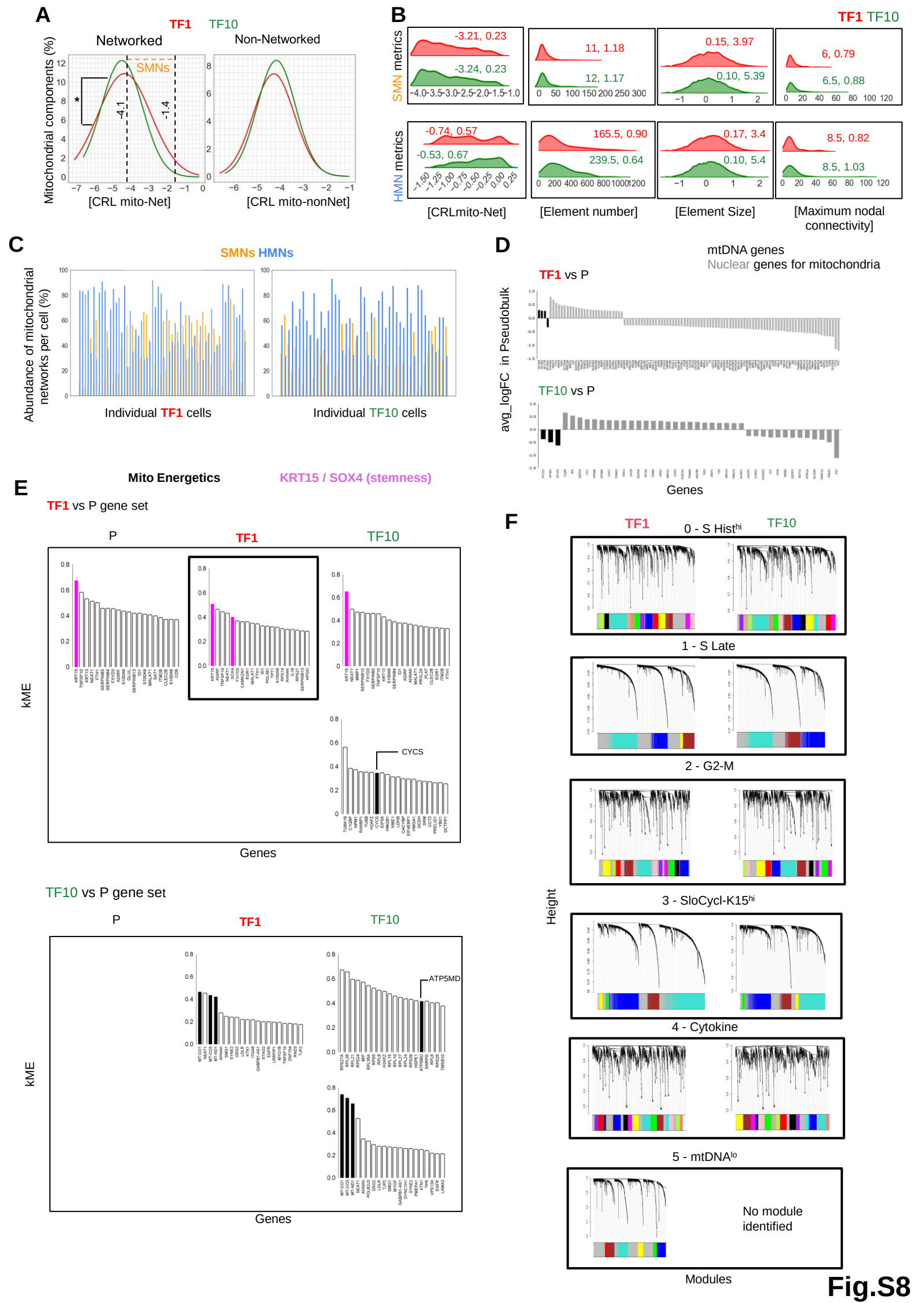
A
TF1
TF10
Networked
Non-Networked
SMNs
Mitochondrial components (%)
-4.1
-1.4
[CRL mito-Net]
[CRL mito-nonNet]
B
TF1 TF10
SMN metrics
HMN metrics
-3.21, 0.23
-3.24, 0.23
11, 1.18
12, 1.17
0.15, 3.97
0.10, 5.39
6, 0.79
6.5, 0.88
-0.74, 0.57
-0.53, 0.67
165.5, 0.90
239.5, 0.64
0.17, 3.4
0.10, 5.4
8.5, 0.82
8.5, 1.03
[CRLmito-Net]
[Element number]
[Element Size]
[Maximum nodal connectivity]
C
SMNs HMNs
Abundance of mitochondrial networks per cell (%)
Individual TF1 cells
Individual TF10 cells
D
mtDNA genes
Nuclear genes for mitochondria
TF1 vs P
TF10 vs P
avg_logFC in Pseudobulk
Genes
E
Mito Energetics
KRT15 / SOX4 (stemness)
TF1 vs P gene set
P
TF1
TF10
kME
CYCS
Genes
TF10 vs P gene set
ATP5MD
F
TF1
TF10
0 - S Hist^hi
1 - S Late
2 - G2-M
3 - SloCycl-K15^hi
4 - Cytokine
5 - mtDNA^lo
Height
No module identified
Modules

Fig.S8

Figure S8. Studying the impact of TF1 and TF10 transformation on mitochondrial structural properties employing mito-SinComp structural analyses and overall gene co-expression profile using hdWGCNA A. Histogram distribution of Cell-Relative Length of a mitochondrial component [CRL mito-Net] or [CRL mito-nonNet] corresponding to networked or non-networked mitochondrial components in TF1 and TF10 transformed cell population; threshold value for identifying SMNs and HMNs (same as **Fig 1**) are marked with dashed lines. **B.** Ridgeline plot comparing the distribution of structural parameters between SMNs and HMNs from TF1 and TF10 groups; Median and Coefficient of Variation are indicated for each parameter, the latter in bold. **C.** Bar plot showing the abundance of mitochondrial networks per cell in SMNs and HMNs categories in TF1 and TF10 groups. **D.** TF1 vs P and TF10 vs P pairwise pseudo-bulk analyses on scRNA-seq data; only mitochondrial nuclear encoded genes are shown here. **E.** kME Plots for hdWGCNA, for non mtDNA-KRT15 interacting modules using genelist from TF1 vs P (top) and TF10 vs.P (bottom) pairwise pseudo bulk analyses. The mtDNA encoded genes are labeled in black, and stem cell genes KRT15 and SOX4 are labeled in purple. **F.** Dendrograms as in **Fig.S7** for TF1 and TF10 hdWGCNA objects across scRNA-seq derived cell clusters.

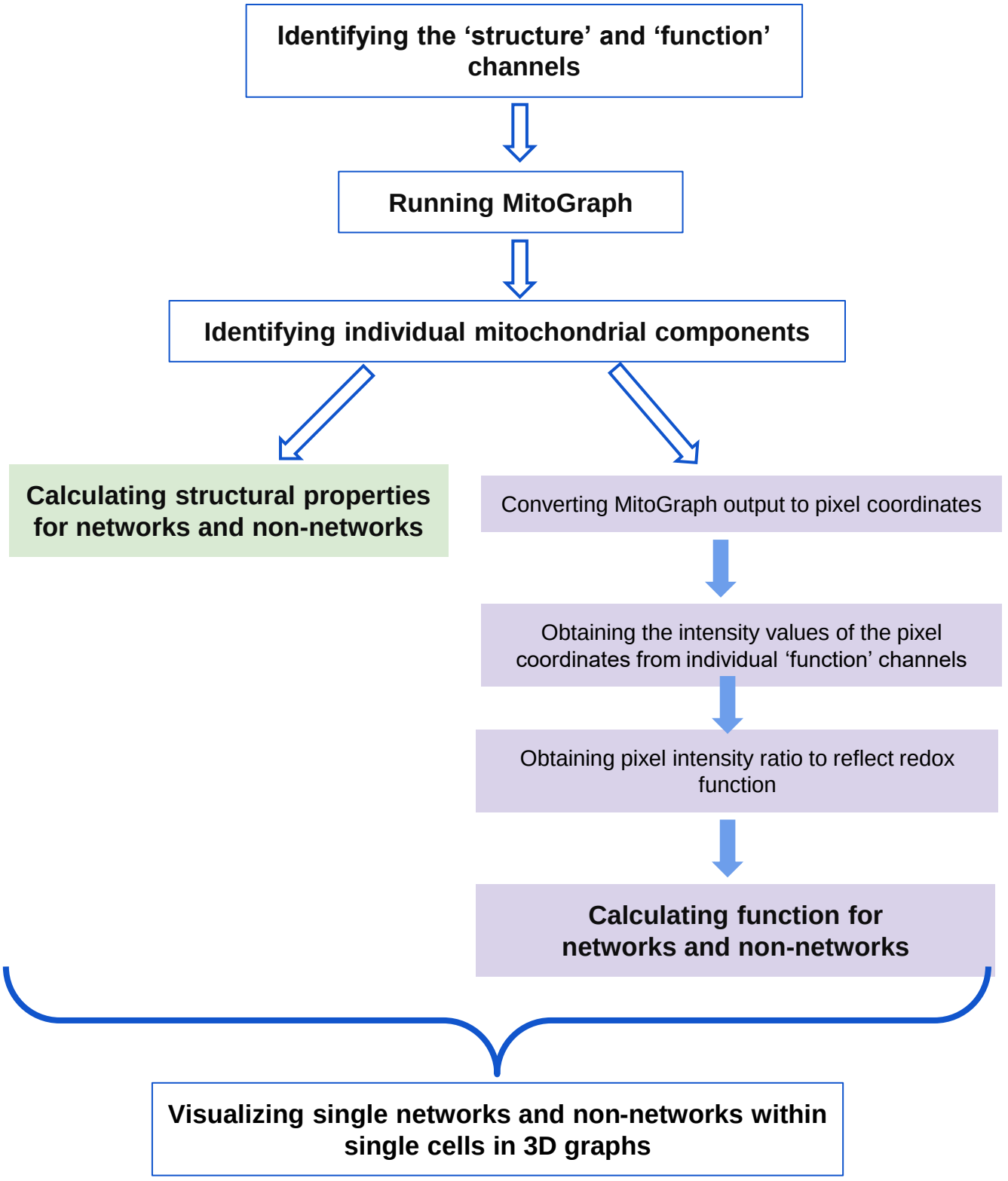
Identifying the 'structure' and 'function' channels
Running MitoGraph
Identifying individual mitochondrial components
Calculating structural properties for networks and non-networks
Converting MitoGraph output to pixel coordinates
Obtaining the intensity values of the pixel coordinates from individual 'function' channels
Obtaining pixel intensity ratio to reflect redox function
Calculating function for networks and non-networks
Visualizing single networks and non-networks within single cells in 3D graphs

Fig. S9

Figure S9. Workflow showing stepwise process for mito-SinComp analyses. The workflow includes identifying 'structure' and 'function' channels, running MitoGraph to delineate individual mitochondrial components, calculating structural and functional properties for networks and non-networks, and visualizing individual mitochondrial networks and non-networks in the form of 3D graphs.

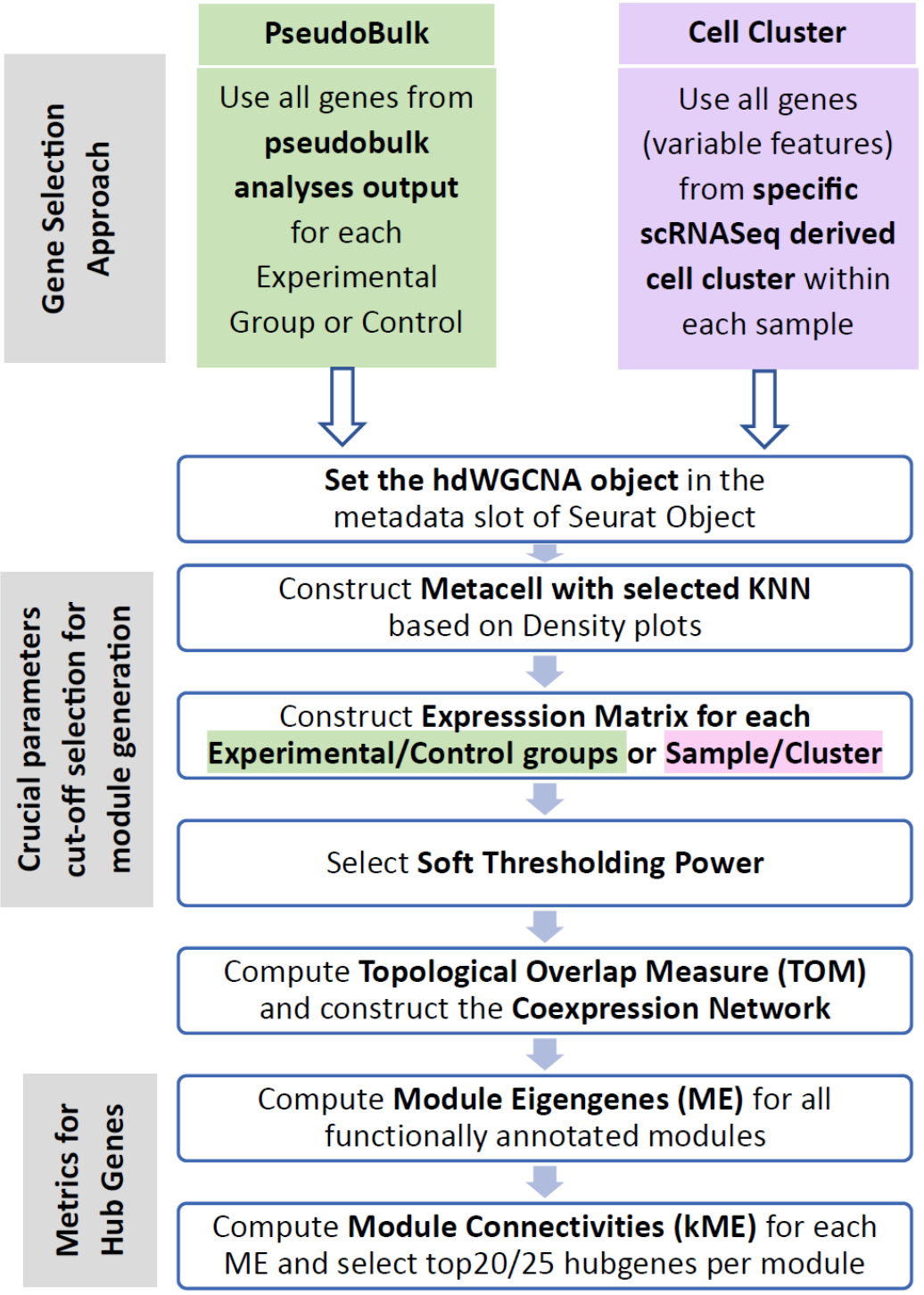
Gene Selection Approach
PseudoBulk
Use all genes from pseudobulk analyses output for each Experimental Group or Control
Cell Cluster
Use all genes (variable features) from specific scRNASeq derived cell cluster within each sample
Set the hdWGCNA object in the metadata slot of Seurat Object
Crucial parameters cut-off selection for module generation
Construct Metacell with selected KNN based on Density plots
Construct Expresssion Matrix for each Experimental/Control groups or Sample/Cluster
Select Soft Thresholding Power
Compute Topological Overlap Measure (TOM) and construct the Coexpression Network
Metrics for Hub Genes
Compute Module Eigengenes (ME) for all functionally annotated modules
Compute Module Connectivities (kME) for each ME and select top20/25 hubgenes per module

Fig. S10

Figure S10. Workflow for detailed stepwise process for hdWGCNA. The hdWGCNA workflow allows network-based transcriptomic analysis in both pseudobulk and single-cell cluster contexts. The stepwise process begins with setting up hdWCGNA object, then constructing metacells using K-nearest neighbors (KNN), followed by computing Pearson's correlations, and transforming them into adjacency matrices with soft-thresholding. Thereafter, networks are built using Topological Overlap Measures (TOM), and transcriptomic modules are identified via hierarchical clustering. Finally, module eigengenes (MEs) and connectivity (kME) values are calculated to identify hub genes.

A

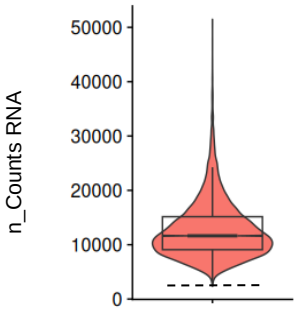

B

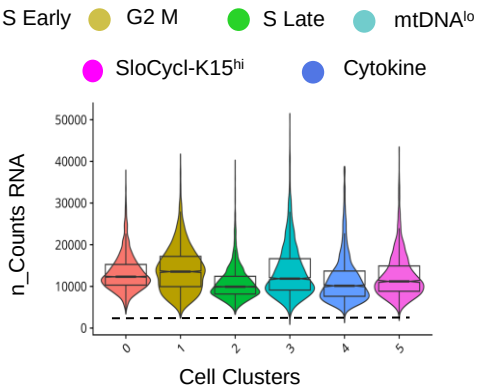

C

DRP1-kd Dataset	nCounts	KNN	Max shared
Pseudobulk	>=2000	20	10
Cell Cluster Based			

D

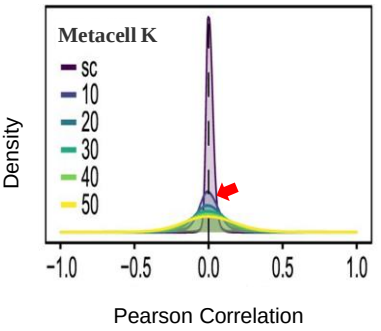

E

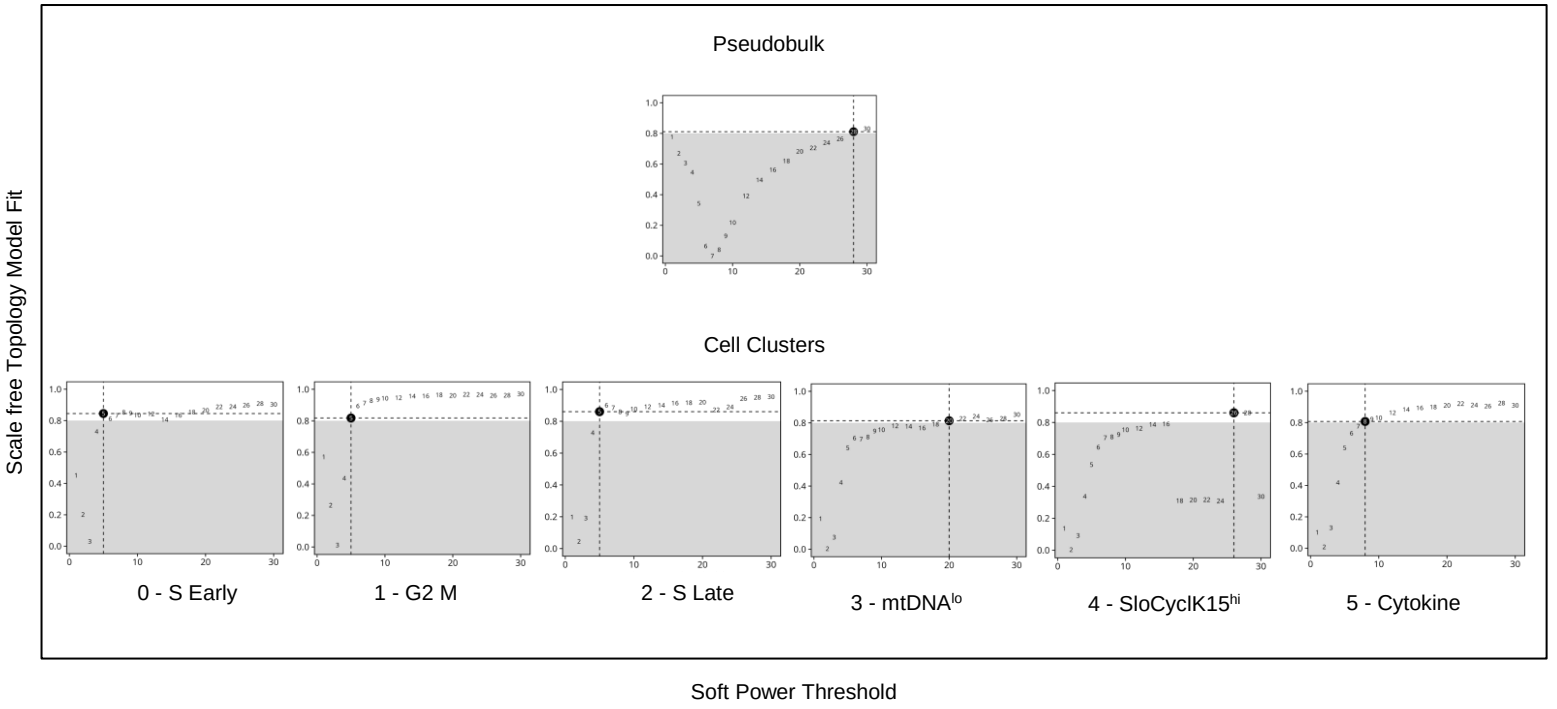

Fig. S11

Figure S11. Optimized parameters for hdWGCNA related to Fig. 1 A. Violin plots display the distribution of high-quality cell counts(n_Counts) for pooled data of DRP1-kd (W) & (S) with NT for pseudobulk analyses; dashed lines represent the selected threshold. **B.** Violin plots obtained as in **Fig.S11A** for clusterwise scRNASeq derived cluster. **C.** Table with parameters for n_Counts, KNN and maximum shared (max_shared) considered for the designated cell populations **D.** Density plot illustrating the distribution of pairwise Pearson correlations between genes from the single-cell expression matrix and metacell expression matrices with varying values of KNN parameter K; red arrow indicates the selected KNN value**. E.** Optimal soft-thresholding power (β) in hdWGCNA for DRP1 pooled data. The panel shows the influence of soft-threshold power on the scale-free fit index for the designated hdWGCNA object.

A

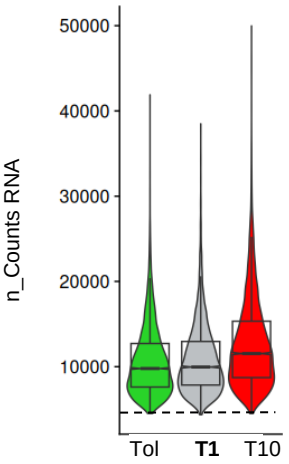

B

Dataset	nCount_RNA	KNN	Maxshared
Acute -2.5h: Pseudobulk	>=2000	20	10

C

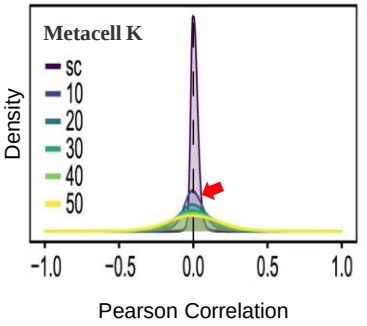

D

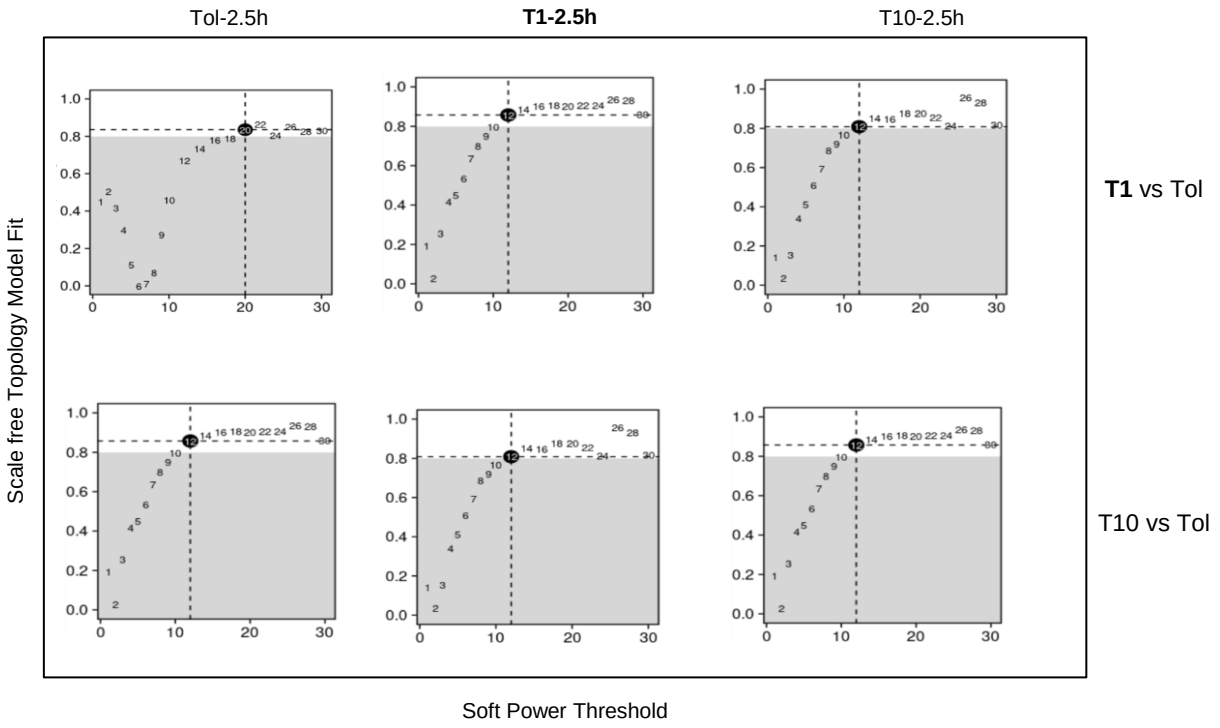

Fig. S12

Figure S12. A. Optimized parameters for hdWGCNA related to Fig. 4. Violin plots obtained as in **Fig.S11A** of T1-2.5hvs. Tol -2.5h and T10-2.5h vs. Tol -2.5h pseudobulk analyses based hdWGCNA objects. **B.** Table similar to **Fig.S11C** using pseudobulk analyses -hdWGCNA objects of Tol-2.5h, T1-2.5hand T10-2.5h **C.** Density plot similar to **Fig. S11D** for T1-2.5h vs. Tol -2.5h and T10-2.5h vs. Tol -2.5h pseudobulk analyses. **D.** Optimal soft-thresholding power (β) for T1-2.5h vs. Tol-2.5h and T10-2.5h vs. Tol-2.5h pseudobulk-hdWGCNA objects.

A

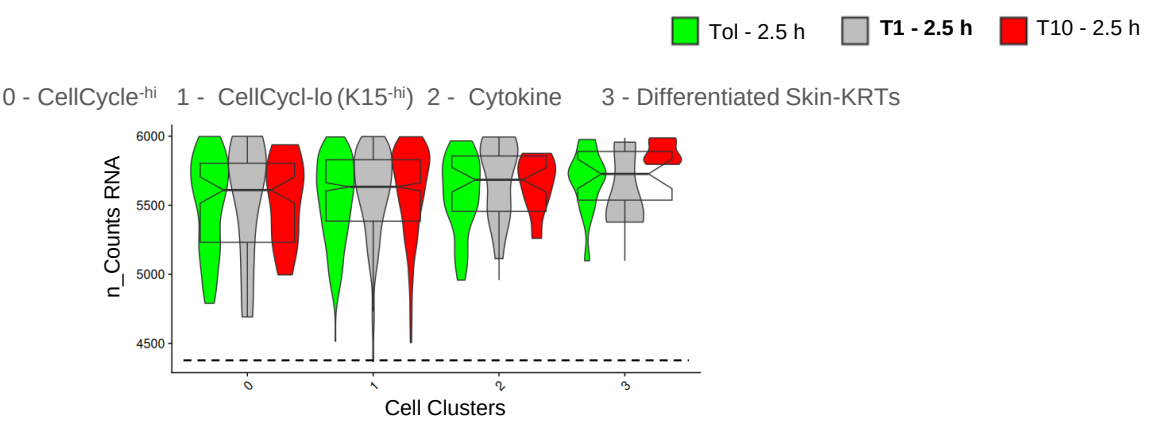

B

Dataset	nCounts	KNN	Max shared
Acute -2.5h: Cell Clusters	>=2000	20	10

C

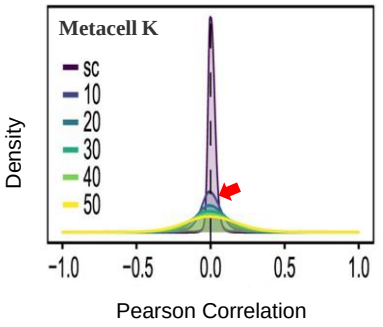

D

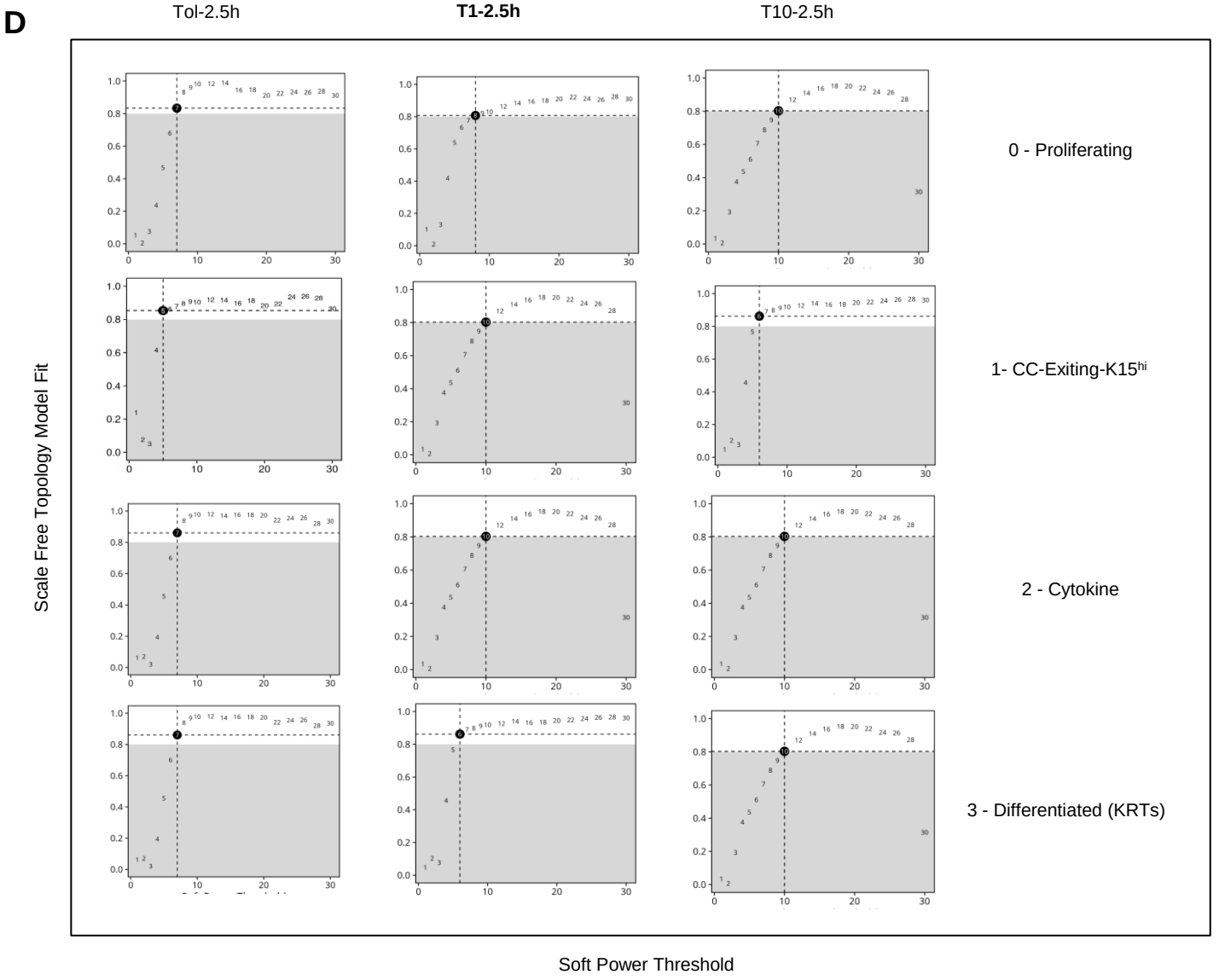

Fig. S13

Figure S13. Optimized parameters for hdWGCNA related to Fig. 5. A. Violin plots obtained as in **Fig.S11A** for Tol-2.5h, T1-2.5h and T10-2.5h across scRNA-seq derived clusters. **B.** Table similar to **Fig.S11C** using Tol-2.5h, T1-2.5hand T10-2.5h data **C.** Density plot similar to **Fig. S11D D.** Optimal soft-thresholding power (β) for Tol-2.5h, T1-2.5h and T10-2.5h cell clusters-hdWGCNA objects.

A

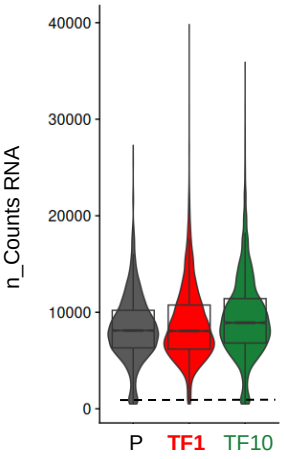

B

Dataset	nCount_RNA	KNN	Maxshared
Transformed: Pseudobulk	>=2000	20	10

C

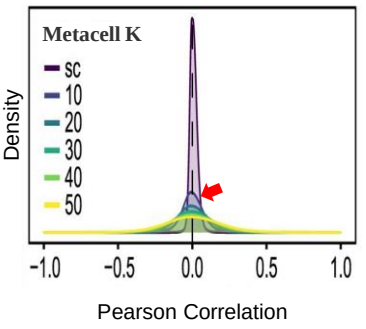

D

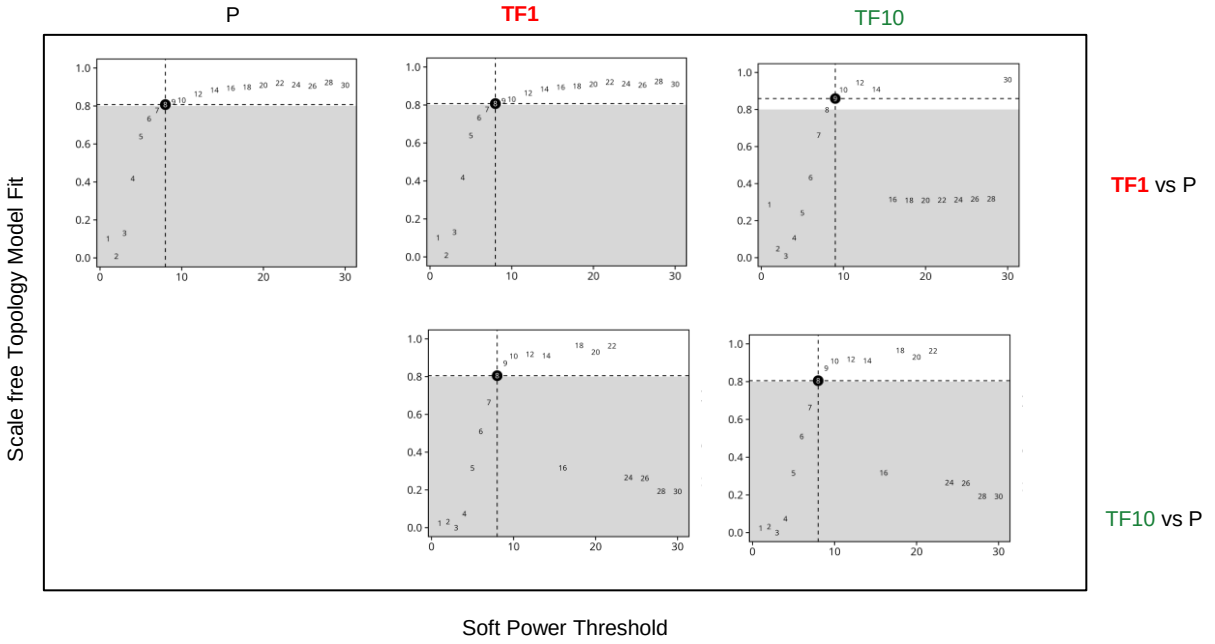

Fig. S14

Figure S14. Optimized parameters for hdWGCNA related to Fig. S8. A. Violin plots obtained as in **Fig.S11A** of TF1 and TF10 for pseudobulk analyses. **B.** Table similar to **Fig.S11C** for the transformed cell populations **C.** Density plot similar to **Fig. S11D** for the transformed cell populations. **D.** Optimal soft-thresholding power (β) for TF1 and TF10 pseudobulk-hdWGCNA objects.

A

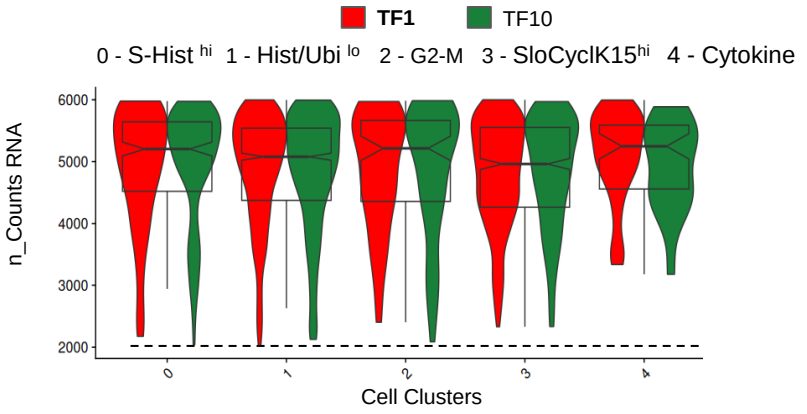

B

Dataset	nCounts	KNN	Max shared
TF1 & TF10	>=2000	20	10

C

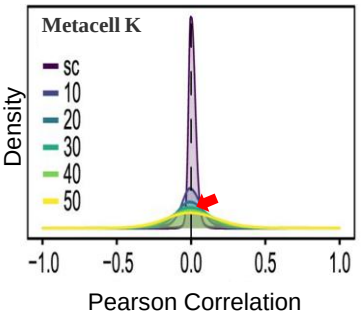

D

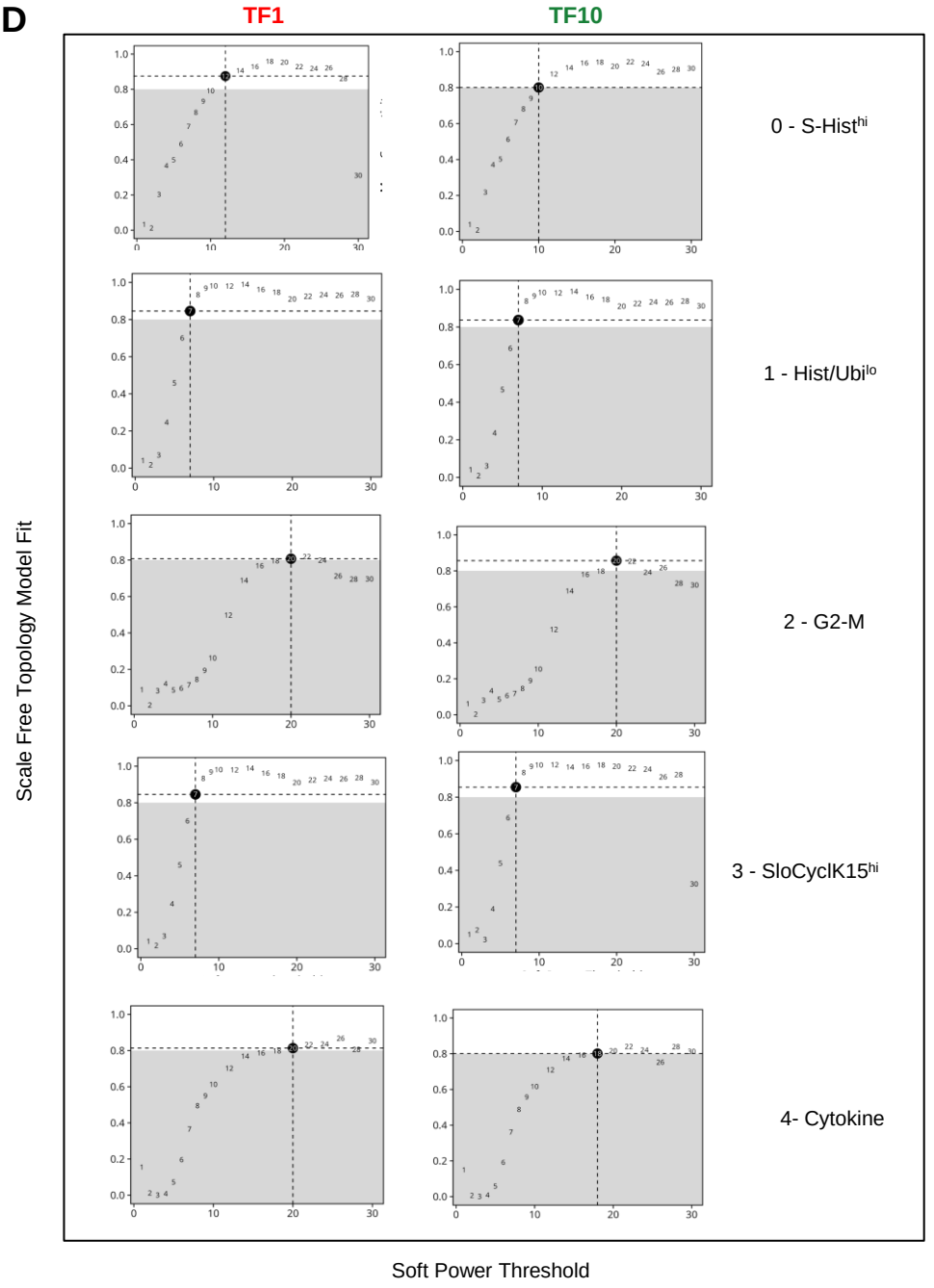

Fig. S15

Figure S15. Optimized parameters for hdWGCNA related to Fig. 6. A. Violin plots obtained as in **Fig.S11A** of TF1 and TF10 for scRNA-seq derived clusters. **B.** Table similar to **Fig.S11C** for the transformed cell populations **C.** Density plot similar to **Fig.S11D** for the transformed cell populations. **D.** Optimal soft-thresholding power (β) for TF1 and TF10 cell clusters-hdWGCNA objects.

References

1. B. Spurlock, K. Mitra, Mito-SinCe2 Approach to Analyze Mitochondrial Structure–Function Relationship in Single Cells. *Methods in Molecular Biology* **2275**, 415–432 (2021).

2. B. Spurlock, *et al.*, New quantitative approach reveals heterogeneity in mitochondrial structure–function relations in tumor-initiating cells. *J Cell Sci* **132** (2019).

3. M. P. Viana, S. Lim, S. M. Rafelski, Quantifying mitochondrial content in living cells. *Methods Cell Biol* **125**, 77–93 (2015).

4. S. Boccaletti, V. Latora, Y. Moreno, M. Chavez, D. U. Hwang, Complex networks: Structure and dynamics. *Phys Rep* **424**, 175–308 (2006).

5. M. P. Viana, *et al.*, Mitochondrial Fission and Fusion Dynamics Generate Efficient, Robust, and Evenly Distributed Network Topologies in Budding Yeast Cells. *Cell Syst* **10**, 287-297.e5 (2020).

6. S. Morabito, F. Reese, N. Rahimzadeh, E. Miyoshi, V. Swarup, hdWGCNA identifies co-expression networks in high-dimensional transcriptomics data. *Cell Reports Methods* **3** (2023).